Scanning probe methods on insulating films offer a rich toolbox to study electronic, structural and spin properties of individual molecules. This work discusses three issues in the field of molecular and organic electronics.

An STM head to be operated in high magnetic fields has been designed and built up. The STM head is very compact and rigid relying on a robust coarse approach mechanism. This will facilitate investigations of the spin properties of individual molecules in the future.

Combined STM/AFM studies revealed a reversible molecular switch based on two stable configurations of DBTH molecules on ultrathin NaCl films. AFM experiments visualize the molecular structure in both states. Our experiments allowed to unambiguously determine the pathway of the switch.

Finally, tunneling into and out of the frontier molecular orbitals of pentacene molecules has been investigated on different insulating films. These experiments show that the local symmetry of initial and final electron wave function are decisive for the ratio between elastic and vibration-assisted tunneling. The results can be generalized to electron transport in organic materials.

Universitätsverlag Regensburg

ISBN 978-3-86845-100-9

gefördert von:

Alumni der physikalischen Fakultät der Universität Regensburg e.V.

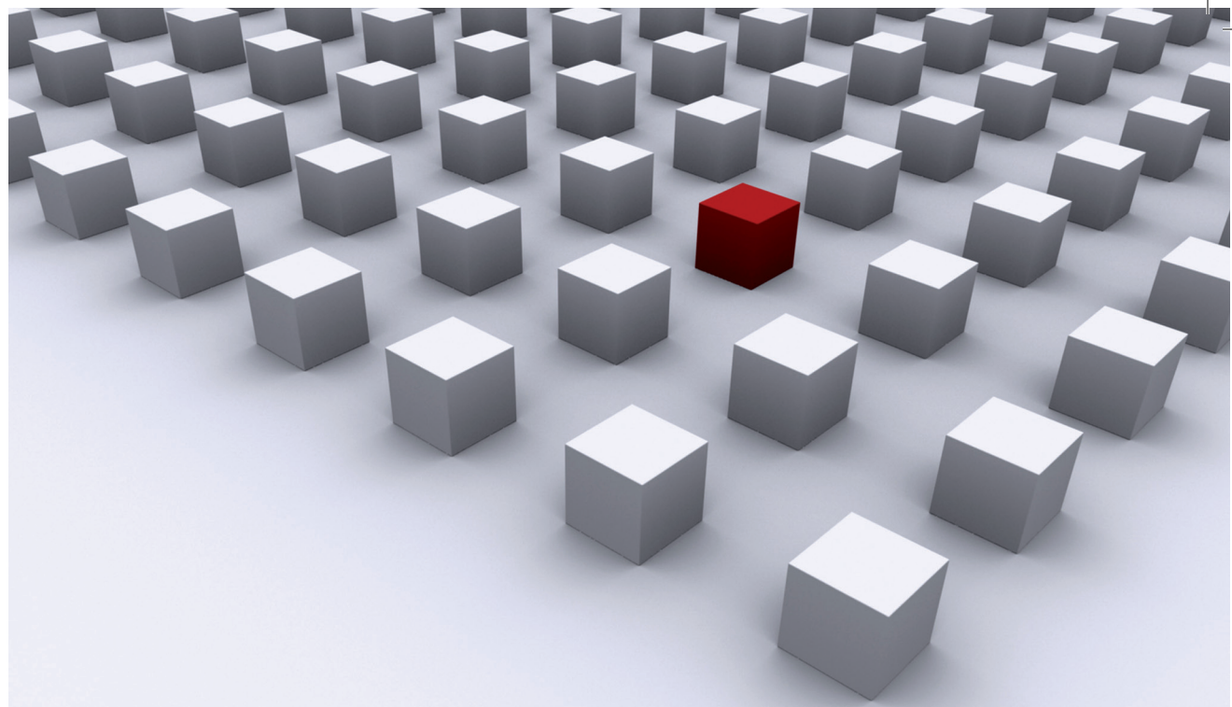

Niko Pavliček

Scanning Probe Methods Applied to Molecular Electronics

Universitätsverlag Regensburg

Dissertationsreihe Physik - Band 33

Niko Pavliček

33

Dissertationsreihe Physik

Universität Regensburg

Niko Pavliček

Scanning Probe Methods Applied to Molecular Electronics

Scanning Probe Methods
Applied to Molecular Electronics

Dissertation zur Erlangung des Doktorgrades der Naturwissenschaften (Dr. rer. nat.)
der Fakultät Physik der Universität Regensburg

vorgelegt von

Niko Pavliček
aus Stuttgart
2013

Die Arbeit wurde von Prof. Dr. Jascha Repp angeleitet.
Das Promotionsgesuch wurde am 8. Februar 2013 eingereicht.
Das Promotionskolloquium fand am 5. Juni 2013 statt.

Prüfungsausschuss:	Vorsitzende:	Prof. Dr. Milena Grifoni
	1. Gutachter:	Prof. Dr. Jascha Repp
	2. Gutachter:	Prof. Dr. Josef Zweck
	weiterer Prüfer:	PD Dr. Tobias Korn

Dissertationsreihe der Fakultät für Physik der Universität Regensburg, Band 33

Herausgegeben vom Präsidium des Alumnivereins der Physikalischen Fakultät:
Klaus Richter, Andreas Schäfer, Werner Wegscheider, Dieter Weiss

Niko Pavliček

Scanning Probe Methods Applied to Molecular Electronics

Universitätsverlag Regensburg

Bibliografische Informationen der Deutschen Bibliothek.
Die Deutsche Bibliothek verzeichnet diese Publikation
in der Deutschen Nationalbibliografie. Detailierte bibliografische Daten
sind im Internet über http://dnb.ddb.de abrufbar.

1. Auflage 2013

Leibnizstraße 13, 93055 Regensburg

Konzeption: Thomas Geiger
Umschlagentwurf: Franz Stadler, Designcooperative Nittenau eG
Layout: Niko Pavliček
Druck: Docupoint, Magdeburg
ISBN: 978-3-86845-100-9

Weitere Informationen zum Verlagsprogramm erhalten Sie unter:
www.univerlag-regensburg.de

Scanning Probe Methods Applied to Molecular Electronics

Dissertation zur Erlangung des Doktorgrades der Naturwissenschaften (Dr. rer. nat.) der Fakultät Physik der Universität Regensburg

vorgelegt von

Niko Pavliček
aus Stuttgart

Februar 2013

Die Arbeit wurde von Prof. Dr. Jascha Repp angeleitet.
Das Promotionsgesuch wurde am 8. Februar 2013 eingereicht.
Das Promotionskolloquium fand am 5. Juni 2013 statt.

Prüfungsausschuss:	Vorsitzende:	Prof. Dr. Milena Grifoni
	1. Gutachter:	Prof. Dr. Jascha Repp
	2. Gutachter:	Prof. Dr. Josef Zweck
	weiterer Prüfer:	PD Dr. Tobias Korn

NIKO PAVLIČEK

SCANNING PROBE METHODS APPLIED TO MOLECULAR ELECTRONICS

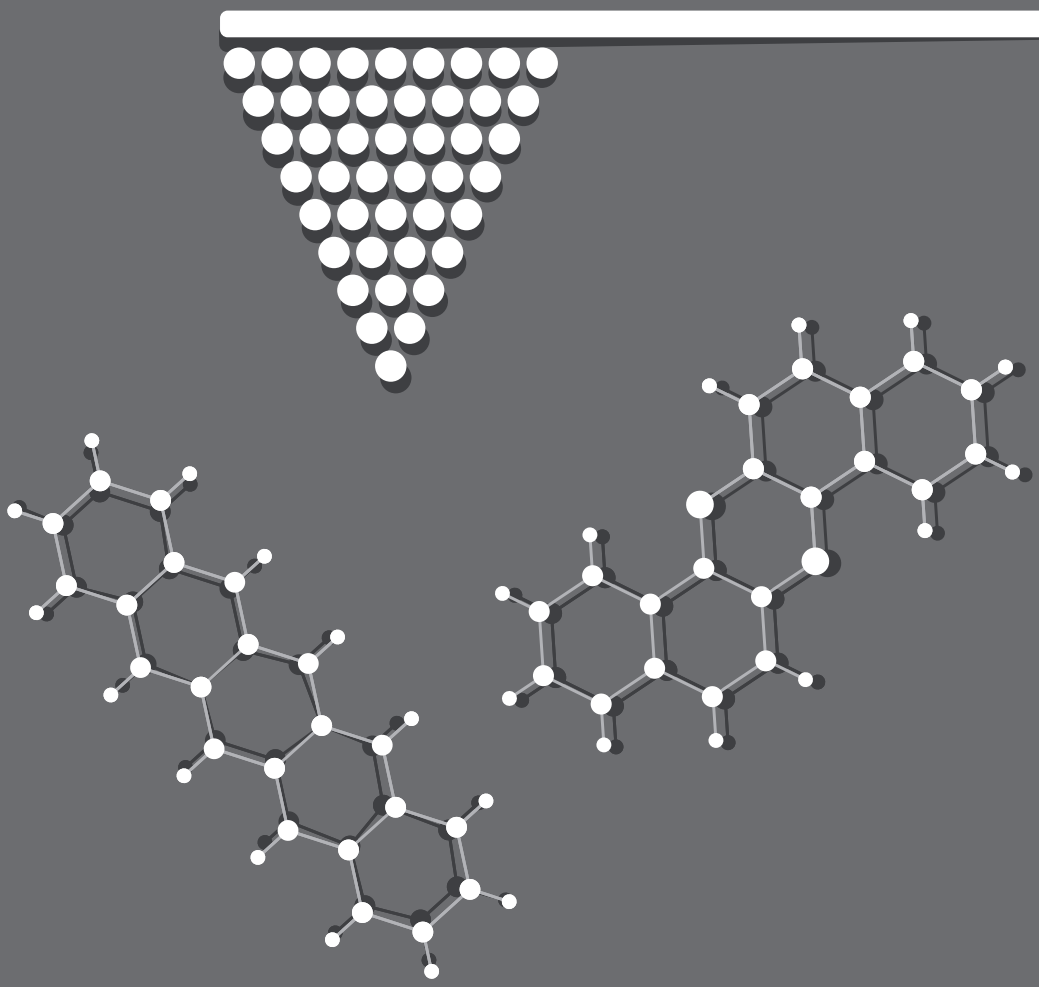

Illustration on recto by Jonas Pavliček shows an oscillating AFM cantilever and the chemical structures of the molecules investigated in this work.

To Florentina & Dario

Abstract

Scanning probe methods (SPM) on insulating films offer a rich toolbox to investigate various properties of individual molecules. Electronic properties are accessible by means of scanning tunneling microscopy (STM) and spectroscopy (STS). Visualizing the molecular structure requires implementation of atomic force microscopy (AFM). Finally, high magnetic fields extend the imaging and manipulation capabilities of STM/STS to spin properties on the atomic scale. This work deals with three issues in the field of scanning probe microscopy (SPM) applied to molecular electronics.

First, to further widen the scope of research in our group, an STM head to be operated in high magnetic fields has been designed and built up. The STM head is very compact and rigid and relies on a robust coarse approach mechanism. This will allow to investigate also the spin properties of individual molecules in the future.

As a second issue, a reversible molecular switch based on two stable configurations of dibenzo[a,h]thianthrene (DBTH) molecules on ultrathin NaCl films has been discovered using a combined STM/AFM. The molecular structure could be visualized in both states by means of AFM. In addition, it was possible to unambiguously determine the pathway of the switch.

As the third and last main topic, tunneling into and out of the frontier molecular orbitals has been investigated for a simple model system– individual pentacene molecules on different insulating films. The experiments show that the symmetry of initial and final wave function are decisive for the ratio between elastic and vibration-assisted, that is dissipative, tunneling. The results can be generalized to electron transport in organic materials. For instance, this phenomenon has a high impact on the efficiency of organic solar cells.

Contents

1. Introduction

The invention of the scanning tunneling microscopy (STM) by Binnig *et al.* (*1*) has paved the way for the emerging field of atomic-scale science. Imaging surfaces in real space (*2*, *3*) as well as spectroscopy (*4*) with atomic precision became reality for the first time. Latter technique is called scanning tunneling spectroscopy (STS). In 1990, Stroscio and Eigler demonstrated the possibility of atom manipulation using low-temperature STM (*5*). Thus, Feynman's dream of rearranging single atoms mentioned in his famous speech "There's plenty of room at the bottom" (*6*) came true.

Only a few years after the invention of the STM, Binnig, Quate, and Gerber (*7*) introduced the atomic force microscope (AFM) as a promising tool to image non-conducting surfaces with atomic resolution. However, it took nearly a decade until the mission of atomic resolution had eventually been accomplished by imaging the Si(111)-(7x7) reconstruction (*8*) using frequency modulation AFM (*9*).

These fascinating capabilities of scanning probe microscopy (SPM) triggered rapid evolvement of a whole slew of branches in atomic-scale science. Several groundbreaking experiments laid the foundation for the work presented in this thesis.

To begin with, decoupling adsorbates from the metallic substrate by means of ultrathin insulating films allows imaging of the unperturbed molecular orbitals of adsorbed molecules (*10*). By applying high magnetic fields at the tunneling junction, decoupling layers also enable experiments to measure and manipulate spin properties of single atoms (*11–14*) or molecules (*15*, *16*). All of the latter experiments make extensive use of inelastic electron tunneling spectroscopy (IETS) (*17*). This necessitates a very stable tip-sample junction, which is insensitive to mechanical vibrations.

In this context, I will present the design and construction of a scanning tunneling microscope head to be operated at low temperatures and in high magnetic fields. Its vertical coarse approach (*18*), which is the centerpiece of an STM, is well established for applications in high magnetic fields (*19–21*). Recently, STM heads based on this working principle have been employed in ultrahigh vacuum even at lowest temperatures on the order of 50 mK (*22*, *23*). To achieve a high resonance frequency of the instrument, we aimed for a rigid and compact design.

After invention of the qPlus sensor in 2000 (*24*), it became possible to build combined scanning tunneling and atomic force microscopes operating at low temperatures and in ultrahigh vacuum conditions with affordable experimental effort. Such microscopes have proved to facilitate exciting experiments on the atomic scale. For instance, the force needed to move an atom (*25*) has been measured in 2008. Shortly after, the chemical structure of single molecules has been visualized in AFM mode (*26*), a method which has already been used to identify the organic structure of a natural compound (*27*). Similar setups enabled measurement of the force-field above a single molecule (*28*), imaging of the charge distribution in a single molecule (*29*), as well as the angular dependence of chemical bonds (*30*).

In this thesis, we have investigated a series of thianthrene-derivatives. The sulphur atoms in such molecules lead to a folded geometry. On the one hand this deviation of strictly planar molecules complicates scanning probe microscopy, but on the other hands provides an additional degree of freedom on adsorption. This manifests itself in experiments on dibenzo[a,h]thianthrene (DBTH) molecules showing two distinct configurational isomers. These different configurations could be visualized using above mentioned capability of AFM to image the chemical structure of adsorbates. STM mode enables reversible switching between both molecular configurations. Utilizing symmetry arguments it was also possible to reveal the reaction pathway of this configurational switch.

The electronic properties of organic materials are of great interest for prospective future devices. For instance, the development of polymer

solar cells has attracted considerable attention (*31–33*). Investigating the possibility of single-molecule electronic devices is another vibrant field of research (*34*, *35*). To minimize dissipation it is necessary to understand charge transport through organic molecules on a fundamental level. To this end, we have performed a study on the spatial dependence of inelastic electron transport into molecular orbitals. These experiments unambiguously prove that the local symmetry of initial and final wave function with respect to each other determine the ratio of elastic to inelastic transport.

Following this introduction, this thesis is divided in three structural parts: the basic theory needed to understand the measurement signals in STM and STS (chapter 2), as well as noncontact AFM (chapter 3) will be introduced in part I.

The experimental details are subject of part II. Techniques for low-temperature measurements, particularly regarding the design of STM heads working in high magnetic fields, are discussed in chapter 4. This mainly covers basic issues of material selection for ultrahigh vacuum (UHV) applications, heat transport at cryogenic temperatures, and magnetic forces, providing the fundamentals for chapter 9. Then, the peculiarities of STM on ultrathin insulating films will be discussed in chapter 5. Chapter 6 deals with the experimental implementation of the force measurement scheme and the tip-functionalization required to visualize the chemical structure of adsorbates in AFM mode. The experimental setup and the sample preparation methods are introduced in chapter 7. A very brief discussion of density functional theory (DFT) and its application with regard to experiments presented later in this thesis concludes this part (chapter 8).

The practical part of this thesis is subject of part III. First, chapter 9 starts with the design, construction and build-up of the STM head capable of operation in high magnetic fields. Then, the experiments using existing scanning probe microscopes are presented. Above mentioned experiments on DBTH molecules are presented in chapter 10. The work on the symmetry-dependence of vibration-assisted tunneling is subject of chapter 11.

Part I.

Fundamentals of Scanning Probe Microscopy

2. Scanning Tunneling Microscopy

This chapter reviews the theory needed to understand scanning tunneling microscopy (STM) and spectroscopy (STS). After presenting the principle of STM in section 2.1, section 2.2 goes into details of STM theory. An expression for the tunneling matrix element will be derived. Based on that it will be shown that STM probes the contour of constant local density of states of the sample at the position of the tip. Subsequently, an expression for the differential conductance, which is measured in scanning tunneling spectroscopy experiments, will be derived in section 2.3.

2.1. Principle

Scanning tunneling microscopy was invented (*1*) and realized (*2*, *3*) by Binnig *et al.* in 1982. Its principle is based on quantum mechanical tunneling through a potential barrier (*36*). The basic idea is illustrated in figure 2.1. A small metal tip is positioned laterally (x- and y-direction) and vertically (z-direction) by piezoelectric actuators (piezos). The x- and y-piezos are used to scan the tip over the sample surface, while the z-piezo determines the tip-sample distance. If the tip-sample distance is in the range of several Ångstrom, the wave functions of tip and

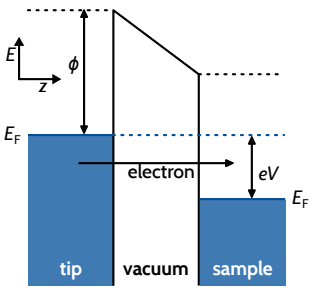

Figure 2.1.: Principle of STM imaging. At low temperature all states below the Fermi levels E_F of tip and sample, respectively, are occupied. By applying a bias voltage eV a net current flows. For simplicity it is assumed that the work function ϕ is the same for tip and sample.

sample overlap enabling electron tunneling through the vacuum barrier. Tip and surface then form a metal–vacuum–metal tunneling junction. Applying a bias voltage between tip and sample gives rise to a net current.

In the limit of small applied voltages the potential of the tunneling-barrier height is approximately equal to the mean work function ϕ. From a simple one-dimensional model it follows that the tunneling current I decays exponentially as a function of tip-surface distance z (*1*, *37*),

$$I(z) \cong I_0 \exp(-2\alpha z), \tag{2.1}$$

where

$$\alpha = \frac{\sqrt{2m\phi}}{\hbar} \tag{2.2}$$

is the decay constant; m denotes the electron mass. Using typical values of $\phi \approx 5\,\mathrm{eV}$ for the work function of metals,

$$\alpha \approx 11.4\,\mathrm{nm}^{-1}. \tag{2.3}$$

Equation (2.3) states that the tunneling current decays roughly one order of magnitude per one Ångstrom increase in tip-sample distance. This is an important rule of thumb, and one of the main reasons why atomic resolution in STM is relatively easy to achieve.

In *constant current mode*, the feedback system maintains the tunneling current constant by adjusting the tip-sample distance with the z-piezo, while scanning the surface. Using equation (2.1) and (2.2) one can define the *apparent barrier height* as

$$\Phi = \frac{\hbar^2}{8m}\left(\frac{d}{dz}\ln I\right)^2. \tag{2.4}$$

Accordingly, an STM image is a map of the surface topography. Alternatively it is possible to image in *constant height mode*, in which the vertical position of the tip remains constant and resulting variations in the current are mapped. This scanning mode necessitates flat sample surfaces and has high demands on the junction stability.

2.2. Derivation of the Tunneling Current

Using **Bardeen's theory of tunneling** (*38*) one can derive an expression for the tunneling matrix element in an STM junction. Bardeen originally considered metal–insulator–metal junctions when working in the field of superconductivity (*39*).

Say, two electrodes, namely tip and sample, are far away from each other. Then, their wave functions χ_ν and ψ_μ both decay into the vacuum. When bringing the two electrodes together, the Schrödinger equation of the combined system is

$$i\hbar\frac{\partial\Psi}{\partial t} = \left[-\frac{\hbar^2}{2m}\nabla^2 + U_T + U_S\right]\Psi, \tag{2.5}$$

where U_T and U_S are the potential functions of tip and sample, respectively. An electron, initially in a state ψ_μ of the sample, has a chance of transferring to a state χ_ν of the tip. The tunneling matrix element M can be written as a surface integral,

$$M = \frac{\hbar^2}{2m}\int_\Sigma \left(\psi_\mu^*\nabla\chi_\nu - \chi_\nu\nabla\psi_\mu^*\right)\mathrm{d}\mathbf{S}, \tag{2.6}$$

where Σ is any separation surface between tip and sample. Calculating the tunneling current I at bias voltage V is now done by summing up over all relevant states. This yields

$$\begin{aligned} I = \frac{4\pi e}{\hbar}\int_{-\infty}^{\infty} &[f(E_F - eV + \epsilon) - f(E_F + \epsilon)] \\ &\times \rho_T(E_F - eV + \epsilon)\rho_S(E_F + \epsilon)|M|^2\,\mathrm{d}\epsilon, \end{aligned} \tag{2.7}$$

where $f(E)$ is the Fermi distribution function and ρ_T and ρ_S are the density of states (DOS) of tip and sample, respectively. In the limit of small temperatures the Fermi distribution function is replaced by a step function, and the formula simplifies to

$$I \propto \int_0^{eV} \rho_T(E_F - eV + \epsilon)\rho_S(E_F + \epsilon)|M|^2\,\mathrm{d}\epsilon. \tag{2.8}$$

When imaging at small bias voltages V it is a good approximation to take M constant and to linearize the integral. Hence,

$$I \propto \rho_T(E_F)\rho_S(E_F + eV)\, V. \tag{2.9}$$

From this it follows that the STM actually measures the convolution of the DOS of tip and sample.

In general, the tip states are unknown. Tersoff and Hamann proposed a widely used model (*40*, *41*), in which an explicit tip wave function is assumed. First, the sample wave function is expanded in the form

$$\psi(\mathbf{r}) = \int d^2\mathbf{q}\, a(\mathbf{q}) e^{-\sqrt{\mathbf{q}^2+\alpha^2}z + i\mathbf{q}\mathbf{x}}, \tag{2.10}$$

where $\mathbf{x} = (x, y)$, $\mathbf{q} = (k_x, k_y)$, and $a(\mathbf{q})$ are the Fourier components at $z = 0$. The wave function of the STM tip is now modeled as locally spherical symmetric with respect to the center of curvature $\mathbf{r}_0$, as shown in figure 2.2, which is the basic assumption of the **Tersoff and Hamann approximation (THA)**. Now, one can derive an explicit expression for the tip wave function. In polar coordinates, where $r^2 = x^2 + y^2 + (z - z_0)^2$, the solution of the Schrödinger equation for the tip is

$$\chi(r) = \frac{1}{r} e^{-\alpha r}. \tag{2.11}$$

Inserting the values of ψ and χ given by equation (2.10) and equation (2.11), respectively, into equation (2.6) results in

$$M \propto \psi(\mathbf{r}_0). \tag{2.12}$$

This means that the tunneling matrix element is proportional to the value of the sample wave function at the center of curvature of the tip. Hence, equation (2.8) becomes

$$\boxed{I \propto |\psi(\mathbf{r}_0)|^2 \rho_S(E_F)\, V = \rho(E_F, \mathbf{r}_0)\, V.} \tag{2.13}$$

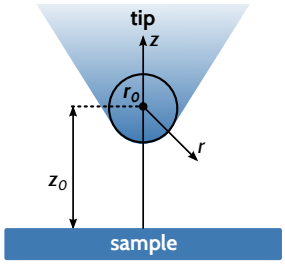

Figure 2.2.: Illustration of *s*-wave tip model used by Tersoff and Hamann (after (*37*)). The tip is modeled as spherically symmetric around $\mathbf{r}_0$ in a distance z_0 to the surface. In polar coordinates r is the distance with respect to $\mathbf{r}_0$.

The right part of equation (2.13) defines $\rho(E_F, \mathbf{r}_0)$ as the local density of states (LDOS) of the sample at the Fermi level at the center of curvature of the tip. In constant current mode, the STM thus probes a *contour of constant LDOS*. This is the central result of the THA.

In conclusion, in THA the tip is modeled as spherically symmetric around a point $\mathbf{r}_0$. This is equivalent to a point-like tip at $\mathbf{r}_0$. In the limit of low temperatures and low bias voltage the tunneling current is then proportional to the LDOS.

2.3. Scanning Tunneling Spectroscopy

Beside imaging, STM is also capable of local spectroscopic investigations with atomic resolution. For such a measurement one interrupts the feedback loop after having moved the STM tip to be above the desired sample position. Then, a voltage ramp is applied to the tunneling junction and the dynamic tunneling conductance is recorded as a function of the applied bias voltage V.

The differential conductance can be obtained by derivation of equa-

tion (2.8) with respect to the bias voltage V,

$$G(V) = \frac{dI}{dV}(V) \propto \rho_T(E_F)\rho_S(E_F + eV)|M(E_F + eV)|^2 + \tag{2.14}$$

$$\int_{E_F}^{E_F+eV} \left.\frac{d\rho_T}{dE}\right|_{E=\epsilon-eV} \rho_S \, |M|^2 \, d\epsilon + \tag{2.15}$$

$$\int_{E_F}^{E_F+eV} \rho_T \, \rho_S \left.\frac{d|M|^2}{dE}\right|_{E=\epsilon-eV} d\epsilon. \tag{2.16}$$

The physical quantity, in which we are actually interested is the voltage dependence of the density of states of the sample $\rho_S(E_F + eV)$, i. e. only the first term. The remaining two terms can be minimized as following:

- The influence of the density of states of the tip $\rho_T(E_F)$ can be estimated by taking spectra on the clean surface. Only if the measured signal is reasonably featureless a spectra is taken above the molecule of interest. Otherwise controlled tip-sample contacts are performed until the density of state of the tip is approximately constant.
- The square of the tunneling matrix element $|M(E_F + eV)|^2$ strongly depends on the applied bias voltage V, since the tunneling barrier collapses at large voltages. Hence, this term is constant for low voltages, while for $V \gg 0$ an exponential increase is observed.

When ρ_T is reasonably flat in the voltage range of interest, and V is not too high, the differential conductance can be written as

$$\boxed{\frac{dI}{dV}(V) \propto \rho_T(E_F)\rho_S(E_F + eV)|M(E_F + eV)|^2.} \tag{2.17}$$

In summary, STS allows to atomically resolve the energy dependence of the LDOS. Since STS measurements are performed in constant height mode, it is clear that measuring at low temperatures simplifies matters due to drastical lower thermal drift.

3. Atomic Force Microscopy

The atomic force microscope (AFM) was introduced shortly after the STM in 1986 by Binnig, Quate, and Gerber (*7*) as an instrument also capable of imaging insulating surfaces. Like in STM, a sharp tip is scanning a sample surface. The difference is that in AFM the tip is mounted to a cantilever. The interaction between tip and sample leads to a deflection of the cantilever. Either the deflection itself or a derived quantity acts as measurement signal. After introduction of the dynamical mode of operation (*9*), which will be discussed below, true atomic resolution (*8*) became routinely possible[1].

In STM, one commonly distinguishes two *imaging* modes, namely constant *current* mode from constant *height* mode. In AFM, things are more sophisticated and different *operation* modes exist. The main ones are static (also called contact) and dynamic (noncontact) mode. In static mode the tip-sample force leads to a deflection of the probe. The deflection is directly proportional to the force and serves as the imaging signal. In dynamic operation mode the cantilever is driven to oscillate close to its eigenfrequency. The tip-sample interaction is then either measured in *amplitude modulation* (AM)(*44*) or in *frequency modulation mode* (FM)(*9*). In this work, we exclusively apply the frequency modulation detection scheme of dynamic AFM, commonly abbreviated as FM-AFM[2].

The fundamentals of dynamic AFM are outlined in section 3.1. A simple formula for the frequency shift as a function of tip-sample interaction force will be derived. Then, the different contributions of short- and

[1] Ohnesorge and Binnig (*42*) have observed single surface atoms of calcite in a liquid environment for the first time in 1993. At this time, they used a microscope in which the deflection of the lever was measured optically (*43*).

[2] FM-AFM, dynamic AFM and noncontact AFM (NC-AFM) are often used synonymously in literature. Here, FM-AFM is mainly used when discussing the force-detection scheme. Apart from that dynamic AFM is used for better readability.

long-range forces to the tip-sample interaction will be discussed in section 3.2.

3.1. Frequency Modulation Atomic Force Microscopy

The combined scanning tunneling and atomic force microscope used for the experiments in chapter 10 is based on the qPlus tuning fork design (*24*). The AFM was operated in the frequency modulation mode (*9*) and sub-Ångstrom oscillation amplitudes have been used to maximize the lateral resolution (*45*). The origin of the imaging signal will be discussed in this section, whereas experimental details are given in the methods part (see chapter 6).

In dynamic AFM (*46*, *47*) the cantilever with a sharp tip is oscillating close to the sample surface as depicted in figure 3.1. The potential energy between tip and sample is U_{ts}. Then, the oscillation perpendicular to the surface causes a vertical tip-sample force,

$$F_{\mathrm{ts}} = -\frac{\partial U_{\mathrm{ts}}}{\partial z}, \tag{3.1}$$

which is the physical quantity in which we are interested. In the frequency modulation mode, which we use to operate our AFM, the cantilever oscillates close to its eigenfrequency at a given amplitude. Variations in the tip-sample force F_{ts} cause a frequency shift Δf of the cantilever which serves as the imaging signal. A control loop maintains the oscillation amplitude to be constant by driving the cantilever by means of mechanical excitation.

In a simple picture, the sharp tip mounted to an oscillating cantilever can be modeled as a mass and a spring, as depicted in figure 3.1. The tip of mass m and the cantilever with a spring constant k_0 are oscillating at its eigenfrequency f_0, where

$$f_0 = \frac{1}{2\pi}\sqrt{\frac{k_0}{m}}. \tag{3.2}$$

Now, the tip-sample force F_{ts} is modeled as an additional spring with stiffness k_{ts}. Treating F_{ts} in a linear response model is justified in the

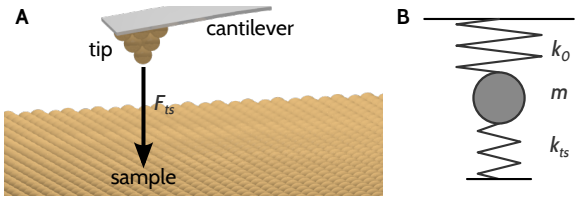

Figure 3.1.: Mass and spring model. **A** Rendered model of an oscillating cantilever with a tip above a sample surface. **B** Corresponding mass and spring model. The analogous model of cantilever and tip is a mass *m* attached to a spring with stiffness k_0. The tip-sample force is modeled by an additional spring with stiffness k_{ts}.

limit of small oscillation amplitudes. In this case, k_{ts} can be taken constant over the range of one oscillation cycle. Then, the oscillation frequency of the cantilever is

$$f = \frac{1}{2\pi}\sqrt{\frac{k_0 + k_{\mathrm{ts}}}{m^*}}, \tag{3.3}$$

where $k_0 + k_{\mathrm{ts}}$ is an effective spring constant and m^* is its effective mass. The square root can be expanded as $\left(\sqrt{1+x} = 1 + \frac{1}{2}x + \ldots\right)$ in a Taylor series. That is, when $k_{\mathrm{ts}} \ll k_0$, the frequency shift $\Delta f = f - f_0$ can be approximated as

$$\Delta f = f_0 \frac{k_{\mathrm{ts}}}{2k_0}. \tag{3.4}$$

By definition, $\delta F_{\mathrm{ts}} = -k_{\mathrm{ts}}\delta z$ in the mass and spring model. Hence, the frequency shift Δf is proportional to the force gradient,

$$\boxed{\Delta f = -\frac{f_0}{2k_0}\frac{\partial F_{\mathrm{ts}}}{\partial z}.} \tag{3.5}$$

In summary, in FM-AFM the imaging signal is the frequency shift Δf, which is proportional to the force gradient $\frac{\partial F_{\mathrm{ts}}}{\partial z}$ in the limit of small oscillation amplitudes. As a matter of fact the frequency shift Δf corresponds to the second derivative of the potential energy U_{ts} between tip and sample.

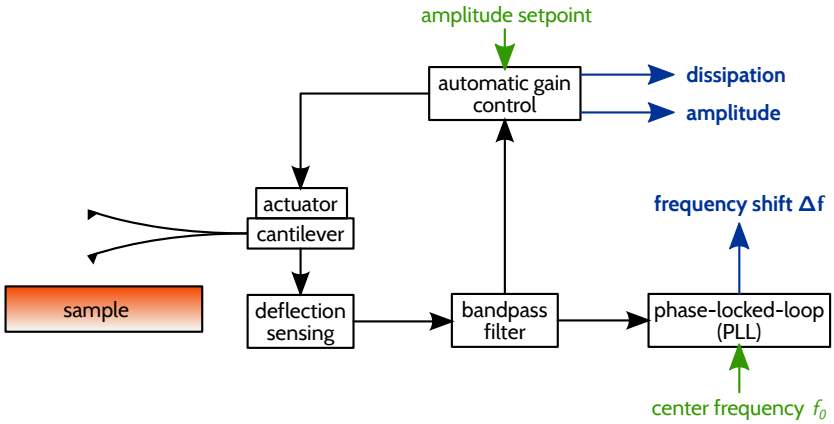

Figure 3.2.: Simplified scheme of FM-AFM. The deflection signal of the cantilever is fed into a bandpass filter, whose signal is used (i) in the PLL to determine the frequency shift Δf and (ii) in the feedback loop maintaining a constant oscillation amplitude. Input and output quantities (imaging signals) are shown in green and blue, respectively.

Figure 3.2 illustrates the working principle of the dynamic operation mode in AFM. First, the deflection signal is measured and bandpass-filtered. A phase-locked-loop (PLL) extracts the frequency shift Δf. For the sake of simplicity, details of the PLL will not be discussed here. Due to the tip-sample force and a finite Q value of the oscillator a feedback loop[3] is needed to maintain a constant oscillation amplitude by means of mechanical excitation (e. g. using a piezoelectric actuator). The actual amplitude and the dissipation signal serve as further output quantities. Obviously, the amplitude is the error signal of the feedback loop. A significant signal of the dissipation signal indicates some kind of plastic deformation on the atomic scale. That is, the tip-sample force leads to a non-conservative force. For instance, structural changes of the tip apex or the sample may occur.

[3]Note, that this feedback loop is different from the one considered for constant current measurements in STM. When analog *constant frequency shift* measurements are performed, an additional control loop is involved.

3.2. Short- and Long-Range Contributions

In section 2.2 it has been shown that the tunneling current in STM, owing to the exponential decay of the sample wave function into the vacuum, is a strictly monotonic function of the tip-sample distance. In contrast, the tip-sample force is not, as illustrated in figure 3.3. In AFM various types of forces contribute to F_{ts} differing in strength and distance dependence. In general, at large distances, attractive van der Waals forces are dominating. The smaller the tip-sample distance, the more important become repulsive contributions due to chemical forces.

Typical force contributions in UHV conditions are described in the following (in descending order of decay length[4]).

3.2.1. Van der Waals Forces

It has to be emphasized, that the term van der Waals forces is used differently depending on the text source. According to the convention by Israelachvili (*48*), which will be adopted here, intermolecular van der Waals forces include three contributions:

- orientation (Keesom) forces between two permanent dipoles,
- induction (Debye) forces between a permanent and an induced dipole,
- (London) dispersion forces between two induced dipoles.

Each of these forces is always attractive and does not vary significantly on the atomic scale. The dispersion forces are present between all atoms or molecules, because they ultimately stem from the quantum mechanical zero point energy. In general, they represent by far the main contribution to van der Waals forces[5].

[4] Technically speaking, for forces obeying a power-law, there is no well-defined decay length. It is rather a question of wether the relative contribution of a specific force increases or decreases with the tip-sample distance.

[5] A counterexample are dipole–dipole forces between H_2O molecules (*48*).

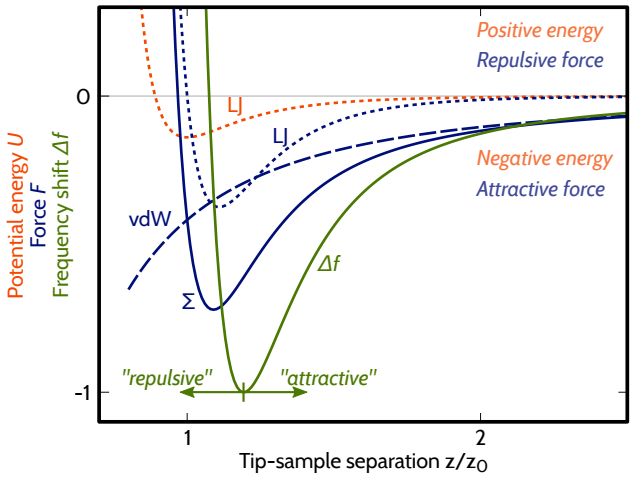

Figure 3.3.: Short- and long-range contributions in AFM. Short-range contributions are modeled by Lennard-Jones pair potential (dotted orange line) and force (dotted blue). Adding an attractive background force due to van der Waals interactions (vdW, dashed blue) yields the total force (Σ, solid blue). The resulting frequency shift Δf, approximated as the force gradient, is shown in green. The total force is only repulsive for tip-sample distances smaller than the equilibrium distance z_0. Nonetheless, it is common to distinguish between the "attractive" and "repulsive" branch based on the minimum in the frequency shift.

The distance dependence of the potential energy between two particles is given by

$$U_{\mathrm{vdW}} \propto -\frac{1}{z^6}. \tag{3.6}$$

Van der Waals forces are additive. To approximate the total (macroscopic) van der Waals force between tip and sample, a tip close to a surface is modeled as a paraboloid with local radius of curvature R near a flat surface. In this case, the van der Waals force is (*37*, *48*)

$$F_{\mathrm{vdW,ts}} = -\frac{HR}{6z^2}, \tag{3.7}$$

where z denotes the closest distance between tip and surface. The material-dependent Hamaker constant H is on the order of 2 eV to 3 eV

for typical metals (*37*). Obviously, the influence of van der Waals forces in AFM measurements can be reduced by using sharp tips.

3.2.2. Electrostatic Forces

On some particular surfaces, of e. g. ionic crystals, electrostatic forces may lead to atomic corrugations (*49*), while in general electrostatic tip-sample interactions lead to an attractive background force.

The potential difference between tip and sample, which are both conductive, leads to a capacitance $C(z)$. The resulting electrostatic force,

$$F_{\mathrm{el}} = \frac{1}{2}\frac{\partial C}{\partial z}\left(V - V_{\mathrm{CPD}}\right)^2, \tag{3.8}$$

is always attractive. This contact potential difference can be deployed for Kelvin probe force microscopy (KPFM) (*50*).

3.2.3. Magnetic Forces

The domain structure of a magnetic sample can be imaged due to dipole forces between such a sample and a magnetized tip (*51*, *52*). The magnetic force is

$$\mathbf{F}_{\mathrm{stray}} = \mu_0 \left(\mathbf{m} \cdot \nabla\right) \mathbf{H}, \tag{3.9}$$

where $\mathbf{m}$ is the magnetic moment of the tip and $\mathbf{H}$ is the magnetic stray field from the sample. This mode is called magnetic force microscopy (MFM).

Magnetic exchange force microscopy (MExFM) enables imaging of the magnetic structure of antiferromagnetic surfaces on the atomic scale (*53*). In this mode, the magnetic exchange force between a tip atom with fixed spin orientation and a sample atom is decisive.

3.2.4. Chemical Forces: Hard-Core Repulsion

At very short tip-sample distances, the electron wave functions of tip apex and sample start to overlap. Pauli's exclusion principle enforces repulsion between the respective electron clouds.

The competition between hard-core repulsion and attractive van der Waals contributions consequently defines the pair-potential of two neutral particles. While the attractive part follows equation 3.6, no universally valid distance dependence can be given for the repulsive part. For this reason one uses empiric pair potentials to model the interaction energy between two particles. The Lennard-Jones (LJ) potential (*54*) is extensively used for its ease of calculation:

$$U_{\mathrm{LJ}} = U_0 \left[\left(\frac{z_0}{z} \right)^{12} - 2 \left(\frac{z_0}{z} \right)^{6} \right], \tag{3.10}$$

where U_0 is the energy at the equilibrium distance z_0. Alternatively, an exponential distance dependence is used. Buckingham (*55*) proposed to do this only for the repulsive part[6], while the Morse potential (*56*) uses an exponential distance dependence for both, repulsive and attractive contributions:

$$U_{\mathrm{Morse}} = 2U_0 \cdot \left(1 - e^{-2\beta(z-z_0)} \right), \tag{3.11}$$

where β is a decay constant. For the LJ potential, the resulting force according to equation (3.1) is

$$F_{\mathrm{LJ}} = \frac{12U_0}{z_0} \left[\left(\frac{z_0}{z} \right)^{13} - \left(\frac{z_0}{z} \right)^{7} \right]. \tag{3.12}$$

While neither the LJ nor the Morse potential accurately describe Pauli repulsion, they can be used to illustrate the distance dependence of the tip-sample interaction qualitatively. The LJ potential and force are depicted in figure 3.3. Before calculating the frequency shift a macroscopic

[6] The decay of electron wave functions into vacuum justifies an exponential distance dependence for repulsive contributions.

van der Waals background force is added. It can be clearly seen that for large distances the frequency shift Δf is dominated by the van der Waals contributions between the (macroscopic) tip and sample. Only for small distances the (microscopic) interaction potential of the frontmost tip and sample atoms becomes significant.

In this work we are mainly interested in atomic contrast due to repulsive contributions, and section 6.1 will show that small oscillation amplitudes can be utilized to maximize the sensitivity on short-range contributions.

Part II.

Materials and Methods

4. Experimental Techniques for Instrumentation

Scanning probe investigations on single molecules as presented in the framework of this thesis can only be carried out in extreme environments. First of all, ultrahigh vacuum (UHV) conditions are essential to avoid contamination of sample surfaces by other adsorbates than the desired ones.

Ultrahigh vacuum already limits the possible materials to those with a low vapor pressure as discussed in detail below. In addition, thermal activated processes like diffusion on and desorption from the surface, have to be considered. The temperature dependence of the rate constant ν for such a process is given by the Arrhenius equation,

$$\nu = \nu_0 \cdot \exp\left(-\frac{E_a}{k_B T}\right), \tag{4.1}$$

where $\nu_0 \sim 1 \times 10^{13}\,\mathrm{s}^{-1}$ is the attempt frequency, T is the temperature, and E_a is the activation energy.

In particular on insulating surfaces, desorption is also relevant since adsorbates are only weakly bound to the substrate. It is believed that London dispersion forces and—depending on the insulator—induction forces in varying strength are responsible for adsorption (physisorption). This is in strong contrast to adsorbates on semiconductor or metal surfaces, for which strong chemical bonds play an important role (chemisorption). This leads to low activation energies for diffusion and desorption (*57*). Consequently, all SPMs discussed here are mounted to bath cryostats cooled by liquid helium. At these temperatures, materials become very stiff and, in general, the thermal conductivity decreases drastically. Hence, it is much more elaborate to equilibrate all parts at the desired temperature.

For the development of the STM head discussed in chapter 9 the high magnetic field adds additional levels of complexity: (i) magnetic forces

even on small ferromagnetic parts can easily become huge, and (ii) superconductors, which are relatively widespread at the relevant temperatures, have to be avoided. Both issues are outlined below. Many details on the experimental techniques are discussed by Ekin (*58*).

4.1. Material Selection for Ultrahigh Vacuum Applications

Achieving typical ultrahigh vacuum base pressures of $< 1 \times 10^{-10}$ mbar requires careful selection of materials with low vapor pressures. Most metals commonly used for construction are fine except for low-melting ones like lead, zinc, or magnesium, and alloys containing them. Latter, in particular, includes lead-based soldering.

However, the choice is very limited for synthetic materials. PTFE (Teflon) and polyimide (Kapton) can be used at temperatures up to 300 °C. Both are commonly used as electric-wire insulation. Another issue are joining techniques, since not only many brazing solders, but also many epoxies are not capable for UHV applications. To this end, for the STM head presented in chapter 9 we exclusively rely on EPO-TEK H20E for electrically conducting joints and EPO-TEK H77 as a thermally conductive adhesive. Both are NASA approved for low outgassing applications (*59*)[1].

4.2. Heat Transport at Cryogenic Temperatures

Thermal conductivity is well represented in a kinetic theory for electrons and phonons (*58*). It can be written as

$$\kappa = \frac{1}{3} \left(C_e v_e l_e + C_p v_p l_p \right), \tag{4.2}$$

where C, v and l are heat capacity, particle velocity and mean free path; subscripts e and p denote electrons and phonons, respectively. At

[1] The NASA manages a database (*59*) with outgassing rates of a huge amount of materials.

temperatures significantly below 1 K also contributions from the nuclear spin degrees of freedom become important.

In particular, superconductors have nearly zero thermal conductivity, since there are no states for electrons to scatter in near the Fermi level. Furthermore, they should be avoided in the construction anyhow due to their shaping-effect on the magnetic field.

The phononic term of the heat capacity is derived in the Debye model. At low temperature, the result is

$$C_p \propto \left(\frac{T}{\Theta_\mathrm{D}}\right)^3, \tag{4.3}$$

where Θ_D is the Debye temperature (for copper, $\Theta_\mathrm{D} = 343\,\mathrm{K}$ (*60*)). That is to say, phonons are mainly frozen out at low temperatures. Thus, thermal conductivity is strongly related to electrical conductivity. For this reason, ceramics and nonmetals have typically a low thermal conductivity at low temperatures. Sapphire, as a single crystalline material, stands out as a remarkable exception. Therefore, it is chosen for insulating parts which require high thermal conductivity.

The temperature dependence of the electronic contributions to heat transport is derived in the Sommerfeld model. In this model, the energy U of the electron system at temperature T is (*61*)

$$U(T) = U(0) + \frac{n\pi^2 k_B^2}{4E_F} T^2, \tag{4.4}$$

where

$$U(0) = \int_0^{E_\mathrm{F}} E\,\rho(E)\,dE \quad \text{and,} \tag{4.5}$$

$$n = \int_0^{\infty} E_\mathrm{F}\,\rho(E)\,f(E,T)\,dE. \tag{4.6}$$

This means, that the heat capacity of the electron system is

$$C_e = \frac{\partial U}{\partial T} = \frac{1}{2}\pi^2 n \frac{k_B^2}{E_F} T \propto T. \tag{4.7}$$

The electron velocity v_e at the Fermi level is independent of temperature. In very pure metals at low temperature the mean free path l_e is dominated by defect scattering, that is independent of temperature. Consequently, the temperature dependence of thermal conductivity κ of pure metals at low temperatures is given by C_e. Hence, κ is proportional to T and the purity of the material. This holds for $T \lesssim 10\,\mathrm{K}$.

4.3. Magnetic Forces

Magnetic forces acting on parts in and near a solenoid can easily become huge. The magnetic force F (in SI units) is given by

$$F = \frac{1}{\mu_0} \chi V B \nabla B, \tag{4.8}$$

where χ is the volume susceptibility, V is the volume of the part, B is the magnetic induction, and ∇B is its gradient. This is one example where relying only on intuition may cause serious problems, since not only ferromagnetic, but also some paramagnetic materials have to be avoided in critical parts. This is due to the fact that χ may change drastically with temperature[2].

In particular, many stainless steels can partially transform into ferromagnetic when cooled to cryogenic temperatures. In such a case, the magnetic force becomes huge. For this reason, gold-platings also have to be custom-made. Usually, a thin nickel layer (ferromagnetic) is used to avoid diffusion of gold into the bulk material damaging the gold-plating. Instead, a palladium layer ($\chi_{\mathrm{Pa}} = 8 \times 10^{-4}$ (*62*)) is used.

[2] E. g. "non-magnetic" austenitic stainless steel (in face-centered cubic structure, also called γ-iron) can transform into a magnetic martensitic phase (body-centered cubic, α-iron) when cooled, stressed, or welded (*58*).

5. STM on Insulating Films

The electronic properties of single adsorbates are determined by their local environment in the range of only few atomic distances. When adsorbed on conducting metal substrates, electronic states of molecules and metal strongly hybridize. However, in relation to molecular or organic electronics, one is interested in the intrinsic electronic properties of individual molecules. Therefore, an insulating surface is required.

As a matter of principle, STM and STS rely on samples with nonzero conductance. Ultrathin insulating films having a thickness of only a few monolayers on metal substrates are a way out. Electrons can still tunnel through the insulating film, but at the same time adsorbates are electronically decoupled from the substrate. A **double-barrier tunneling junction (DBTJ)** is formed. This situation is depicted in figure 5.1. In a DBTJ, an electron is first tunneling from the tip onto the adsorbate, and subsequently into the substrate, or vice versa (**sequential tunneling regime** (*63*)). This setup allows to probe the electronic levels of individual molecules by sweeping the applied bias voltage.

Note, that adsorbed molecules are apparent in an STM image even if the bias voltage does not correspond to a molecular state. Accordingly, the presence of a molecule has an impact on the tunneling barrier height, even if its density of states is zero. This finding can be explained by the concept of virtual states. Say, there exists an electronic level with energy E_n. Then, an electron with energy $E = E_n - \delta E$ may tunnel from the tip onto the molecule, and subsequently into the substrate, if it obeys the uncertainty principle $\delta E \delta t \geq \frac{\hbar}{2}$. Of course, for this process to be allowed, the time scale for tunneling from the molecule into the substrate has to be lower than δt.

The following subsections deal with several aspects specific to STM/STS investigations of molecules on insulating films. Section 5.1 addresses the

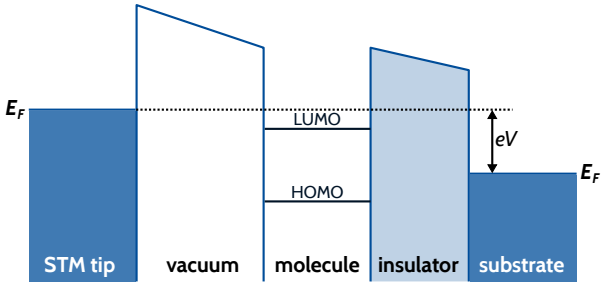

Figure 5.1.: Illustration of a DBTJ formed by an adsorbed molecule on an ultrathin insulating film grown on a metallic substrate. When scanning at this bias voltage the main contribution comes from imaging the LUMO of the molecule.

effect of Coulomb blockade in DBTJs, which explains the enlarged energy gap in STS studies between the highest occupied (HOMO) and lowest unoccupied molecular orbital (LUMO), respectively. Then, section 5.2 describes the mechanisms causing level broadening of adsorbates on conducting and insulating films, respectively. Finally, section 5.3 discusses the possibility of atom manipulation on insulating films.

5.1. Coulomb Blockade

In STS experiments on molecules on insulating films, it is observed that the HOMO-LUMO energy gap is larger than the minimal excitation energy in optical absorption measurements. The reason for that is the so-called Coulomb blockade.

For the situation of a DBTJ depicted in figure 5.2A, one might expect that electrons could tunnel from the tip into the LUMO of the molecule and subsequently into the metal substrate. This is not the case and can be explained in a simple capacitor model.

Say, one electron has already tunneled into the LUMO. Then the molecule would be negatively charged. However, the energy levels of the

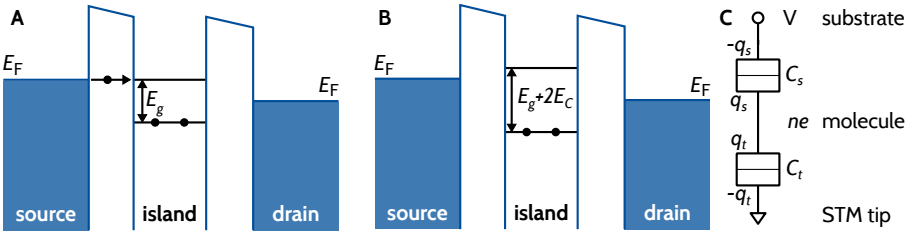

Figure 5.2.: Illustration of Coulomb Blockade in a DBTJ. **A** Two energy levels are separated by E_g. At the applied bias voltage one might expect tunneling from the source onto the island and subsequently onto the drain. **B** However, an electron tunneling from the source onto the island, which has a capacitance C, causes a voltage buildup $V = e/C$. Since the same argumentation holds for the lower level, both levels are separated by $E_g + 2E_C$. **C** Equivalent electric circuit of a DBTJ. After (*64*).

anion are not the same as for the neutral molecule due to the interaction of the additional electron with all other electrons[1]. In the simple **constant interaction model** this interaction is not treated in a quantum mechanical picture. Instead, the molecule is treated as a capacitor plate having a capacitance C with respect to the surrounding environment. Therefore, the electrostatic charging energy $E_C = \frac{e^2}{2C}$ is required to put an additional electron onto the molecule. This energy contribution is called Coulomb energy.

The DBTJ is connected to a voltage source. As a result, one has to consider the free energy F of the total system depicted in figure 5.2C, which can be expressed as the electrostatic energy U stored in the molecule minus the work $W = q_s V$ done by the voltage source (*64*, *65*),

$$F = U - W = \frac{q_t^2}{2C_t} + \frac{q_s^2}{2C_s} - q_s V, \tag{5.1}$$

where C_t, C_s, q_t, and q_s are the capacitances of tip-molecule and molecule-substrate, and the polarization charges of these capacitances, re-

[1]The equilibrium positions of the nuclei are different for the charged and neutral molecule. However, tunneling is fast and Born-Oppenheimer approximation holds. Hence, the electron attachment has to occur in the geometry of the neutral molecule.

spectively. The charge on the molecule is $ne = q_t - q_s$, and $V = \frac{q_t}{C_t} + \frac{q_s}{C_s}$. It can be shown that inserting these expressions into equation (5.1) yields

$$F(n, V) = \frac{1}{2C_\Sigma}\left[n^2e^2 + 2C_s neV_b - C_tC_sV^2\right], \tag{5.2}$$

where $C_\Sigma = C_t + C_s$.

The final state needs to be energetically favorable to enable tunneling. We can neglect two of the four tunneling possibilities in total, since the bottleneck of DBTJs considered in this thesis is tunneling from the tip onto the molecule or vice versa. In order that tunneling occurs, the final state has to be energetically favorable, that is

$$\Delta F = F(n \pm 1) - F(n) \overset{!}{<} 0. \tag{5.3}$$

From this it follows that

$$V = \pm\frac{e}{2C_s}, \tag{5.4}$$

and the corresponding Coulomb energy is

$$E_C = \pm\frac{e^2}{2C_s}. \tag{5.5}$$

That is why we find the LUMO in dI/dV spectroscopy at the position of the molecule's negative ion resonance (NIR)[2]. In other words, the level seems to be shifted by an energy of E_C (see figure 5.2B). An analog argumentation holds for the HOMO, such that the peak position of the HOMO corresponds to the positive ion resonance (PIR) of the molecule[3]. Therefore, the dI/dV signal shows an enlarged spacing between HOMO and LUMO, that can be expressed as

$$\Delta E = E_g + 2\,|E_C| = E_g + \frac{e^2}{C_s}, \tag{5.6}$$

[2]The NIR corresponds to the charged molecule in the geometry of the neutral system.
[3]For the sake of simplicity LUMO (HOMO) and NIR (PIR) will be used synonymously in this thesis.

where E_g is the energy gap seen in optical absorption spectra.

For a rough estimate of the order of magnitude, the system is modeled as a parallel-plate capacitor with a capacitance $C_s = \epsilon_0 \epsilon_r \frac{A}{d}$, where $A = 1\,\mathrm{nm}^2$ is the area of the molecular orbital, $d = 1\,\mathrm{nm}$ is the molecule-substrate distance, and $\epsilon_r \approx 10$. Hence, $e^2/2C_s \approx 1\,\mathrm{eV}$. That is, the difference between the observed HOMO-LUMO gap in STS experiments compared to optical absorption measurements is on the order of 2 eV.

For the Coulomb blockade to happen, the charging energy has to be larger than the thermal energy, that is

$$\frac{e^2}{2C} \gg k_B T. \tag{5.7}$$

By comparing the rough order of magnitude estimate from above with the thermal energy $k_B T \approx 0.5\,\mathrm{meV}$ at the temperature of liquid helium, it is clear that the condition of equation (5.7) is always fulfilled for the low temperature experiments presented in this work.

5.2. Level Broadening

The electronic states of adsorbates on metal surfaces hybridize with the electronic states of the substrate. Consequently the levels are broadened due to the reduced lifetime. This process is commonly explained in the Newns-Anderson model (*66*, *67*), which is illustrated in figure 5.3. The coupling can be expressed as a perturbing Hamiltonian Γ. For many molecule/metal systems, the resulting Lorentzian has a linewidth of $\Gamma \sim 1\,\mathrm{eV}$ (*68*).

This coupling term Γ decreases with increasing distance between adsorbate and metallic substrate. As a consequence, the lifetime-broadening is strongly reduced for adsorbates on insulating films being in the range of $\Gamma \approx 1\,\mathrm{meV}$ for a double layer of sodium chloride (*68*).

Nevertheless, due to strong electron-phonon coupling of the adsorbate states to the ionic lattice of the insulating film the levels appear significantly broadened in dI/dV spectra (*69*). As discussed above, electrons

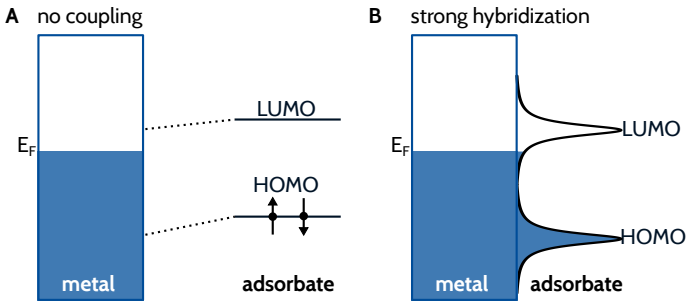

Figure 5.3.: Schematic energy diagrams illustrating the Newns-Anderson model. **A** When the adsorbate is far away from the metal it has discrete energy levels (delta function-like DOS). Upon approach the levels shift. **B** The shifted levels hybridize with metal states and are broadened into a Lorentzian. Here, the LUMO is partially filled due to broadening until below the Fermi level.

tunnel onto the adsorbate and subsequently into the sample. This means that the adsorbate is negatively charged, and then is getting discharged. This process may be inelastic, that is some of the electron's energy may be transferred in phonon energy. These vibrational-electronic (vibronic) transitions obey the Franck-Condon principle. For the systems considered here, the envelope of transition probabilities becomes a Gaussian. The linewidth depends on the electron-phonon coupling strength and can vary significantly between different insulating films (see section 7.2).

5.3. Atomic Manipulation on Insulating Films

As mentioned in the introductory chapter 1, STM allows to realize Feynman's dream of rearranging single atoms in a controlled manner. A distinction is drawn between lateral and vertical manipulation. During a lateral manipulation step the adatom stays attached to the sample all the time (*5*). In contrast, for a vertical manipulation step the adatom is picked up by the STM tip, and then released back to the surface at a desired position (*70*).

Above mentioned techniques are well established on conducting sur-

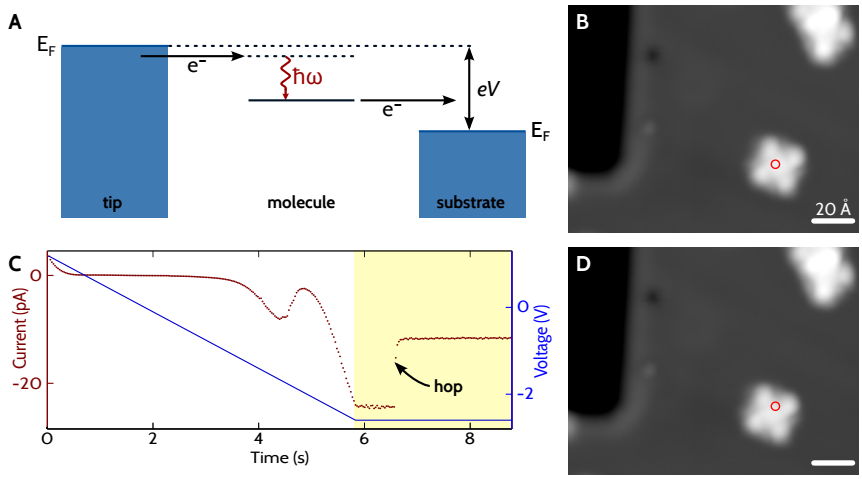

Figure 5.4.: A Illustration of vibronic excitations. Initially, the electron's energy is eV, where V is the applied voltage. If a molecular vibration of energy $\hbar\omega$ is excited, the electron's energy corresponds to an electronic level of the molecule. **B** and **D** show STM images of an individual 4NCuPc molecule before and after a hopping step ($I = 5\,\text{pA}$, $V = 1.2\,\text{V}$). The red circles correspond to the position of charge injection. **C** Tunneling current (red) and voltage ramp (blue) versus time. First, the voltage is ramped to a given value. Once this voltage is reached, it is held constant (shaded area). A sudden drop in the current signals the hopping event.

faces. However, they do not work on insulating films quite as well. A counterexample are Mn atoms vertically manipulated on insulating CuN islands (*12*). The reason for this shortcoming is that for metal adatoms on metallic surfaces the desorption barrier is roughly two orders of magnitude higher than the diffusion barrier. On insulating films, both energies are on the same order of magnitude. Therefore, to deliberately move adsorbates on insulating films a different technique is applied. While classical manipulation techniques utilize strong tip-adsorbate interaction forces, this technique employs vibronic excitations.

Therefore, vibrational energy has to be stored in the adsorbate (*71*). More precisely, the tip is positioned above the center of a molecule to be moved. Then, the feedback loop is interrupted and the bias voltage

is raised to an absolute value being at least $\hbar\omega$ higher than a given molecular level. This excess energy may excite vibrational modes of $\hbar\omega$ in the molecule, as illustrated in figure 5.4. If the stored energy is higher than the diffusion barrier, relaxation may eventually lead to a lateral movement. In such a case, the tunneling current will change. This abrupt change can be either an increase or a decrease depending on the LDOS at the point of the tip before and after the jump. If such a change occurs, the measurement will be stopped. Taking a subsequent image of the same area will resolve where the molecule has jumped to.

While vibronic excitations are highly efficient, the quantum yield of lateral movement is quite low, and at typical tunneling currents on the order of picoamperes, the time constant is on the order of seconds. We have successfully applied this technique to study the non-thermal diffusion of molecules on NaCl (*72*, *73*). In many cases a slight modification of this technique even allows to guide the molecular motion in a desired direction, albeit without atomic precision (*74*).

6. Dynamic AFM with Submolecular Resolution

In 2009 Gross *et al.* (*26*) have demonstrated the capability of AFM to visualize the chemical structure of organic molecules. Their AFM operating in the frequency modulation mode was based on a qPlus tuning fork design. In their experiments, they have shown that the tip-termination is crucial for submolecular resolution. In fact, DFT calculations have shown that Pauli repulsion is the origin of the contrast mechanism (*75*). Their breakthrough is remarkable as AFM always measures a mixture of short- and long-range forces. Beside operating the cantilever at small amplitudes (*45*), tip functionalization was the key ingredient to visualize the molecular structure.

Recently, it has been shown that such setups can also be used to probe the electric field above single molecules with submolecular resolution by means of Kelvin probe force microscopy (KPFM) (*29*). Altogether, AFM imaging, frequency shift versus distance spectroscopy and KPFM in conjunction with STM and STS provide a toolbox of experimental techniques on the atomic scale to deliver a very detailed picture of individual molecules by measuring a variety of independent properties.

We have adopted this method to visualize a configurational switch by means of AFM with submolecular resolution. These experiments will be presented in chapter 10.

In this chapter, the experimental methods are outlined, which are essential to achieve atomic contrast in AFM imaging of individual molecules. First, we examine why small amplitude operation is advantageous in section 6.1. After a short overview of the qPlus force sensor in section 6.2, the noise sources in dynamic AFM are briefly discussed in section 6.3. The chapter concludes with section 6.4 on the role of tip functionalization.

6.1. Small Amplitude Operation

As outlined in section 3.2 for small oscillation amplitudes the frequency shift Δf is proportional to the force gradient F_{ts}. It is obvious that the gradient of long-range forces is smaller as compared to short-range forces with a high slope at small distances. Giessibl (*47*) discusses the relative contribution of short- and long-range force components to the frequency shift in detail. He shows that equation (3.4) holds for oscillation amplitudes that are small compared to the range of the short-range interaction. For such amplitudes the impact of short-range force components to the frequency shift are an order of magnitude higher than the impact of long-range force components. As a matter of fact, the overall magnitude of long-range force components, which are mainly due to van der Waals interactions, can be additionally lowered when using sharp tips.

Here, we are interested in chemical forces within a single molecule. That is to say, forces with a range comparable to typical bonding lengths of 1 Å to 2 Å. Thus, above analysis shows that stable oscillation at amplitudes below 1 Å are required.

6.2. qPlus Sensor

Historically, soft silicon cantilevers with spring constants on the order of $30\,\mathrm{N\ m^{-1}}$ and eigenfrequencies on the order of 160 kHz have been used in dynamic AFM. These sensors require high oscillation amplitudes for stable operation. Hence, they are perfectly suited for probing long-range contributions, such as—to pick just one example—magnetic exchange force microscopy (*76*).

As discussed in the previous section, small oscillation amplitudes are desired to probe short-range force components. In our combined scanning tunneling and atomic force microscope (STM/AFM)[1] we use sensors based on the qPlus tuning fork design (*24*). This sensor, depicted in

[1] Design and realization of our combined STM/AFM are part of a different thesis by Neu (*77*).

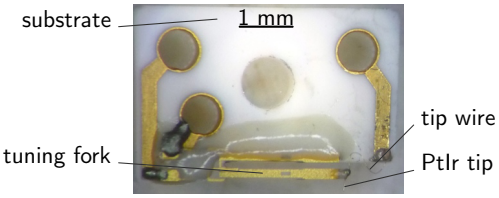

Figure 6.1.: Photograph of a qPlus sensor. The upper prong of a quartz tuning fork is glued to the ceramic substrate. Since quartz is piezoelectric, oscillation of the lower prong leads to electrical charge accumulation. This makes the qPlus sensor "self-sensing". The separate tip wire with a diameter of 10 µm, which is hard to see in the photograph, allows simultaneous STM and AFM measurements. A mechanically cut PtIr tip is glued to the end of the free prong.

figure 6.1, is ideally suited for the experiments presented in this thesis. Its high stiffness allows for stable operation at small amplitudes. Hence, even for relatively strong tip-sample interactions equation (3.4) and equation (3.5) still hold. Its high quality factor Q minimizes frequency noise (see below).

6.3. Noise Sources in Dynamic AFM

As a downside, small oscillation amplitudes cause a high vulnerability to frequency noise. According to the argumentation by Giessibl (*46*, *47*) thermal noise $\delta f_{\mathrm{thermal}}$ and detector noise $\delta f_{\mathrm{detector}}$ make up the two main contributions to frequency noise. Since both noise sources are incoherent, the total frequency noise is given by

$$\delta f = \sqrt{\delta f_{\mathrm{thermal}} + \delta f_{\mathrm{detector}}}. \tag{6.1}$$

6.3.1. Thermal Noise

The thermal noise of a cantilever is given by (*9*)

$$\frac{\delta f_{\mathrm{thermal}}}{f_0} = \sqrt{\frac{2k_B T B}{\pi f_0 k_0 A^2 Q}}, \tag{6.2}$$

where B is the bandwidth, A is the oscillation amplitude, k_BT the thermal energy, and $k_0A^2/2 = kA_{rms}^2$ is the mechanical energy stored in the cantilever.

Our experiments are performed at temperatures of about 5 K. Intuitively, thermal noise should not play a significant role at cryogenic temperatures. However, we also aim to minimize the oscillation amplitude A, so it is better to explicate an order of magnitude estimate. The sensor used for the experiments presented in chapter 10 has a quality factor of $Q \sim 10^4$ and an eigenfrequency of $f_0 = 26\,057$ Hz (see also section 7.1). Say, we operate the cantilever at an oscillation amplitude of $A = 1$ Å and assume a bandwidth of ~ 10 Hz. Then, the thermal noise is about $\delta f \approx 2.6$ mHz or $\delta f_{\text{thermal}}/f_0 \approx 10^{-7}$. These numbers are indeed small compared to the atomic contrast on the order of some 0.1 Hz (corresponding to $\delta f/f_0 \gtrsim 4 \times 10^{-6}$) seen in typical AFM images.

6.3.2. Detector Noise

Detector noise is a measure of how accurate the deflection of the cantilever can be determined. In our setup this accounts for the complete sensing setup including the phase-locked loop (PLL) measuring the frequency shift. This noise shows up in the frequency shift as (*45*, *78*)

$$\frac{\delta f_{\text{detector}}}{f_0} = \frac{n_{q'} B_{\text{FM}}^{3/2}}{\pi A f_0}, \tag{6.3}$$

where $n_{q'}$ is the deflection noise density given in fm $\text{Hz}^{-1/2}$ and B_{FM} is the bandwidth of the frequency detector. Hence, slow scanning significantly reduces the noise in the imaging signal.

To give some real-world numbers, the deflection noise density $n_{q'} \approx (17 \pm 1)$ fm $\text{Hz}^{-1/2}$ in our setup[2] (*77*). The total noise in typical KPFM

[2] That is, for a bandwidth of 100 Hz the deflection of the cantilever can be determined with a precision of 17 pm, which is still significantly smaller than a typical "small" oscillation amplitude of 50 pm.

spectra corresponds to 3 meV in energy or 20 mHz in frequency shift for an oscillation amplitude of $A \approx 0.5$ Å.

Both noise sources discussed above scale with the bandwidth B. From this it follows that slow scanning speeds significantly reduce the total frequency noise δf. Accordingly, the AFM images presented in chapter 10 are acquired at scanning speeds lower than 10 Å/s. For this reason, STM mode allowing much higher scanning speeds is used for large overview scans and to find interesting spots on the surface. Only, after the image frame is fixed, and proper plan-substraction has been confirmed, AFM imaging is started to efficiently use measurement time.

6.4. Tip Functionalization

Gross *et al.* (*26*) have shown that tip functionalization is a basic requirement to visualize the chemical structure of individual molecules. DFT calculations (*75*) have proved that the submolecular contrast originates from the Pauli exclusion principle (*79*). Significant contributions due to Pauli repulsion can only be measured for small tip-sample distances. Therefore, the tip apex has to be chemically inert. In particular, this applies for single molecules on insulating films, which are only weakly bound to the substrate (see chapter 4).

Originally, either a single CO molecule, Cl atom, or pentacene molecule have been used as tip terminations. In addition, we have also acquired atomic and submolecular contrast with a single Xe atom (*80*) at the tip. For the experiments on the configurational switch presented in chapter 10, CO molecules have been used. In general, localized wave functions like the π orbitals of CO enable a high lateral resolution. Experimentally, it is advantageous to use CO molecules, since tip preparation is well-known and straightforward (see section 7.2.2).

In dynamic AFM a CO tip-termination enables visualization of the chemical structure of molecules. In this case it is decisive that CO is inert. Hence, the tip apex stays stable even when the wave functions

of tip and molecule start to overlap and chemical contrast due to Pauli repulsion emerges (see section 3.2.4).

In STM mode a CO-terminated tip also leads to different imaging contrast as compared to metal tips. Its π-orbitals strongly enhance the p-wave character of the tip as compared to clean metal tips. For metal tips the s-wave character dominates since these states expand further into vacuum (*40*, *41*). This fact can also be rationalized by equation (2.10) and equation (2.11). The same Fourier expansion as for the sample wave function can be used for the tip wave function. Then, it is clear that high k values lead to a faster decay into the vacuum.

According to Chen's derivative rule (*37*), the tunneling matrix element for p-wave tips is proportional to the lateral derivative of the local density of states, that is

$$M_{p_x} \propto \frac{\partial \Psi}{\partial x}, \tag{6.4}$$

$$M_{p_y} \propto \frac{\partial \Psi}{\partial y}. \tag{6.5}$$

This has been demonstrated recently by Gross *et al.* (*81*). We have employed this technique for the experiments presented in chapter 11.

7. Experimental Setup and Sample Preparation

7.1. Experimental Setup

The experiments presented in chapters 10 and 11 were carried out in two different setups. Both are based on a design developed and improved by Meyer (*82*) and later commercialized by Zöphel (*83*). The first setup is a modified commercial STM from SPS-Createc GmbH (*84*), whereas the second one is a homebuilt combined STM/AFM. Both setups only differ in the heart of the microscope head, but are otherwise compatible to each other. This enables the use of same samples in both machines, and obviously facilitates handling.

A photograph of the STM/AFM apparatus is shown in figure 7.1. A combination of a turbomolecular pump, an ion pump and a titanium sublimation pump provides a base pressure better than 1×10^{-10} mbar.

A gate valve makes it possible to separate the STM chamber from the preparation chamber. The preparation chamber holds an ionization gauge, a sample storage, as well as the equipment for sample preparation, namely the alkali halide evaporator and a sputter gun. Both the ion pump and the titanium sublimation pump are attached to the preparation chamber. Additionally, it is possible to connect a quadrupole mass spectrometer.

The load lock is attached to the preparation chamber on the back side. It can be pumped separately from the rest of the chamber by the turbo molecular pump. Therefore, it is possible to transfer samples and evaporators without breaking the vacuum. Transferable evaporators are used to deposit metal atoms or organic molecules, respectively, on the cleaned sample.

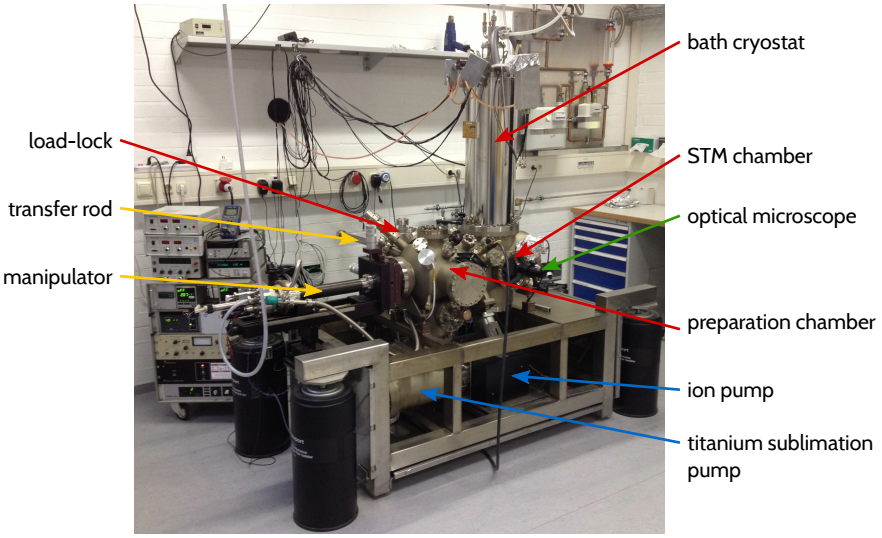

Figure 7.1.: Photograph of UHV apparatus. On the left-hand side the manipulator is connected to the preparation chamber. On the right-hand side are the STM chamber, and, on top of it, the bath cryostat. The load-lock is located on the back.

The manipulator can be cooled with liquid nitrogen (LN_2) or liquid helium (LHe). This makes it possible to prepare and transfer samples at low temperatures. Furthermore the sample can be heated independently using a small oven, on which the single crystal is installed. This is essential in order to grow alkali halides in a wide temperature range.

The bath cryostat consists of an LN_2 and an LHe tank with a capacity of 15 l and 4 l, respectively. The microscope is suspended from springs, which are attached to the bottom of the LHe cryostat, to achieve good mechanical vibration isolation. Resonant oscillations of the springs are damped by an eddy-current brake. For thermal isolation, the microscope is surrounded by two radiation shields at the temperature of LN_2 and LHe, respectively.

Using the manipulator, samples can be transferred in and out of the microscope. Deposition of organic molecules or metal atoms onto the

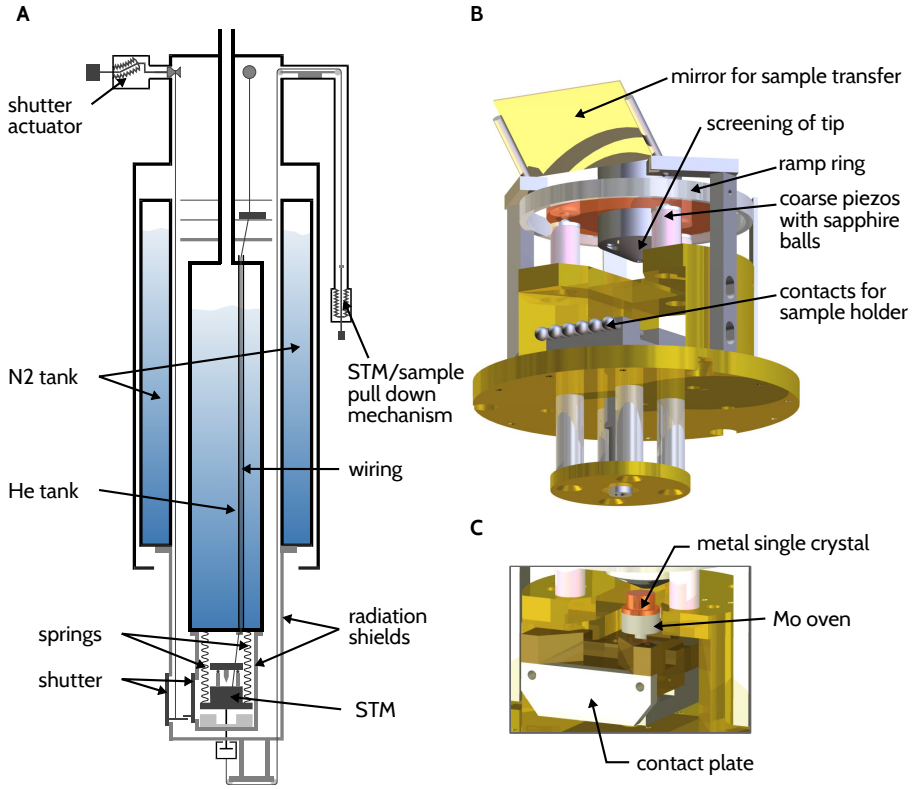

Figure 7.2.: A Cross-section of bath cryostat. **B** Three-dimensional model of beetle-type scan head in Createc design. In this picture the STM is pulled down for sample transfer. Panel **C** shows a sample holder placed in the scan head.

sample is carried out *in situ*. That is, the sample remains in the microscope during the evaporation process. For this purpose an evaporator is positioned in front of the microscope. Then, a pair of small shutters in each radiation shield (not shown in figure 7.2A) is opened, while the molecules or atoms are thermally sublimed.

The Besocke beetle-type design principle of the scanner is well-known for its inherent mechanical stability (*85*). A three-dimensional computer-aided design (CAD) model of the microscope is shown in figure 7.2B. The tip is mounted to a ring which has three ramps on the bottom

(ramp ring). The coarse movement of the tip is based on inertial sliding of the ramp ring on the sapphire balls of the outer piezos. To this end, cycles of stick and slip motion are triggered by a suitable sawtooth voltage applied simultaneously to all piezos. Displacing all piezos in the same direction results in lateral movement (x, y), while moving tangentially (circular motion of the ramp ring) results in the coarse approach (z).

In the pure STM setup the tip is attached to a fourth identical tube piezo (not seen in figure 7.2B). The use of four identical piezos results in a very good thermal compensation. In the combined STM/AFM setup the qPlus sensor (see section 6.2) is mounted to the fourth piezo. In this case, the central piezo is used to drive the cantilever oscillation, and the outer piezos are used for z movement.

The AFM is operated in the frequency modulation mode (*9*) (see section 3.1). The qPlus tuning fork sensor (*24*) used for the experiments presented in chapter 10 had a spring constant $k_0 \approx 1.8 \times 10^3\,\mathrm{N\,m^{-1}}$, a resonance frequency $f_0 = 26\,057\,\mathrm{Hz}$, and a quality factor $Q \approx 10^4$. Following the discussion in section 6.1 sub-Ångstrom oscillation amplitudes have been used to maximize the lateral resolution (*45*).

7.2. Sample and Tip Preparation

This chapter is intended to present the relevant properties of the substrate systems, on which all experiments have been conducted. Subsequently, the procedure to create CO-functionalized tips is presented.

7.2.1. Substrate Systems

All experiments have in common that clean copper single crystals were used. The copper surfaces were cleaned in the preparation chamber by several cycles of Ne^+ sputtering (10 min to 20 min at an ion energy of 1 keV) and subsequent annealing up to 830 K.

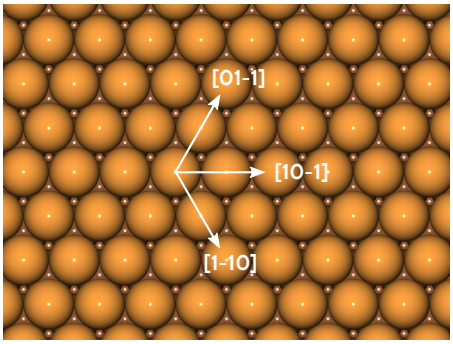

Figure 7.3.: Ball model illustrating sixfold symmetry of Cu(111) surface. The close-packed directions are shown.

The electron-phonon (*e-ph*) coupling, which is responsible for the energy broadening in STS (see section 5.2), differs significantly for the insulating films used in this work. The best energy resolution can be achieved on Xenon islands with a line width of $\Gamma_{\mathrm{Xe}} \approx 0.1\,\mathrm{eV}$. For rubidium iodide the line width is $\Gamma_{\mathrm{RbI}} \approx 0.15\,\mathrm{eV}$, while for sodium chloride it rises to $\Gamma_{\mathrm{NaCl}} \approx 0.3\,\mathrm{eV}$. In general, it is advantageous to work on a substrate system with the best possible energy resolution. However, it turns out that the *e-ph* coupling strength scales with the polarizability of the substrate giving rise to some ionic contributions to the adsorption energy. For this reason, adsorbates are less mobile on NaCl as compared to RbI and Xe. Therefore, experiments which require long measurement times have been performed on substrates with higher line width (NaCl, RbI). Only, if the energy resolution is crucial, Xe is used as a substrate.

NaCl(100) on Cu(111)

Cu(111) is a close-packed surface and its close-packed directions are denoted as $[01\bar{1}]$, $[1\bar{1}0]$ and $[10\bar{1}]$ (as illustrated in figure 7.3). The distance between two neighboring atoms is $a_{\mathrm{Cu}}/\sqrt{2} = 2.55\,\text{Å}$. The (111) surfaces of noble metals exhibit a Shockley surface state (*86*). For Cu(111) the band minimum is 450 mV below the Fermi energy.

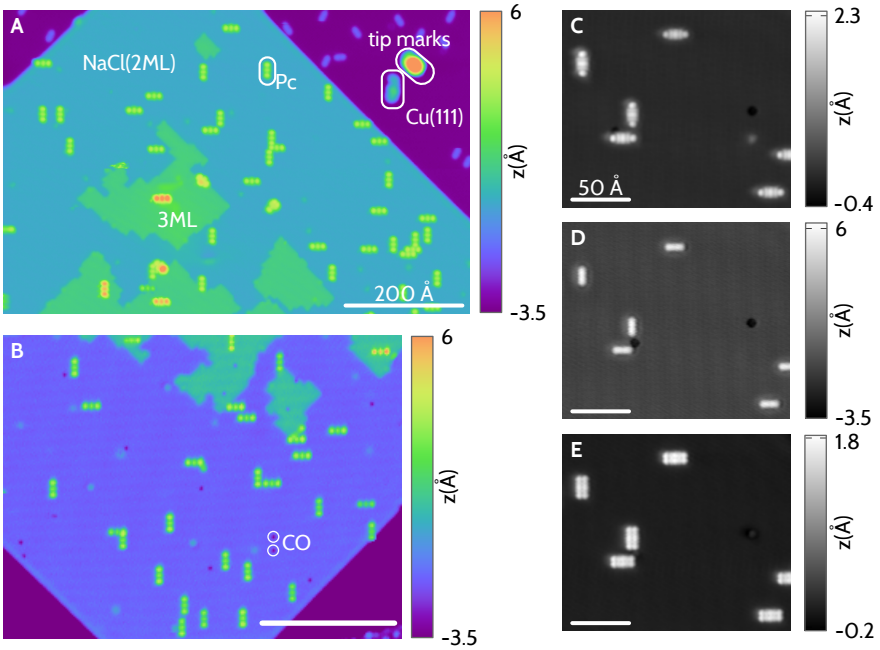

Figure 7.4.: Typical STM images of NaCl/Cu(111) sample preparation. **A** Pentacene (Pc) molecules on a mainly 2ML thick island of NaCl ($V = 1.5\,\mathrm{V}$, $I = 2\,\mathrm{pA}$). It shows straight nonpolar edges. Some smaller islands of a third layer (3ML) of NaCl are on top of the bilayer. The tip had been indented into the bare copper surface at the indicated positions (tip marks) to get a sharp metal tip. **B** Similar STM image acquired with a CO-terminated tip. CO molecules for tip-preparation show up as depressions ($V = 1.4\,\mathrm{V}$, $I = 0.6\,\mathrm{pA}$). **C-E** Bias-dependent imaging of pentacene molecules with a CO-terminated tip ($I = 2\,\mathrm{pA}$). Voltages correspond to the onset of the LUMO (**C**, $V = 1.3\,\mathrm{V}$), the HOMO-LUMO gap region (**D**, $V = 1.1\,\mathrm{V}$), and the onset of the HOMO (**E**, $V = -2.2\,\mathrm{V}$).

During epitaxial growth of (100)-terminated islands of NaCl the sample has been kept at a temperature of 10 °C. At this deposition temperature the NaCl islands formed have a width of up to several hundreds of Ångstrom. The islands have nonpolar edges and grow immediately as a double layer. Different domains of growth directions can be distinguished (*87*). For the experiments presented in this thesis the coverage was significantly below one monolayer (meaning that less than half of the sample surface is covered with a bilayer of NaCl).

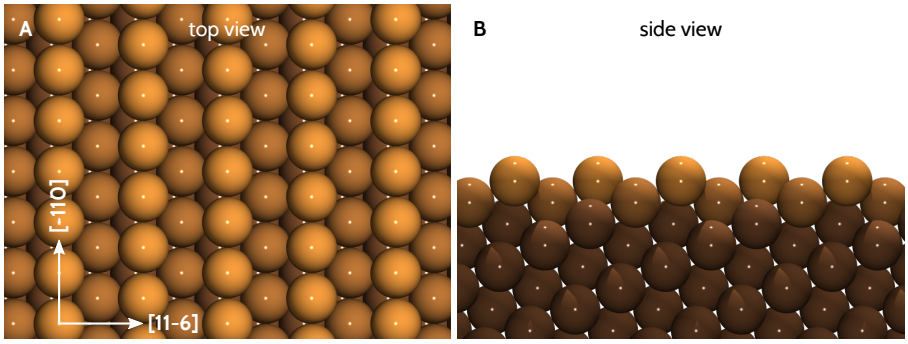

Figure 7.5.: Ball models illustrating Cu(331) surface. Intrinsic step edges along the $[\bar{1}10]$ direction can be seen. Atoms in three topmost layers are colored differently for clarity.

The lattice constant of NaCl is $a_{\mathrm{NaCl}} = 5.64\,\text{Å}$ at room temperature, which gives a nearest-neighbor distance between atoms of the same ionic species of $a_{\mathrm{NaCl}}/\sqrt{2} = 3.99\,\text{Å}$. At a sample temperature of $T \approx 8\,\mathrm{K}$ the lattice of NaCl/Cu(111) is compressed by 2% compared to the lattice constant at room temperature (*87*).

Where the Cu(111) is covered with a double layer of NaCl the Cu(111) Shockley surface state band turns into an interface state band. The band minimum shifts to $230 \pm 30\,\mathrm{mV}$ (*88*). All adsorbates, regardless of their charge state, on the bare Cu(111) surface lead to scattering of surface state electrons. However, only the long-range Coulomb potential of charged adsorbates on the insulating film acts as a scattering potential for the interface state electrons. This phenomenon can be employed to measure the charge state of adsorbates (*89*, *90*).

RbI(100) on Cu(331)

The Cu(331) surface, which serves as a substrate for ultrathin (100)-terminated RbI films, consists of alternating monoatomic (111) and (100) nanofacets, as illustrated in figure 7.5. The resulting intrinsic step edges are aligned along the $[\bar{1}10]$ direction. Neighboring rows are separated by a distance of $\sqrt{38}/4 \cdot a_{\mathrm{Cu}} = 5.56\,\text{Å}$, while two neighboring atoms

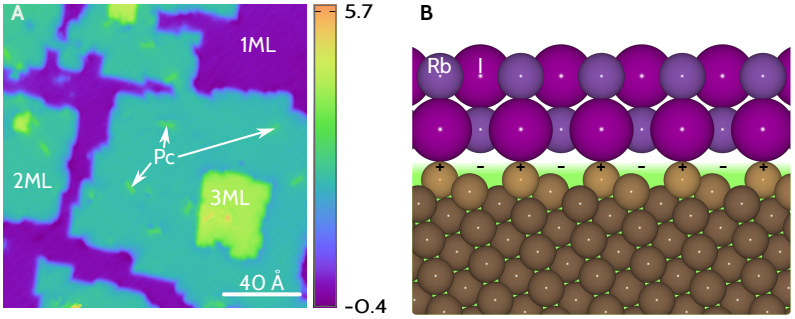

Figure 7.6.: A Typical STM image of RbI/Cu(331) substrate system. Regions of 1ML to 3ML coverage and some pentacene molecules (Pc) are indicated. No bare Cu(331) is visible since it is covered by a RbI wetting layer (indicated as 1ML). $V = 0.2\,\mathrm{V}$, $I = 2\,\mathrm{pA}$. **B** Schematic model of RbI on Cu(331). The Smoluchowski smoothing effect leads to surface dipoles. Consequently, I anions favor kink atoms, and Rb cations sit between intrinsic step edges.

in a row are separated by $a_{\mathrm{Cu}}/\sqrt{2} = 2.55\,\text{Å}$.

Similar to NaCl/Cu(111), (100)-terminated RbI islands are grown on Cu(331). During the evaporation process the sample is kept at a temperature of 0 °C; after this step it is annealed to 40 °C and kept at this temperature until the sample has been transferred into the STM. In contrast to NaCl/Cu(111) the first RbI layer grows as a single wetting layer. Thus, the coverage has to be well above one monolayer to get sufficiently large areas covered with a second layer of RbI[1].

The lattice constant of RbI is $a_{\mathrm{RbI}} = 7.34\,\text{Å}$, which yields a nearest-neighbor distance of atoms of the same ionic species of $a_{\mathrm{RbI}}/\sqrt{2} = 5.20\,\text{Å}$. The growth of related systems has been studied in detail (*91*, *92*). It is expected and consistent with experimental results, that RbI on Cu(331) grows in an analog manner. Accordingly, the I anions are located on top of intrinsic Cu step edges, as illustrated in figure 7.6B, which carry a positive charge due to the Smoluchowski smoothing effect (*93*). This goes along with significant strain, since the distance

[1] Only a bilayer of RbI ensures that adsorbates are thoroughly electronically decoupled.

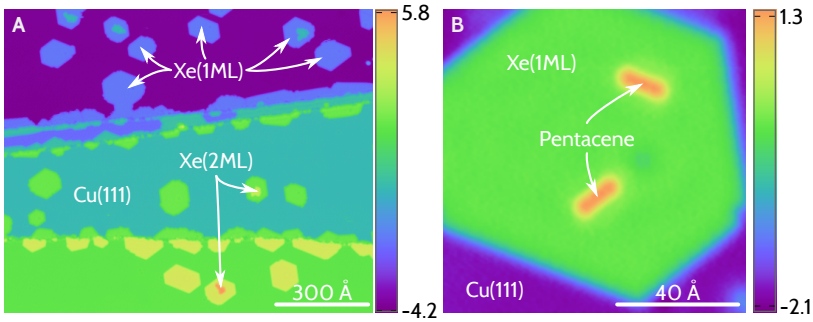

Figure 7.7.: Typical STM images of a Xe/Cu(111) sample preparation. **A** Regions of bare Cu(111) and 1ML and 2ML thick Xenon islands are indicated ($V = 0.4\,\mathrm{V}$, $I = 2\,\mathrm{pA}$). **B** Two pentacene molecules on a 1ML thick Xenon island ($V = 0.2\,\mathrm{V}$, $I = 0.4\,\mathrm{pA}$).

between intrinsic step edges is about $1.07 \times a_{\mathrm{RbI}}/\sqrt{2}$ at room temperature.

Xe(100) on Cu(111)

Xe films were formed by adsorption on Cu(111) while the sample was inside the STM below 15 K. A background Xe pressure of typically 2×10^{-5} mbar was maintained in the UHV chamber for 30 s. This results in mainly monolayer-islands of Xe of hexagonal shape on the bare Cu(111) surface (*94*, *95*).

The experiments on Xe islands presented in chapter 11 have been performed exclusively on one monolayer thick islands.

7.2.2. Tip Functionalization

Controlled vertical manipulation of individual CO molecules from and back onto copper surfaces has been demonstrated already in 1997 by Bartels, Meyer, and Rieder (*96*). A characteristic contrast change when imaging further CO molecules signals that a single CO molecule has been successfully transferred to the tip apex. In recent years this method

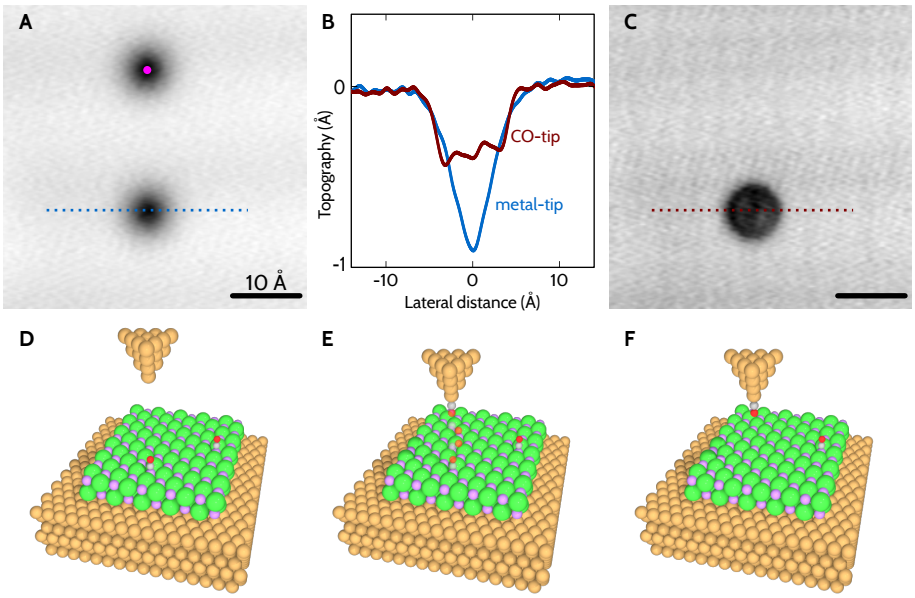

Figure 7.8.: CO tip-functionalization on NaCl(2ML)/Cu(111). **A** and **C** correspond to constant current STM images before and after picking up one of the CO molecules ($V = 0.4\,\mathrm{V}$, $I = 1\,\mathrm{pA}$). In between the tip was approached at $V = 0.05\,\mathrm{V}$ by 5 Å with respect to the STM set point of panel **A**. The circle indicates the tip position during approach. **B** Topographic line scans across the second CO molecule as indicated by the dotted lines in panels **A** and **C**. Panels **D**-**F** illustrate the procedure: a clean metal tip is positioned above a CO molecule (**D**); upon approach (**E**) the CO molecule transfers to the tip (**F**). This step is accompanied by a rotation of 180° (that is, the O atom sticks out in both cases).

has been deployed for AFM (*26*) and STM (*81*) studies of individual molecules[2].

It is also possible to pick up single CO molecules from ultrathin NaCl films on copper surfaces[3], as presented in figure 7.8. Therefore, the tip is positioned to be above the center of a CO molecule. Then, the tip is

[2]Recently, a reverse setup with the CO molecule adsorbed on a Cu(111) surface probing tungsten tip clusters has been employed to identify the tip cluster by its angular symmetry of chemical bonds (*30*).

[3]Since transferring CO molecules back onto the NaCl film is not as reliable this is no example for controlled vertical manipulation on insulating surfaces.

approached by a few Ångstroms.

For the experiments presented in chapter 10 and chapter 11, CO molecules were adsorbed at sample temperatures below 10 K by maintaining a background CO pressure of typically 2×10^{-5} mbar in the UHV chamber for about 2 s. The coverage was chosen to be far below one monolayer. Before functionalizing the tip apex with a CO molecule, a clean metal tip has to be prepared by indenting the tip into the bare copper surface. During this procedure voltages up to 10 V are applied such that currents on the order of a few microamperes are established. It is believed that this modus operandi results in local melting due to the high current density. Consequently, it is expected that the resulting tip apex is covered by copper. Only, when STM images prove that the tip is sharp and symmetric (e. g. CO molecules appear circular) one tries to pick up a CO molecule as illustrated in figure 7.8. In the combined STM/AFM a small frequency shift Δf is an additional quantitative measure for a sharp tip (that is, small van der Waals interactions, see section 3.2).

8. Density Functional Theory Calculations

In conjunction with the experiments presented in chapter 10 of this thesis, density functional theory (DFT) calculations of individual thianthrene (TH), dibenzo[a,h]thianthrene (DBTH), and dinaphtho[a,j]thianthrene (DNTH) molecules have been performed. These calculations verified the initial assumptions of the molecular geometry. Furthermore, the calculations provided numbers for the relevant energy scales.

In the introductory section, I will first present the fundamental idea behind DFT. A detailed overview of DFT goes beyond the scope of this thesis, so this discussion will be very briefly. The subsequent section then presents the computational details for the series of above mentioned molecules.

8.1. Introduction

DFT is a well-established method in physics and chemistry to calculate the ground state properties of many-body systems (*97*, *98*). It is based on the **Hohenberg-Kohn Theorem** (*99*). This theorem states that the ground-state density $n(\mathbf{r})$ of a system of interacting electrons in some external potential $v(\mathbf{r})$ determines this potential uniquely.

As the external potential $v(\mathbf{r})$, in turn, specifies all physical observables, it is possible—at least in principle—to determine all physical parameters from the electron density $n(\mathbf{r})$ alone. The many-body problem depending on $3N$ coordinates is therefore formally reduced to finding the electron density $n(\mathbf{r})$ depending only on the three spatial coordinates.

In practice, the problem is usually solved in a self-consistent cycle for the single-particle equations

$$\left(-\frac{1}{2}\nabla^2 + v_{\text{eff}}\left(\mathbf{r}\right) - \epsilon_j\right)\phi_j\left(\mathbf{r}\right) = 0, \tag{8.1}$$

where

$$n\left(\mathbf{r}\right) = \sum_{j=1}^{N}\left|\phi_j\left(\mathbf{r}\right)\right|^2, \tag{8.2}$$

$$v_{\text{eff}}\left(\mathbf{r}\right) = v\left(\mathbf{r}\right) + \int \frac{n\left(\mathbf{r}'\right)}{\left|\mathbf{r}-\mathbf{r}'\right|}dr' + v_{\text{xc}}\left(\mathbf{r}\right). \tag{8.3}$$

The ground-state energy is then given by

$$E = \sum_j \epsilon_j + E_{\text{xc}}\left[n\left(\mathbf{r}\right)\right] - \int v_{\text{xc}}\left(\mathbf{r}\right)n\left(\mathbf{r}\right)d\mathbf{v} - \frac{1}{2}\int \frac{n\left(\mathbf{r}\right)n\left(\mathbf{r}'\right)}{\left|\mathbf{r}-\mathbf{r}'\right|}. \tag{8.4}$$

Equations (8.1)–(8.4) are called the Kohn-Sham (KS) equations (*100*), where v_{xc} is the local exchange-correlation potential, and $E_{\text{xc}}\left[n\left(\mathbf{r}\right)\right]$ is the exchange-correlation energy.

The accuracy of DFT is now determined by the exactness of approximating E_{xc} and v_{xc}. In theory, given the exact exchange-correlation, the ground-state energy would be exact. In fact, approximating the exchange-correlation part is the crucial task. Among the most common approximations for E_{xc} are the local-density approximation (LDA) and many forms of the generalized gradient approximation (GGA).

The HOMO-LUMO gap Δ of molecules is often approximated as the eigenvalue difference of the corresponding Kohn-Sham eigenstates (orbitals) based on Koopman's theorem (*101*). This mapping is not justified from theory, and usually underestimates the gap in the GGA formalism. A better estimate of the gap can be achieved in the self-consistent field method (*102*) by calculating the total energy difference between the neutral and the charged system (both in the relaxed geometry of the neutral system):

$$\Delta = E_0(N) - E_0(N+1), \tag{8.5}$$

where $E_0(N)$ corresponds to the energy of the neutral molecule in its optimized geometry and $E_0(N+1)$ corresponds to the energy of the molecule with an extra electron added in the geometry of the neutral system. This treatment is also intuitive in the case for STM experiments in a DBTJ. As a consequence of the Born-Oppenheimer approximation, electron injection into the LUMO of a given molecule occurs in the geometry of the neutral molecule. This directly reflects the situation of Coulomb blockade as discussed in section 5.1.

8.2. TH, DBTH and DNTH molecules

In conjunction with the experiments presented in chapter 10 we have performed DFT calculations for free DBTH calculations using the highly optimized `CPMD` code (*103*). To get a more systematic view of the chemical mechanisms, similar calculations have been performed for the highly related molecules TH and DNTH. Prior to these runs, the validity of all parameters has been verified by calculating the structure of the well-known pentacene molecule (*104–107*).

A plane-wave cut-off energy of 130 Ry (≈ 1.8 keV) was used in all cases. PBE (Perdew-Burke-Ernzerhof) exchange correlation functionals (*108*) and *ab-initio* norm-conserving pseudopotentials (*109*) were applied.

We have deliberately chosen above mentioned parameters for several reasons:

1. It was known from previous studies that similar parameters have proven to yield reliable geometries for other organic molecules (*26*, *75*).
2. While hybrid functionals might yield more accurate values of absolute energies, they require much more computing power. All calculations using the PBE functional could be carried out on a standard desktop computer within less than 24 hours.
3. The molecules under study are computationally unproblematic in a sense that they e. g. do not contain any transition metal centers which are known for high self-interaction errors when using PBE

Table 8.1.: DFT calculated properties of TH, DBTH, DNTH, and pentacene molecules. For each molecule the folding angle and the cell size of the calculation are given.

Molecule	Folding Angle Θ	Cell size (Å^3)
TH	137.4°	17.0×13.6×17.0
DBTH	134.6°	24.0×24.0×24.0[a]
		18.0×16.2×9.0[b]
DNTH	155.4°	24.0×14.4×14.4
Pentacene	180.0°	24.0×12.0×14.4

[a] Determination of molecular geometry.
[b] Determination of energy vs. Θ dependence.

or related functionals in the generalized-gradient approximation (see for example Rappoport *et al.* (*110*)).

The molecular structure has been found by minimizing the total energy and relaxing the ions until the forces on all atoms were below $5 \times 10^{-4}\, E_\mathrm{h}/a_0$ ($\approx 40\,\mathrm{pN} \approx 2.1\,\mathrm{meV/Å}$)[1].

An important quantity of the molecules studied here, TH, DBTH, and DNTH, is their dihedral angle Θ[2]. Poly-aromatic hydrocarbons consisting only of C and H atoms (e. g. pentacene) are planar. Exchanging a C-H group for a S atom in such a molecular structure—i. e., incorporating a thioether group—leads to a folding of molecules (*111–116*). This is due to two lone pairs (that is four non-bonded electrons) of the S atoms.

Structure Determination

In a first step, we have optimized the structure for TH, DBTH, and DNTH molecules by relaxing all atoms. To check the validity of our input parameters, the structure of the well-known pentacene molecule

[1] Atomic (Hartree) units are internally used in `CPMD`.
[2] The dihedral angle corresponds to the angle between the normal vectors of two planes defined by the outer benzene units. In this work, folding angle is used synonymously.

has also been determined. The cell size for each calculation is given in table 8.1. All cell sizes are relatively large compared to the size of the molecules. This was done to enable comparison of STM orbital images at low currents (large tip-molecule distances correspond to a contour of low constant electron density) with corresponding Kohn-Sham orbitals at low isovalues.

Energy versus Folding Angle Θ of DBTH

There is no preferential direction of folding for free molecules (or molecules in gas phase). However, adsorption on a surface will break this symmetry. For instance, TH and its derivatives may adsorb with either side up or down. For this reason, we have also calculated the energy barrier for flapping between both configurations.

To this end, we have optimized the geometry for fixed dihedral angles ranging from 90° to 183°. That is, the atoms may relax with the constraint that the dihedral angle as defined in figure 10.1 is fixed. For this series of calculations we have chosen a smaller cell size (see table 8.1) to reduce computation time.

The results of the calculations described here will be presented in connection with the respective experiments on DBTH molecules in section 10.2.

Part III.

Results

9. Design of an STM Head for Use in High Magnetic Fields

> Everything should be made as simple as possible, but not simpler.
>
> *(Albert Einstein)*

This chapter presents design, construction and build-up of an STM head for use in high magnetic fields.

In the last years many fascinating experiments on spin manipulation on the atomic scale have been performed (*11–13*, *15*, *16*, *117*). All these experiments require high magnetic fields. Another exciting experiment would be the realization of an Aharonov-Bohm interferometer in an STM setup, a prospective experiment recently proposed by Cano and Paul (*118*).

For the experiments presented in chapters 10 and 11 STM heads based on the Besocke design (*85*) have been applied. While their performance is great with respect to thermal drift compensation, high magnetic fields on the order of 10 T are nearly incompatible with Besocke-type microscope heads for several reasons:

- The high magnetic fields are realized by superconducting solenoids with a small bore with a diameter of typically $2\,\text{inch} = 50.4\,\text{mm}$[1]. Typical Besocke designs are simply too large to fit inside the bore.
- Due to their design they have usually low eigenfrequencies. Therefore, they are suspended from long springs and eddy-current damping is used for vibration isolation. As a matter of principle eddy-current damping is not possible inside the bore of a solenoid. In principle, it is possible to relocate the damping stage outside the bore. However, this comes along with high experimental effort.

[1] Solenoids with larger bores are much more expensive at the same maximum magnetic field.

- Finally, magnetic forces are a severe issue. In particular, the ramp ring is held solely by gravity.

Section 9.1 introduces the magnet cryostat, in which the STM head is to be mounted. After presenting the design goals of the STM head in section 9.2, its realization is discussed in section 9.3.

9.1. Magnet Cryostat

The Zeeman energy for a single spin-flip excitation is

$$\Delta = g\mu_B B, \tag{9.1}$$

where $g = 2.0023$ for a free electron and $\mu_\mathrm{B} = 57.9\,\mathrm{eV/T}$ is the Bohr magneton. For a magnetic field of 9 T the Zeeman energy $\Delta \approx 1\,\mathrm{meV}$. Thermal broadening leads to a line width of $5.4k_\mathrm{B}T$ in STS data (*119*). Therefore, only for temperatures $\lesssim 2\,\mathrm{K}$ thermal broadening is small enough to resolve spin-flip events in STS[2].

To this end, the STM head is to be mounted in the magnet cryostat presented in figure 9.1. This cryostat mainly differs in two key aspects from the 4 K cryostats used in the existing apparatuses of our research group:

Magnetic field
A superconducting solenoid provides magnetic fields perpendicular to the sample surface of up to 9 T.

1-K pot
A so-called 1-K pot allows to attain temperatures of about 1.3 K. For this purpose, a small vessel is filled with liquid helium. Evaporative cooling is applied to lower the vapor pressure of liquid helium in the 1-K pot and hence its temperature.

[2]The experiments in chapter 11 are performed at 5 K, although the relevant energy scales are on the order of 100 meV. In this case low temperature suppresses surface diffusion and enables high thermal stability of the STM junction (cf. chapter 4).

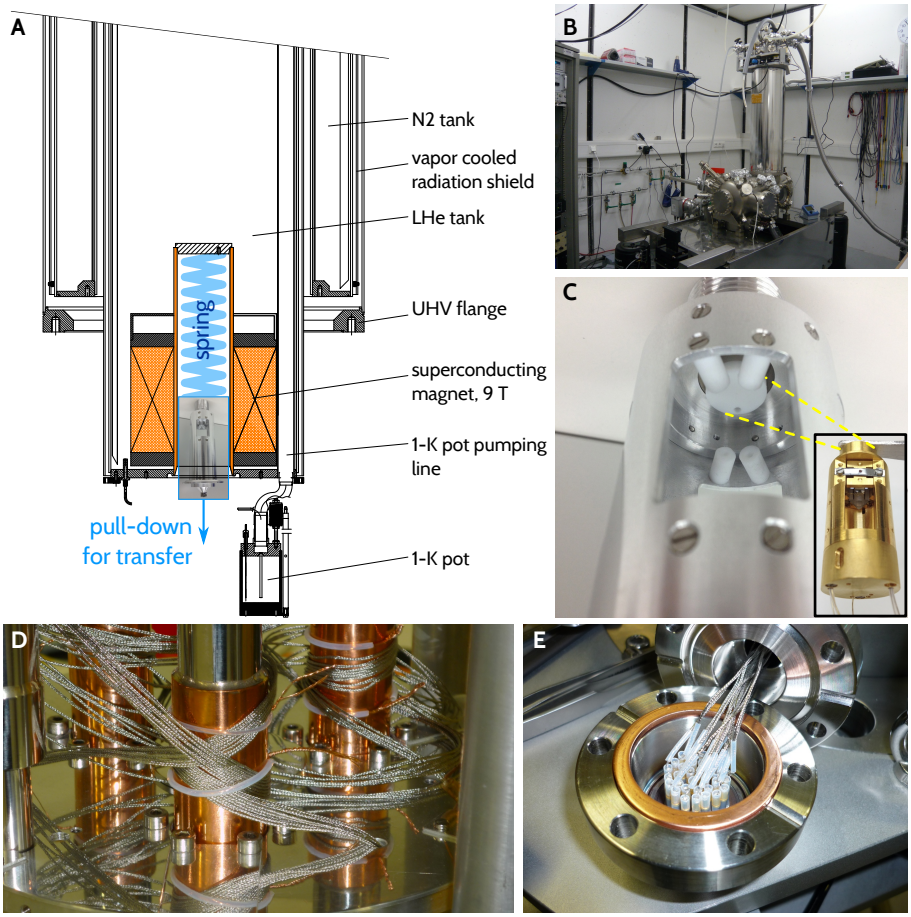

Figure 9.1.: Illustration of 1 K/9 T apparatus. **A** Schematic cross-section of bottom part of magnet cryostat. Not all details are shown. The frame and spring which are used for suspension of the STM head and sample-transfer are indicated as an overlay. **B** Photograph of laboratory. In this picture the manipulator is not assembled. **C** Photograph of frame which is to be mounted in the bore of the magnet. By using a strong spring it can be pulled-down for tip and sample transfer. The STM head, shown in the inset, will be attached to the circular Teflon piece. Dashed lines illustrate this connection. **D** The microscope wiring is fed into UHV via three multipin feedthroughs at the top of the cryostat (panel **E**). The wires are firmly pressed to baffles at different temperatures between room temperature and LHe temperature for thermal anchoring.

A pressure of $p = 1.5\,\mathrm{mbar}$ above the LHe bath in the 1-K pot corresponds to a temperature of 1.3 K. To obtain this pressure a pump with a pumping speed of

$$\dot{V} = \frac{\dot{n}RT}{p} \approx 30\,\frac{\mathrm{m}^3}{\mathrm{h}}, \tag{9.2}$$

is required, where $\dot{n} = 56\,\mathrm{ml/h} = 1.75\,\mathrm{mol/h}$ is the LHe consumption as per data sheet[3], R is the gas constant, and $T = 300\,\mathrm{K}$. Here, an XDS35*i* scroll pump from Edwards Vacuum (*120*) with a pumping speed of $36\,\mathrm{m}^3/\mathrm{h}$ is used. The cooling power of the 1-K pot equals the rate of evaporated liquid helium times its latent heat of evaporation $L = 83\,\mathrm{J/mol}$ (*58*), that is

$$P = \dot{n}L = 40\,\mathrm{mW}. \tag{9.3}$$

When operating the STM the head is located in the bore of the magnet (see figure 9.1A) with the tunneling junction at the point of highest magnetic field. For tip and sample transfer a strong spring is pulled down to grab them with a manipulator. The manipulator—except for its end piece—is similar to the ones used in the existing apparatuses.

As a matter of principle 1-K pots are source of mechanical vibrations[4]. For this reason, the magnet cryostat is designed in a way that the STM head is not mounted on the 1-K pot. Instead, the STM head is mechanically fixed to the 4 K helium stage (which itself is mechanically decoupled from the surroundings) of the cryostat. Only a thermal connection is established between the STM head and the 1-K pot.

For this purpose, very high purity copper wires[5] connect the STM head to the 1-K pot. As discussed in section 4.2, the thermal conductivity of metals is proportional to its purity in the relevant temperature range. Thus, a strong thermal coupling is achieved without a stiff mechanical

[3] The consumption is taken as constant, since it is determined by the dimensions of a small capillary between main bath and 1-K pot providing constant supply.

[4] When the helium from the main bath is thermalized before entering the 1-K pot, the helium is superfluid in the pot (*121*). This is done in our setup.

[5] Cu wires, purity ≥99.999 %, diameter of 0.1 mm, with a thermal conductivity $\kappa = 11\,300\,\mathrm{W/(m\,K)}$ (*58*).

coupling. On the other hand, a piece machined from PTFE (Teflon) realizes a weak thermal coupling[6] between STM head and main helium stage (see figure 9.1C).

The microscope wiring, illustrated in figure 9.1D and 9.1E, is fed into UHV via three multipin feedthroughs at the top of the cryostat. Teflon insulated twisted pair stainless steel cables with a braided shielding are used for all leads. Stainless steel minimizes the heat input into the system. Moreover, the cables are thermally anchored to baffles at the top of the cryostat. When thermodynamic equilibrium is reached, the baffles (not shown in figure 9.1A, cf. cryostat in figure 7.2A) are at descending temperatures from top to bottom.

To avoid ground loops each of the multipin feedthroughs is dedicated to a different scope of the microscope wiring:

1. Sensitive signal leads, i. e. leads for bias voltage and leads to handle (read out or pre-amplify) the tunneling current.

2. Piezo voltages, which can be up to $\pm 200\,\mathrm{V}$. For this reason, it makes sense to spatially separate the unshielded pins at the feedthroughs from sensitive signal leads.

3. Additional leads required, e. g. for temperature sensors.

All leads connecting the STM head are collected at likewise separated multipin connectors at the bottom of the cryostat (at the 4 K helium stage). Nonmagnetic phosphor bronze leads are used as cables between this point and the STM head to avoid stainless steel in the critical region.

9.2. Design Goals of STM Head

Prior to the actual design and construction of the STM head several goals were fixed:

[6] The thermal conductivity of PTFE at 4 K is only $\kappa = 46\,\mathrm{mW/(m\,K)}$ (*58*).

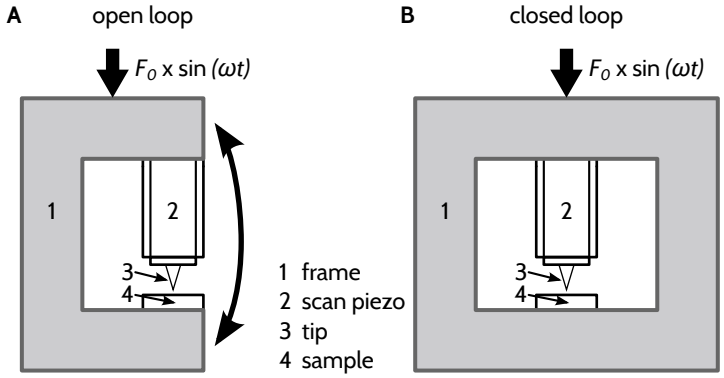

Figure 9.2.: Illustration of open (**A**) and closed (**B**) loop design of an STM head. A sinusoidal force models environmental vibrations. In the open loop design, this leads to a bending mode. Such a bending mode, being most probably the lowest eigenfrequency, has a high impact on the tip-sample distance z. In contrast, the closed loop design is much stiffer and less susceptible to the same sinusoidal force.

Modularity

In the course of construction there is always a chance that some components will not work as anticipated. Therefore, we set a high value on modularity. That is, the STM head was divided into independent functional units of vertical coarse approach, lateral coarse approach, tip-exchange mechanism, sample receptacle unit, and top cover for mounting. These units are indicated in figure 9.3A. Each of these parts may be changed easily when necessary or desirable to implement additional functionality.

Rigidity

Rigidity of an STM head is highly desirable for vibrational immunity. The tunneling current exponentially depends on the tip-sample distance. For this reason vibration isolation is essential for high-precision STM and STS measurements. Thus, the tip-sample junction has to be decoupled from external disturbances (*122*).

In general, the aim is to create a vibration filter having a large bandwidth using a system with a series of unmatched transfer functions (*123*).

The UHV chamber and the cryostat have low eigenfrequencies on the order of a few Hz. Hence, the STM head itself is designed to have eigenfrequencies in the kHz range.

One important aspect to achieve high rigidity is the closed-loop design (*124*). Closed-loop designs have in general much higher eigenfrequencies as compared to open-loop designs which were used in early STM heads. This concept is illustrated in figure 9.2. In general, for an open-loop design the lowest eigenfrequency corresponds to the bending mode. This bending mode limits the vertical resolution of an STM, and thus has to be avoided.

In summary, it is desired to manufacture a small STM head in a closed-loop design made of materials with a high rigidity.

Simplicity

In the spirit of the initial quotation we tried to keep things *as simple as possible*. This is best illustrated by the following examples.

- While the cryostat is equipped with radio-frequency cables, the initial sample holder design only involves a single electrical contact for the bias voltage.
- While lateral coarse movement is required for experiments on single molecules on islands of insulating films, it does not have to be reproducible at all costs.
- Including a tip-exchange mechanism obeys the second part of the initial quotation. The added complexity is necessary to enable spin-polarized STM with different macroscopic tips without breaking the vacuum.

9.3. Realization

The design of the final STM head is presented in figure 9.3. The main body is divided in four parts, which can be build up and changed independently from each other. All body parts are machined from phos-

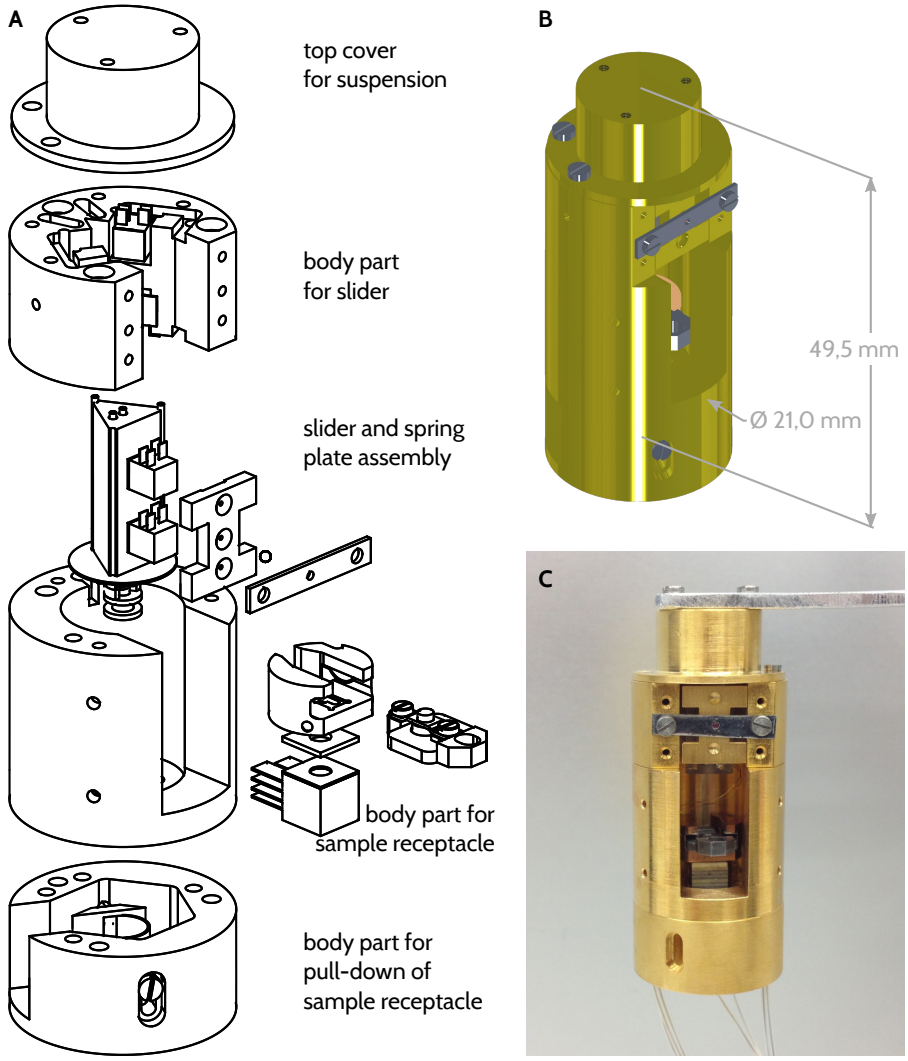

Figure 9.3.: Design of the STM head. **A** Exploded view depicting the main parts. The inner two body parts are intended for the vertical piezo motor with the tip and the lateral piezo motor with the sample. (For clarity, only four piezos of the vertical motor are drawn.) The further body parts are a top cover to mount the STM in the bore of the magnet, and a bottom part to adjust the contact pressure of the sample holder receptacle (see text). **B** indicates the overall dimensions of the STM head. **C** shows a photograph of the assembled and wired STM head.

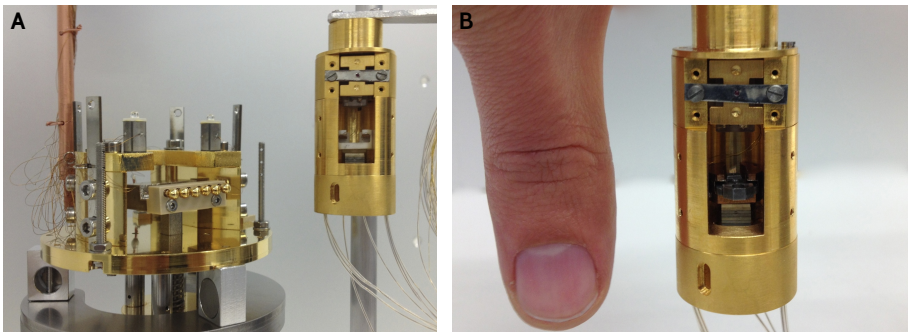

Figure 9.4.: Size of STM head in comparison to (**A**) a Besocke-style scan head in the Createc design (without ramp ring) and to (**B**) my own thumb.

phor bronze (CuSn5). This material can easily be machined and has a high thermal conductance. To avoid stainless steel in the high magnetic field region, custom-made screws made of molybdenum are used. Molybdenum has a high tensile strength. More important, in contrast to tantalum, its super conduction transition temperature is below the operation temperature. Figure 9.4 shows the size of the STM head in comparison to an existing Besocke scan head and an author's thumb. Some key components will be discussed in more detail in the following subsections.

9.3.1. Vertical Piezo Motor for Coarse Approach

The vertical coarse approach mechanism is the crucial part of an STM head. Many of the remaining components are relatively straightforward.

Pan-style coarse approach is well established and has proven its value. It is very reliable and reproducible. This is a big advantage when optical access is not possible during operation. Originally designed by S. H. Pan (*18*) it has been adopted by many groups in different systems (*19*, *20*, *23*, *125–127*), even down to the milli-kelvin regime (*21*).

In particular, it has been designed explicitly for application in high magnetic fields at temperatures around or below 1 K (*18*). The Pan design

Table 9.1.: Test of vertical piezo motor at ambient conditions using a sawtooth wave form.

Peak-to-peak amplitude	20 V
Frequency	12 kHz
Speed upward	0.12 mm/s
Speed downward	0.16 mm/s
Step size upward	10 nm
Step size downward	13.3 nm

is characterized by a sapphire prism pressed onto six shear piezos with alumina contact pads. Our realization is illustrated in figure 9.3 and figure 9.5.

Depending on the driving wave forms for each piezo the motion is called "sliding" or "walking". In the simplest case all piezos are actuated simultaneously using a periodic sawtooth wave form. Then, the resulting stick-slip motion is referred to as sliding. In contrast, when the piezos are actuated one after the other, the motion is called walking[7]. The walking technique requires individual leads for each piezo, and a more sophisticated driving electronic. Tests in ambient conditions have shown that the piezo motor presented here works very reliable using the sliding technique. Driving parameters are summarized in table 9.1. The difference between up- and downward speed is comparable to the best settings reported for a similar STM head (*21*). The ratio of step size and amplitude of driving voltage is also comparable.

9.3.2. Tip-Exchange Mechanism

The tip exchange mechanism, illustrated in figure 9.5A, was inspired by reference (*125*). Here, a vertical leaf spring has been replaced by a circular spring to minimize its height. The tip is fixed in a tip holder made of molybdenum. The tip holder is pressed by the circular spring

[7] This technique was proposed in the original publication by Pan, Hudson, and Davis (*18*).

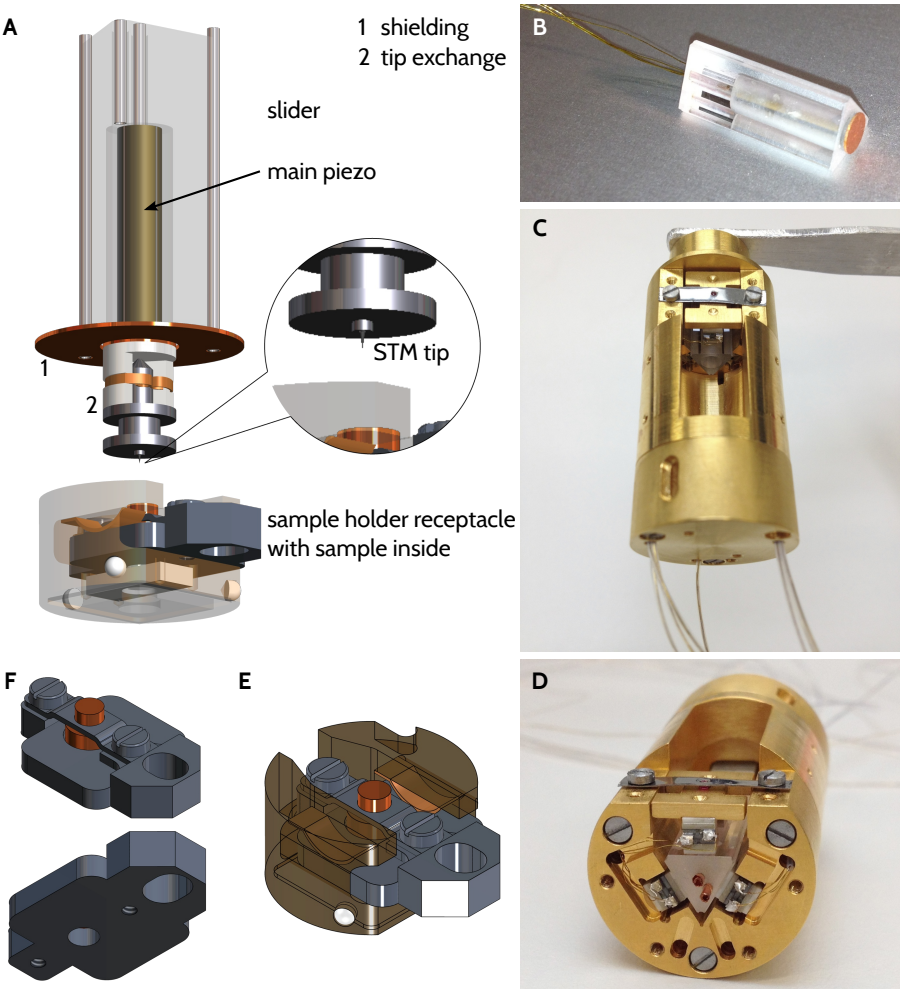

Figure 9.5.: Details of slider and sample holder. **A** Rendering of slider and sample holder assembly. The main piezo is mounted to a hole in the prism. Two shielding plates on the prism and the tube piezo reduce the electric field at the sample caused by the piezo voltages. The sample holder receptacle made of phosphor bronze is rendered translucent for clarity. **B** Photograph of the slider prism and the wired scan piezo. On the piezo the shielding is already assembled. **C** Photograph of the assembled STM head. All wires are routed in holes of the body to the downside. **D** shows how the slider is jammed in between of the shear piezos. It can be seen that the molybdenum leaf spring is under tension. **E** Rendering of sample holder assembly. **F** Perspective views on sample holder top and bottom.

into the v-groove of the tip-holder receptacle machined from a piece of sapphire or Macor. The circular spring also acts as electrical contact for the tunneling current. A transporter at the manipulator carries the tip holder using its notch to insert the tip holder into the scanner.

9.3.3. Sample Holder

The sample holder assembly is depicted in figure 9.5E-F. The sample holder base plate is machined from a single piece of molybdenum. Two M1 threads are used to fix the single crystal by means of a molybdenum leaf spring. Single crystal samples need to be annealed during sample preparation. The sample holders are intended for heating by electron bombardment. To optimize the efficiency a hole in the sample holder base plate enables direct heating of the single crystal as compared to indirect heating via the base plate.

If future experiments require samples with more than one electrical contact the sample holder base plate may be machined from heat-resistant sapphire. In this case the sample holder receptacle can also easily be adjusted. It may be manufactured from an insulating material like PEEK, Macor, or sapphire with several electrical connections.

9.3.4. Lateral Piezo Motor for Coarse Approach

The sample holder receptacle is pressed by an adjustable spring onto a piezo stack, which can be deflected in both lateral directions (x, y). A macroscopic movement of the whole sample receptacle with respect to a piezo stack can be realized by driving the piezo in a stick-slip fashion similar to the vertical motor. This motor is needed to approach different spots on the sample surface. In contrast to the vertical coarse approach the reproducibility in this case is not essential.

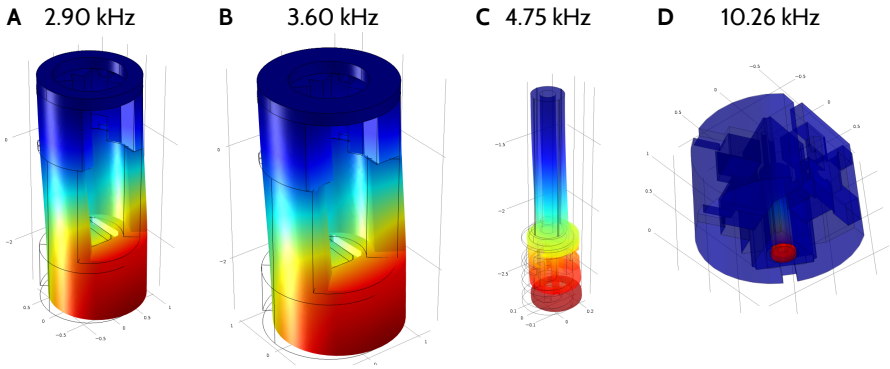

Figure 9.6.: Results of finite element analysis. Deformation in the respective mode is shown. In addition, the surface color corresponds to the magnitude of displacement (arbitrary units). **A** Initially, a thinner wall was used for the body parts resulting in a lowest eigenfrequency of 2.90 kHz. **B** This eigenmode can be increased to 3.60 kHz using a greater wall thickness. **C** The lowest mode of the scan piezo and tip assembly corresponds to 4.75 kHz, which is significantly lower than the eigenfrequency of the scan piezo itself (cf. panel **D**). **D** When calculating the vertical piezo motor without tip, its lowest eigenfrequency corresponds to bending of the scan piezo at 10.26 kHz.

9.3.5. Finite Element Analysis

In the course of the design work, key components of the STM head were analyzed by means of finite element analysis (FEA). The structural mechanics module of COMSOL Multiphysics was used to compute the lowest eigenfrequencies and eigenmodes of different parts. The upper end of each assembly was rigidly fixed, as it is the case in the experimental setup.

The results are shown in figure 9.6. The initial design of the body is shown in panel A. Increasing the wall thickness resulted in a shift of the fundamental eigenfrequency from 2.90 kHz to 3.60 kHz. As can be seen from figure 9.6D, the eigenfrequency of the main piezo tube is higher than 10 kHz. Figure 9.6C shows that the tip holder assembly leads to a shift of the corresponding mode to 4.75 kHz. All modes correspond to bending of the respective parts. In literature, higher eigenfrequencies in a similar STM head have only been reported using a unibody design

manufactured from sapphire (*127*).

Finally, it has to be emphasized that room-temperature data was used for the material properties. It is therefore safe to assume that at low temperatures the eigenfrequencies of all parts will shift to higher frequencies.

9.4. Conclusions

In this chapter I have presented the design and build-up of a scanning tunneling microscope head for operation in high magnetic fields. A rigid and compact STM head has been developed and built-up. The STM head provides a simple tip-exchange mechanism to facilitate spin-polarized STM measurements.

While the magnet cryostat has been wired, and all linking parts have been designed, the integration of the STM head into the apparatus has not been performed yet. However, initial tests of the vertical piezo motor and finite element modeling show promise for future experiments.

Other possible applications include giant magnetoresistance (GMR) studies on single molecules. While it has been shown that it is possible to prove this effect without applied magnetic field (*128*), an external field is beneficial. Such prospective experiments might provide insight into the fundamentals of single spin data storage.

10. Atomic Force Microscopy Reveals Bistable Configurations of Dibenzo[a,h]thianthrene and their Interconversion Pathway

Most of the work presented in this chapter has been published in Physical Review Letters[1] *(129). Parts of the text are identical to the publication.*

This chapter presents combined STM and AFM experiments on DBTH molecules. Recently, the chemical structure of planar pentacene molecule has been visualized by means of noncontact atomic force microscopy (AFM) (*26*). Here, we apply this method to nonplanar DBTH molecules. In conjunction with the capability of scanning tunneling microscopy (STM) to perform orbital imaging on ultrathin insulating films (*10*), it is possible to gain independent and complementary information of the molecular as well as of the adsorption geometry, but also of the electronic structure of individual molecules.

We observe that two stable configurations exist corresponding to different isomers of free nonplanar molecules. Excitations from inelastic electron tunneling allow reversible switching between both configurations. The chirality of the molecules could be utilized to determine their interconversion pathway in detail. Finally, our investigations also shed new light on contrast mechanisms in scanning tunneling microscopy.

[1] N. Pavliček *et al.*, *Atomic Force Microscopy Reveals Bistable Configurations of Dibenzo[a,h]thianthrene and their Interconversion Pathway.* Physical Review Letters **108**, 086101 (2012).

10.1. Introduction

Unambiguous identification of configurational changes of adsorbed molecules is a challenging task by means of STM alone (*130*) probing the local density of states rather than geometry. Usually, additional techniques such as near-edge x-ray adsorption fine structure measurements have to be employed (*131*, *132*).

The AFM measurements were carried out in the homebuilt combined STM and AFM presented in section 7.1. Some of the STM measurements (figure 10.3 and figure 10.4) were performed in the STM without AFM capability, which has likewise been presented in section 7.1.

All experiments were carried out on a double layer of sodium chloride on Cu(111) single crystals. This substrate system is denoted as NaCl(2ML)/Cu(111). The DBTH molecules were synthesized as described previously (*133*).

Low coverages of CO (for tip functionalization) and DBTH molecules were adsorbed at sample temperatures below 10 K. As discussed in detail in section 7.2.2, the tip had been terminated with a CO molecule for all AFM measurements to enhance the resolution considerably (*26*).

10.2. DBTH and Related Molecules

DBTH molecules are within the family of thianthrenes, in which, due to the presence of the lone pairs of the thioether groups, the molecules are folded along the S-S axis (*111–116*). As described in section 8.2, we have performed density functional theory calculations (*99*, *100*) for a free molecule (i. e., without substrate) using the highly optimized `CPMD` code (*103*) to obtain the folding angle for DBTH and related molecules.

The resulting structures are illustrated in figure 10.1. To define the dihedral angles Θ, given in table 8.1, the atoms labeled with a red dot are used. When going from TH to DBTH the folding angle slightly

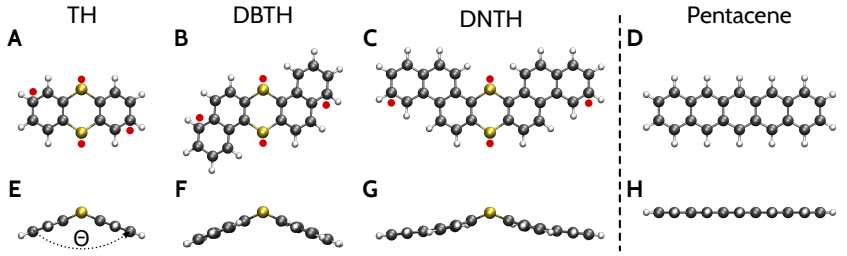

Figure 10.1.: Molecular geometry of thianthrene derivatives from DFT calculations. **A**-**D** Top views of TH, DBTH, DNTH, and pentacene molecules, respectively. **E**-**H** Corresponding side views. White, gray, and yellow balls represent H, C, and S atoms. Red dots indicate the atoms used to define the angles Θ, which is indicated for TH in panel **E**. One of the outermost C atoms and the two S atoms define a plane and the angle Θ between this plane and the second C atom is measured.

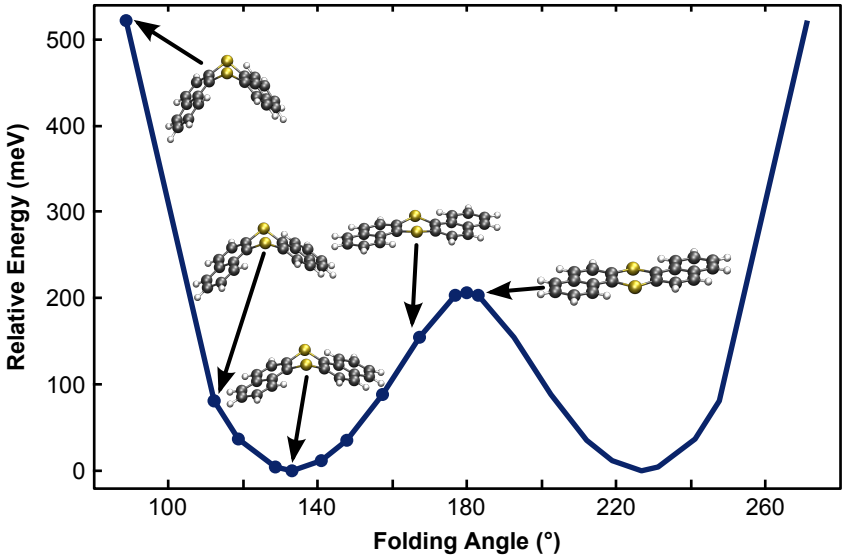

Figure 10.2.: Relative energy of DBTH molecules as a function of dihedral angle Θ. The total energy for the optimized geometry is set as zero. The circles correspond to calculated energies in the illustrated geometries. The curve has been mirrored with respect to a folding angle Θ of 180°.

decreases. When further increasing the molecular size the folding angle drastically increases. Interestingly, the bond angle for the S atoms remains roughly unchanged for all three structures. The flattening of the larger DNTH molecule is instead accomplished by a bending of the molecular structure over the length of two C-C bonds.

In the optimized geometry, we find a dihedral angle (see figure 10.1 for definition) of $\Theta = 134°$. Initially, we compared this value to the one observed for thianthrene by x-ray crystallography with $\Theta = 128°$ (*112*). We attributed the difference to the extension of the π conjugation in DBTH molecules and thus flattening the molecule. However, from the DFT calculations it can be seen that for a free TH molecule the value is roughly the same. This finding suggests that incorporation in a crystal and associated molecule-molecule interactions lead to a slightly different value.

Figure 10.2 shows that the energy barrier for flapping is approximately 200 meV. As expected, the relative energy diverges for very small Θ, and is the same for 183° and 177°.

10.3. Bistable Switch of DBTH Molecules

Bias dependent STM images of DBTH on NaCl(2ML)/Cu(111) are presented in figure 10.3. Two species of DBTH molecules that are nonequivalent with respect to translation, mirroring and/or rotations exist on the surface, which we denote as **U** and **D** as indicated in the caption of figure 10.3. STM images at low bias voltages (figures 10.3A and 10.3B) as well as orbital images (figures 10.3C and 10.3D) show distinct differences between both species. However, we note that the nodal plane structure of the orbital images is the same. In addition, STS spectra acquired on both species are similar, and the only peak in the accessible voltage range at around 2.45 V corresponds to the negative ion resonance.

By means of the manipulation technique based on inelastic excitations, which has been introduced in section 5.3, it is possible to induce the lateral motion of individual molecules, as well as to switch between the

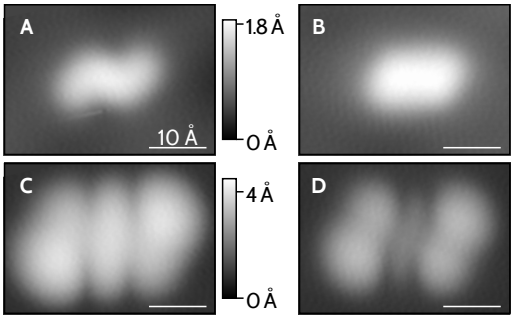

Figure 10.3.: Bias dependent STM imaging reveals two possible nonequivalent species of the same individual DBTH molecule on NaCl(2ML)/Cu(111). **A** and **B** Constant-current images of **U** and **D** configuration, respectively, at low bias voltage (imaging parameters: $I = 0.4\,\mathrm{pA}$, $V = 0.01\,\mathrm{V}$). **C** and **D** Images corresponding to the lowest unoccupied molecular orbital acquired with the same metal tip apex ($I = 0.2\,\mathrm{pA}$, $V = 2.3\,\mathrm{V}$).

two species. The results are presented in figure 10.4[2]. An analysis of many excitations reveals that whenever a molecule switches from **U** to **D** or vice versa, both the in-surface-plane orientation and the adsorption site change (see below for a detailed adsorption geometry determination). Thus, every species can be assigned to a different adsorption site.

Figures 10.4E and 10.4F present STM images at low bias voltages. The difference of these images, shown in figure 10.4G, demonstrates that neither species has an influence on the scattering wave pattern of the substrate's interface state. Hence, it can be inferred that both species are neutral (*89*, *90*)[3]. The similarity in the electronic structure (nodal planes in orbital imaging and the energy of the negative ion resonance) suggests that the molecule is either in the same or an equivalent configuration, that is, it has a similar dihedral angle. The different appearance

[2]STM and AFM data before and after an excitation show that molecules and NaCl remain undamaged.

[3]The long-ranged Coulomb potential of a charged molecule would lead to concentric ring-like standing waves due to scattering of the interface state (see section 7.2.1) electrons (*89*, *90*). Since the adsorption site changes, even permanent charging with the same number of electrons could be detected in the difference image.

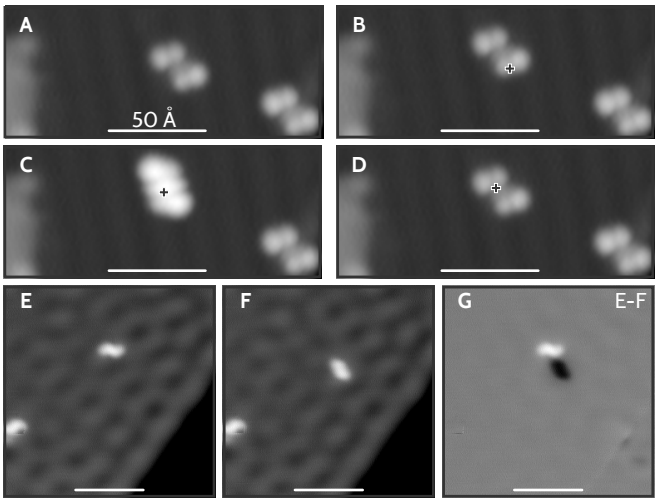

Figure 10.4.: Switching between molecular configurations by means of inelastic excitations. A manipulation sequence shows subsequent STM orbital images ($I = 0.2\,\mathrm{pA}$, $V = 2.35\,\mathrm{V}$). Crosses indicate previous positions of the center of the molecule. From **A** to **B** only the adsorption position changes. In contrast, both position and in-plane orientation change from **B** to **C** and subsequently to **D**. STM images in **E** and **F** show same molecule before and after switching between both configurations ($I = 0.4\,\mathrm{pA}$, $V = 0.01\,\mathrm{V}$). **F** Difference image constructed by subtracting image **F** from image **E**.

could be simply due to different adsorption sites leading to slightly different electronic properties. It must be emphasized that we can not draw any conclusions from the STM data going beyond what has been discussed until this point.

10.4. Revealing the Molecular Structure of Both Configurations

As a next step, we performed constant height Δf imaging presented in figure 10.5A in the AFM mode. It is immediately apparent that the two species correspond to different molecular configurations (*134*). First, consider the S-S axis. Whereas **U** molecules show a characteristic bright stripe, **D** molecules do not show any atomic contrast at the center at

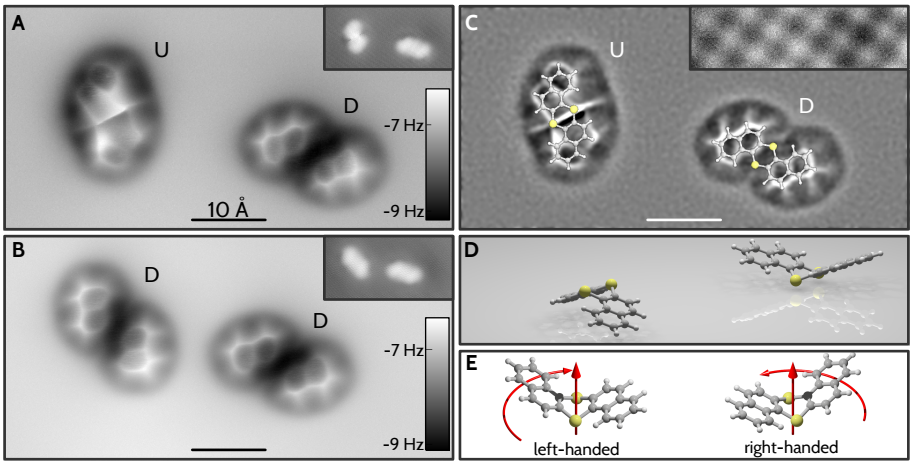

Figure 10.5.: AFM measurements on DBTH on NaCl(2ML)/Cu(111) with a CO-functionalized tip. **A** Constant height AFM image. Imaging parameters: oscillation amplitude $A = 0.5\,\text{Å}$, $V = 0\,\text{V}$, $\Delta z = 0.0\,\text{Å}$. Δz corresponds to a distance decrease with respect to an STM set-point of $I = 0.5\,\text{pA}$, $V = 0.4\,\text{V}$ above the clean NaCl(2ML)/Cu(111). **B** Image of the same area as in **A** after both molecules changed their adsorption position ($A = 0.5\,\text{Å}$, $V = 0\,\text{V}$, $\Delta z = 0.1\,\text{Å}$). Insets in **A** and **B** show constant-current STM images of the same frame. Panel **C** represents the curvature of the image in **A** obtained by calculating the Laplacian. Molecular models (drawn to scale) for **U** and **D** are overlaid as a guide to the eye; the slightly larger appearance of molecules has been discussed previously (*75*). Inset shows atomically resolved NaCl lattice. **D** Model representing molecules in **U** and **D** configuration on a surface. **E** Model depicting chiral enantiomers of the free molecule.

the same tip height. In addition, the carbon rings of **U** molecules show an apparent distortion.

Before we shed light on the actual structure of both configurations, we have to discuss the origin of the contrast in the frequency shift. For the small amplitudes used here, the frequency shift well approximates the force gradient. While attractive long-range forces are responsible for overall negative Δf background, repulsive short-range contributions due to Pauli repulsion are decisive for the intramolecular contrast as was shown in (*26*, *75*). These short-range forces are very sensitive to the tip-molecule distance. An examination of C atoms and

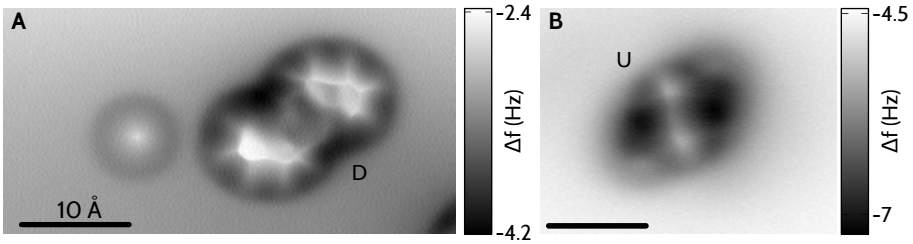

Figure 10.6.: Distance dependence of constant height AFM imaging. **A** Image of **D** molecule at closer tip-molecule distance as compared to figure 10.5. The molecule is adsorbed close to a CO molecule. At this distance the S atoms are also visible for **D** molecules. Imaging parameters: oscillation amplitude $A = 0.6\,\text{Å}$, $V = 0\,\text{V}$, $\Delta z = -0.4\,\text{Å}$. Δz corresponds to a distance decrease with respect to an STM set point of $I = 1.5\,\text{pA}$, $V = 0.3\,\text{V}$ above the clean NaCl(2ML)/Cu(111). **B** When imaging **U** molecules at larger tip-molecule distances, no apparent distortions due to bending of the CO molecule at the tip apex are visible ($A = 0.5\,\text{Å}$, $V = 0\,\text{V}$, $\Delta z = -0.3\,\text{Å}$ relating to $I = 0.5\,\text{pA}$, $V = 0.4\,\text{V}$).

C-C bonds shows a specific gradient for both species. In the **D** (**U**) configuration the contrast increases (decreases) with the distance to the S-S axis. As discussed above, in this regime we can attribute a higher contrast with stronger repulsive contributions, and consequently a smaller distance to the molecule. Thus, the bright band along the S-S axis in the **U** configuration can be attributed to a small distance to the tip. We believe that the sharp feature is a fingerprint of the CO molecule at the tip apex which bends due to the protruding S atoms (*75*). Accordingly, in this configuration the S atoms are pointing upward, and the aromatic rings are close to the surface. In contrast, the S atoms of **D** molecules are closest to the surface, whereas its naphthalene units are pointing upwards. Both configurations are illustrated in figure 10.5D.

The S atoms can also be imaged for **D** molecules when using an STM set point over the bare NaCl surface corresponding to a slightly smaller tip-sample distance as compared to figure 10.5. Such an AFM image is presented in figure 10.6A. In this case, the outer rings appear very bright corresponding to a small distance to the tip. It can be seen that there is significant repulsive force also for the regions inside the carbon

rings. This points out that the CO molecule at the tip apex is strongly bent when imaging these regions. In agreement to this interpretation, a considerable signal in the excitation channel is observed for even smaller tip-sample distances (not presented here).

These results are consistent with AFM images of **U** molecules, presented in figure 10.6B, at larger tip-sample distances as compared to figure 10.5. In this case, the interaction of the CO molecule at the tip apex with the protruding S atoms is lower. Accordingly, the S atoms are imaged without apparent distortions and no sharp features are observed.

10.5. Determination of the Interconversion Pathway

The stereochemistry of DBTH molecules can be utilized to determine the pathway of the configurational change (*135*, *136*). We have estimated the barrier for flapping to be about 200 meV from our density functional calculations using the relative energy versus folding angle Θ (see section 8.2 and discussion of figure 10.2). As the flapping of molecules is frozen at the temperatures of our experiments, there are two enantiomers of the free molecule possessing C_2 symmetry, as depicted in figure 10.5E[4].

In general, going from upward to downward pointing S atoms can be realized either by flipping from one face to the other, or by flapping the naphthalene units with respect to the S atoms. The molecular structure projected onto the surface plane would change for flipping, but not for flapping. As can be seen from the left molecule in Figs. 10.5A and 10.5B, the latter is the case. From this it follows immediately that switching is caused by a change of the folding angle, and the initial and final configurations correspond to the different chiral enantiomers of the free molecule as depicted in figure 10.5E.

[4]In total, 4 configurational isomers exist on the surface: one pair of enantiomers for molecules in each configuration (**U** and **D**).

10.6. Force versus Distance Curves

In all AFM images presented here the C and S atoms appear distinctly different. It is interesting to ask wether these differences stem from their chemical nature or if this is purely due to molecular geometry. To this end we recorded frequency shift versus distance curves, which are presented in figure 10.7A. All curves were recorded in a constant distance to the underlying NaCl surface. To concentrate on the short-range contributions a curve above the bare NaCl surface has been subtracted.

It is clear that the curves acquired above the two C sites are qualitatively similar, while the curve over the S atom is significantly different. This hints to a chemical sensitivity rather than a purely geometric effect (*137*). The tip-sample force can be extracted from the frequency shift versus distance curves using the method of Sader and Jarvis (*138*)[5]. The resulting force curves are given in figure 10.7B. For the C sites, the slope of the force curves decreases for small tip-sample distances, suggesting that it is close to the force minimum. In contrast, for the S site the slope is approximately constant and its absolute value is significantly higher.

10.7. Adsorption Site Determination

To get more insight into the stabilization mechanism of both species, we determined the adsorption site of molecules in both states. Therefore, we used AFM imaging with STM constant-current feedback. That is, the frequency shift Δf is recorded simultaneously with the STM topography while the STM feedback is used to control the tip height[6]. Figures 10.8C-10.8F show the frequency shift Δf of such measurements for both configurations. Recently, it has been shown that the faint maxima

[5] For this analysis, a Matlab script provided by Welker, Illek, and Giessibl (*139*) has been slightly modified.

[6] STM and AFM signals are convoluted in this mode (*140*). However, this mode enables atomic resolution on NaCl and stable imaging of the molecules at the same time (*27*).

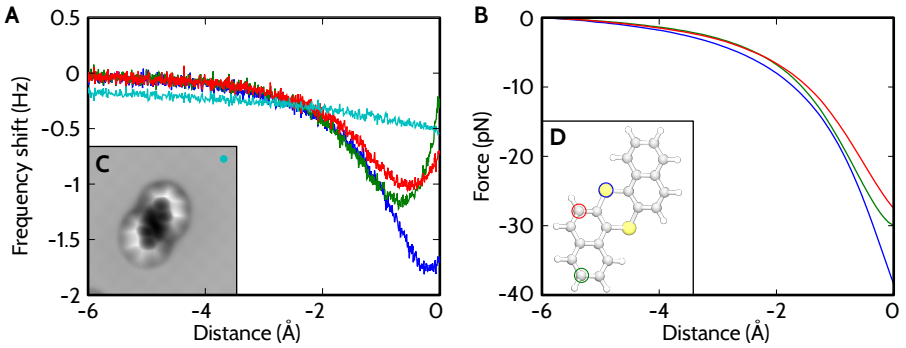

Figure 10.7.: Force spectroscopy on a **D** molecule. **A** Frequency shift vs. distance curves. All curves have been corrected for the long-range van der Waals part by subtracting the light blue curve taken on NaCl. The tip has been positioned over the atoms indicated in panel **D**. Oscillation amplitude $A = 0.45\,\text{Å}$, $V = 0\,\text{V}$. The point of closest approach corresponds to an STM set-point of $I = 1.0\,\text{pA}$, $V = 0.3\,\text{V}$ above the clean NaCl(2ML)/Cu(111). **B** Force vs. distance curve, calculated by the method of Jader and Sarvis (see text). **C** Frequency shift image in constant current mode taken before starting spectroscopy mode.

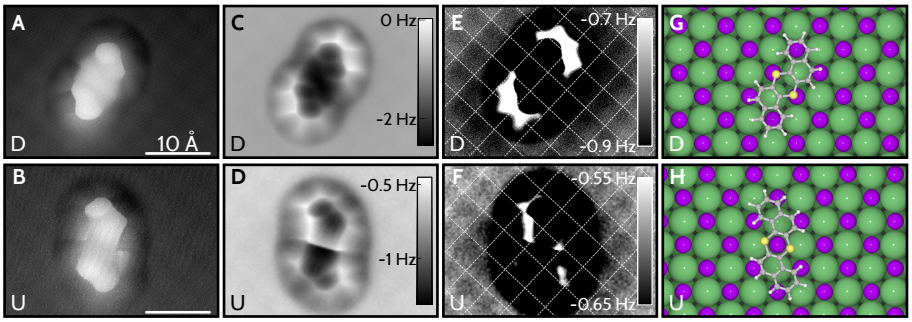

Figure 10.8.: Determination of the molecular adsorption position for down (top row) and up (bottom) geometry using AFM with STM feedback. **A** and **B** Constant current STM images (imaging parameters $I = 1.0\,\text{pA}$, $V = 0.3\,\text{V}$). The corresponding frequency shift Δf recorded simultaneously is shown in panels **C** and **D** (oscillation amplitude $A = 0.5\,\text{Å}$, and $A = 1.0\,\text{Å}$, respectively). Panel **E** and **F** show the same data with a different Δf scale to highlight the faint maxima resembling Cl sites, for which a lattice was overlaid as a guide to the eye. Panels **G** and **H** show models of the adsorption position as determined from the experimental data. Big green and small purple balls represent Cl^- and Na^+ ions, respectively.

correspond to the Cl sites of the NaCl(100) lattice (*27*). From the models of the adsorption geometries shown in figures 10.8G and 10.8H we can conclude that the S atoms are located on top of Na sites for **D** molecules. This can be rationalized by the ionic nature of the NaCl lattice as follows: The downward pointing lone pairs of S atoms are attracted by Na^+ ions and repelled by Cl^- ions. In contrast, the S atoms of **U** molecules are farthest from the surface, and the naphthalene units align with a polar direction of NaCl. This results in a geometry in which the center of the molecule is located above a Na site[7].

Since we are by now in a position, in which we have a detailed picture of our system, we would like to revisit figure 10.3 particularly with regard to the actual molecular structure. Resonance images resembling the orbital structure can not be used to make a statement about the geometry. In contrast, images at low voltages can be argued to be due to modifications of the tunneling barrier and should therefore be somewhat related to geometry. However, these images show a pronounced *s* shape for **U** and a relatively straight rod for **D** molecules, whereas the apparent height above their center is the same. Thus, they neither reflect the lateral geometry nor the vertical changes in the structure.

10.8. Conclusions

In conclusion, we have revealed the exact geometries of two different configurations of DBTH molecules on NaCl(2ML)/Cu(111) using combined STM and AFM experiments. Our experiments demonstrate reproducible and nondestructive switching between both configurations. We have shown that AFM with submolecular resolution is capable of directly revealing configurational changes in real space. Our data visualize displacements perpendicular to the surface in a nonplanar molecule. Taking the chirality of DBTH molecules into account, we could unambiguously determine the interconversion pathway.

[7] All possible, independently determined adsorption geometries are consistent with symmetry considerations. We estimate the error bars to be $\pm 0.5\,\text{Å}$ for the site determination and $\pm 3^\circ$ for the in-plane orientation.

Stabilization of both adsorption geometries can be rationalized by the (electrostatic) interaction with the sodium chloride substrate. Therefore, a next step would be to investigate wether the results presented here can be generalized for related molecules like for example DNTH. Besides, it would be of great interest to find a tip-termination suitable for operation of the molecular switch by means of the tip-sample force. This would allow direct determination of the energy barrier involved in switching.

11. Symmetry-Dependence of Vibration-Assisted Tunneling

Most of the work presented in this chapter has been published in Physical Review Letters[1] *(*141*). Parts of the text are identical to the publication.*

In organic and molecular electronics the electrons are much more spatially confined as compared to inorganic semiconductors, leading to a much stronger electron-vibron (*e*-ν) coupling (*142–144*). Therefore, *e*-ν coupling gives rise to substantial dissipation in such systems, which should be minimized in electronic devices.

When an electron tunnels into a given molecule (electron attachment), the nuclei will relax giving rise to the so-called reorganization energy, a process that is usually treated in the Franck-Condon picture (*142*). In the latter, the *e*-ν coupling strength for all modes is inferred from projecting the atomic displacements that arise upon electron attachment onto the vibrational eigenmodes (*104*, *142*). Whereas the wave functions of the vibrational states are crucial in the Franck-Condon picture, it does not account for the electronic wave functions. In contrast to that picture, this chapter shows that the spatial position of the electron injection as well as the local wave function symmetry dramatically affect the *e*-ν coupling.

11.1. Introduction

As discussed in chapter 5, we use ultrathin insulating films on copper single crystals as substrates in our LT STM setup. This setup consti-

[1] N. Pavliček *et al.*, *Symmetry-Dependence of Vibration-Assisted Tunneling.* Physical Review Letters **110**, 136101 (2013).

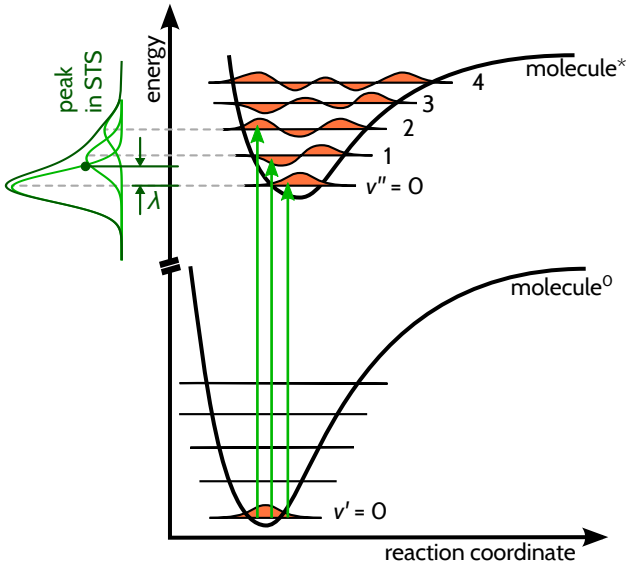

Figure 11.1.: Franck-Condon picture for vibronic transitions. Electronic transitions are represented by vertical arrows, since they are much faster than molecular relaxations. That is, the reaction coordinate is constant for any electronic transition leading to a series of vibronic peaks. Each vibronic peak appears broadened in STS (see figure 11.2 and discussion in text) resulting in a peak structure as illustrated on the left-hand side. The reorganization energy λ (see text) is indicated as the energy difference between the elastic peak and the centroid (green dot) of the peak in STS. Since the experiments discussed here are performed at low temperatures, all transitions start in the vibrational ground state of the initial electronic state.

tutes a DBTJ geometry and enables spatially resolved vibronic spectroscopy (*145*, *146*). It is important to emphasize that this regime is highly relevant, resembling electron-hopping in organic and molecular electronics. In particular, it is very different from usual STM-based inelastic electron tunneling spectroscopy (IETS) setups (*17*)[2], for which it has been realized that the symmetries of wave functions play an important role (*147–150*).

As a model system we chose pentacene, which is widely used in or-

[2]This corresponds to IETS close to the Fermi level, and does not involve simultaneous electronic transitions.

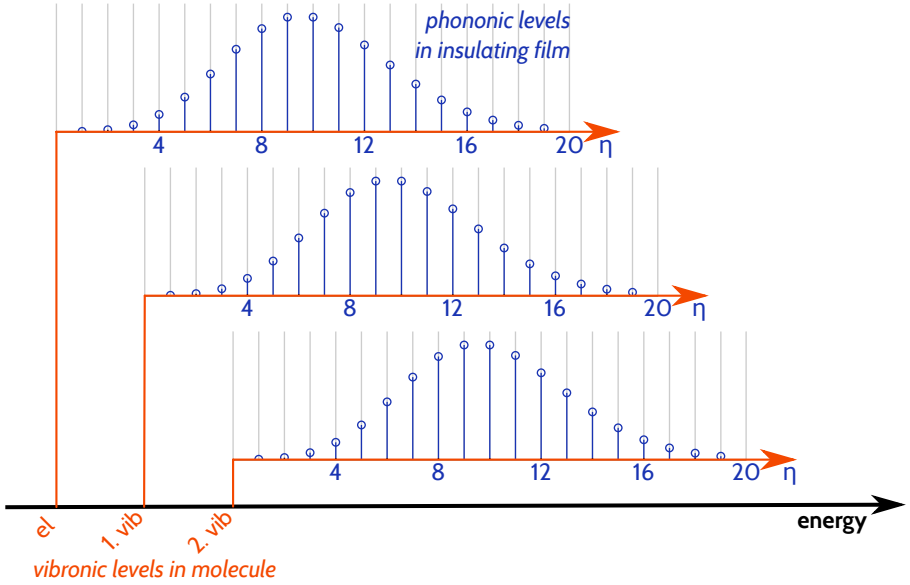

Figure 11.2.: Schematic illustration of vibronic progression on insulating films. The individual vibronic levels due to *e*-ν coupling in the molecule are shown in orange on the energy axes. Each level is independently broadened due to *e*-*ph* coupling in the insulating film as depicted in blue. The phononic levels are closely spaced. Therefore, in STS only the envelope of the Poisson distribution can be resolved, which approximately corresponds to a Gaussian for large Huang-Rhys factors S.

ganic electronics and one of the best studied systems (*104–107*, *151*). We consider only transport involving the first molecular resonances, attributed to occupation and depletion of the LUMO and HOMO level, respectively. Effectively, this renders a single-level system. If several molecular orbitals are closely spaced in energy, tunneling into different orbitals and mixing of vibronic states (*145*, *152*, *153*) may lead to spatial variations of the *e*-ν coupling, which can be ruled out here. In our system, transport involving further orbitals (LUMO+1, HOMO-1) can be excluded due to energy differences of more than 1 eV to subsequent orbitals (*106*, *154*).

In contrast to the work presented in the previous chapter, the energy

resolution is decisive for the experiments presented here. The energy resolution varies significantly for different ultrathin insulating films and increases from NaCl to RbI to Xe. The reason for the different energy resolution is electron-phonon (*e-ph*) coupling in the insulating film (see section 5.2 for a discussion of the origin and section 7.2.1 for data on the different insulating films) (*69*). However, the better the energy resolution is the weaker the molecules are bound to the surface. In particular, ionic contributions to the molecule-substrate interaction are missing on Xe in contrast to RbI and NaCl. Taking many spectra on an individual molecule on Xe inevitably leads to a lateral displacement of the molecule after some time due to inelastic excitations[3].

In addition, the different work functions of the combined insulator-substrate systems give rise to an overall shift of molecular resonances from one system to the next (*10*). Thus, the HOMO is hardly accessible on RbI. Finally, functionalizing the tip with CO molecules required working on NaCl films for technical reasons (see section 7.2.2). Therefore, depending on the experimental requirements, one monolayer thick Xe, two monolayer thick RbI or two monolayer thick NaCl islands (see section 7.2) were chosen as insulating films for the work presented in this chapter. CO (for tip functionalization) and pentacene molecules were adsorbed at sample temperatures below 10 K. The coverage was chosen to be far below one monolayer.

The substrate-induced *e-ph* broadening of spectroscopic features discussed above should occur independent of the *e-ν* coupling to vibrational modes inside the molecule, which is addressed here. Therefore, each vibronic transition gives rise to a broadened peak in STS. Both processes, *e-ph* and *e-ν* coupling can be understood in a Franck-Condon picture as depicted in figure 11.1. That is, consecutive vibronic levels show up as distinct peaks for rather weak broadening. Such a peak pattern—called **vibronic progression**—is depicted in figure 11.2. In contrast, in the case of strong broadening only the envelope of the vibronic progression is measured[4].

[3] Here, the same mechanism that can be employed to deliberately move adsorbates on insulating films (as discussed in section 5.3) or to operate the molecular switch in the previous chapter is an unwanted side-effect.

[4] Technically speaking, such a vibronic progression may exist for each vibrational

To keep changes of the Stark shift to a minimum, we acquired all spectral series in constant height mode, that is, all spectra at different spatial positions for a given system are acquired with the same vertical distance from the insulating film[5].

11.2. Scanning Tunneling Spectroscopy on Different Insulating Films

Figure 11.3A presents differential conductance (dI/dV) spectra of the LUMO-related peak above the end and the center of a single pentacene molecule adsorbed on a monolayer of Xe[6]. We emphasize that the entire peak structure has to correspond to the same electronic resonance, with varying contributions of vibrational excitations, since the LUMO+1 state is too high in energy to contribute (*106*, *154*). By comparing spectra taken at different positions, it is clear that the centroid[7] of the peak is found at higher energy at the center of the molecule than at the end, see figure 11.3D.

Within the entire peak structure the local maximum that is lowest in energy can be assigned to the elastic tunneling contribution (*104*). For pentacene on Xe films, where the energy resolution is best, this can be attributed to $V \approx 2.18\,\mathrm{V}$. When comparing the spatially resolved vibronic spectra, one realizes that at the center of the molecule this elastic contribution is strongly suppressed. The variations of the centroid can be linked to the reorganization energy λ, which can be written as (*157*)

$$\lambda = \sum \lambda_i = \sum \hbar\omega_i S_i, \tag{11.1}$$

mode of a molecule. However, as will become clear in the course of this chapter, we cannot assign a single vibrational eigenmode being responsible for the experimental peak structure.

[5] Since the internal shape of the peak structure changes drastically, these changes cannot be attributed to the Stark shift (*69*, *155*, *156*).

[6] dI/dV curves were obtained by numerical derivation of $I(V)$ curves.

[7] Centroids of dI/dV curves refer to the center of mass of the area under the curve.

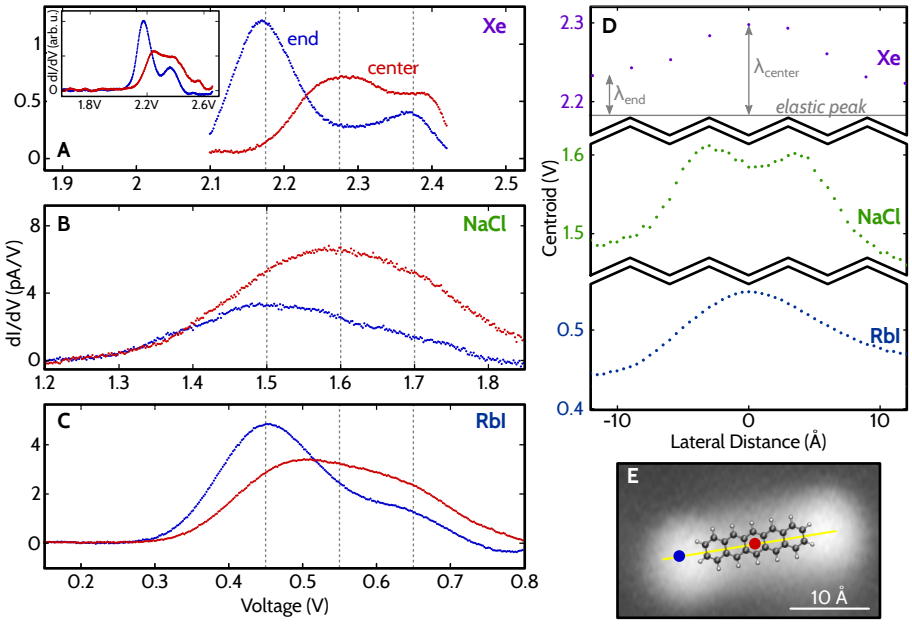

Figure 11.3.: Differential conductance spectroscopy on different insulating films. **A-C** dI/dV curves acquired on pentacene on Xe, NaCl, and RbI, respectively. Note that extremely low currents have been used on Xe to avoid any lateral movements during the measurement series. Spatial positions are indicated in panel **E**. Dashed gray lines indicate voltages of elastic peak and two vibronic peaks, respectively. Inset in **A** shows spectra on Xe for a larger voltage range. **D** The centroid of spectra taken along the long axis of the molecule (indicated by line in panel **E**). For Xe reorganization energies λ are indicated for positions at the end and the center. **E** STM image on Xe ($I = 0.2\,\mathrm{pA},\ V = 2.2\,\mathrm{V}$).

where the summation runs over the vibrational modes; $\hbar\omega_i$ and S_i denote the corresponding vibrational energy and Huang-Rhys factor, respectively. The Huang-Rhys factors can be obtained by means of a normal mode analysis (*104*). In a first step the nuclear displacements between the equilibrium positions of the two electronic states have to be determined. In the case considered here, these would be the displacements upon electron attachment[8]. In a next step, these nuclear displacements (the horizontal offset of the parabolas in figure 11.1) have to be projected

[8] Commonly, the displacements are calculated by DFT (*104*, *157*).

onto the basis of the normal modes (*104*, *157*). Thus, the energy stored in normal mode i is $\lambda_i = \frac{k_i}{2} (\Delta Q_i)^2$, where k_i and ΔQ_i denote its force constant and its nuclear displacement, respectively. Using $\omega_i = \sqrt{k_i/M_i}$, where M_i is the reduced mass of mode i, equation (11.1) can be expressed as

$$\lambda = \sum \frac{1}{2} \omega_i^2 M_i \, (\Delta Q_i)^2 \, . \tag{11.2}$$

That is, the Huang-Rhys factors S_i give the average number of excited quanta for every individual mode i. From this analysis it follows that the difference between the energy of elastic tunneling and the one of the centroid of the entire peak structure equals the reorganization energy λ.

It can be seen from figure 11.3D that λ varies spatially by more than a factor of two. Data on pentacene molecules adsorbed on a bilayer of RbI (figure 11.3C) reveal the same spatial dependence of the peak structure as observed on Xe islands. Also for NaCl as an insulating film (figure 11.3B,D), the centroid of the entire peak structure shows similar lateral variations as for Xe and RbI, apart from a small feature at the center[9]. Hence, these effects have to be associated with tunneling into different parts of the molecule. Pentacene, having only C-H and aromatic C-C bonds distributed over the molecule, does not have highly localized vibrational modes, such that this can also be ruled out as a reason for the different e-ν coupling.

11.3. Spatial Dependence of Vibronic Excitations

To investigate the spatial dependence in detail, we have measured spatial maps of the LUMO-related peak structure on RbI[10]. To visualize

[9] The central lobe of the LUMO also appears more pronounced in constant current images on NaCl (*10*), slightly increasing the local s character at the center.

[10] A drift-correction mechanism based on cross-correlation was performed during data acquisition of the spatial maps. Before starting the first line of spectra an STM image was recorded serving as the reference image. After each line of spectra (~ 40 minutes) the STM tip was moved back to the starting position of the reference image and another STM image was recorded. The lateral drift vector was then

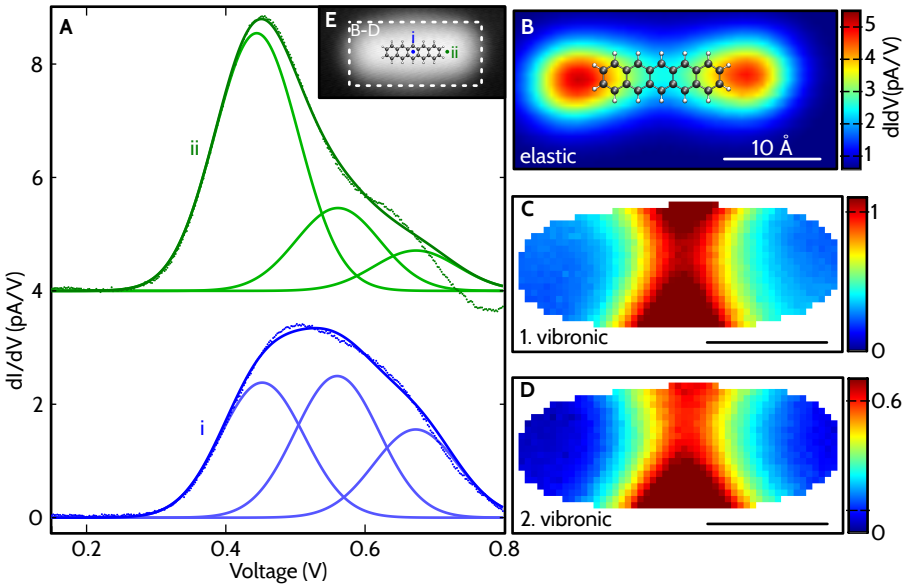

Figure 11.4.: Spatial maps of elastic and vibration-assisted contributions on RbI. Data have been constructed from 63×31 individual dI/dV curves in a rectangle of 31.6 Å $\times$ 15.5 Å above the molecule. **A** Two exemplary dI/dV curves acquired at positions indicated in the inset and the corresponding fits. The slight deviation at bias voltages above the LUMO is due to the tunneling barrier increasing with voltage (*10*). In addition, each of the three Gaussian peaks is shown. **B** Intensity map of the elastic peak. A molecular model is superimposed as a guide to the eye. **C**-**D** Plots of the ratio of the first and second vibronic to the elastic peak. Data are shown only for spots at which the tunneling current significantly exceeds the noise level. **E** Dashed rectangle in the STM image corresponds to the mapped region.

characteristic differences in the measured data, each spectrum was fitted to a sum of three Gaussian curves corresponding to elastic tunneling and two vibronic side peaks at higher energy[11]. The data are

evaluated by cross-correlating reference and test image and subsequent spectra positions were compensated by this drift vector. The accumulated lateral drift between each line was small compared to the grid spacing.

[11] Obtaining the best fit for data in figure 11.4 was done in a least-squares sense. The width of the Gaussians has been fixed, since it is determined by the *e-ph* coupling strength on RbI. The estimated peak positions are indicated in figure 11.3C.

reproduced well by the fits as demonstrated in figure 11.4A. Even small organic molecules exhibit a multitude of vibrational modes with different symmetries (*157–159*). Pentacene has 36 atoms and thus more than 100 vibrational modes. Different modes with an energy around 100 meV can exhibit significant e-ν coupling (*157*). It should also be noted that the mode spacing is on the order of few meV, only. For this reason, and due to energy broadening, there is some arbitrariness in choosing the peak positions for fitting[12]. Note that a small part of the bias voltage drop occurs in the insulating film (*10*). Hence, the energies of the vibronic satellites experimentally observed read $\sim 10\%$ too large.

The elastic contribution, presented in figure 11.4B, is high at the ends of the molecule and smoothly decreases to the center of the molecule. This is consistent with the individual spectra on different insulating films discussed above. The ratio of the vibronic peaks to the elastic peak, presented in figure 11.4C-D, is close to zero at the ends of the molecule. In contrast, the ratio for the first vibronic peak is above unity at the center and the ratio between both vibronic peaks is almost constant. Since both peaks are roughly equidistant, there are two possible explanations for this observation. Either the second peak corresponds to a different vibrational mode or to the excitation of two quanta of the same vibrational mode.

11.4. Dependence on Wave Functions of Tip and Molecule

Next, we will address the physical origin of the observed effect. It was realized long ago, that tunneling from metal tips occurs predominantly via states with s-wave character, since those states penetrate much further into vacuum as compared to others (*40*, *41*). This fact, which has been mentioned in section 7.2.2, can be rationalized by equation (2.10). Of course, the tip wave function can be expanded in the same way. Then, it is clear that high k values lead to a faster decay into the vacuum.

[12] As mentioned above, it is expected that none of the modes is highly localized. Therefore, we refrained from making a direct assignment to a vibrational mode.

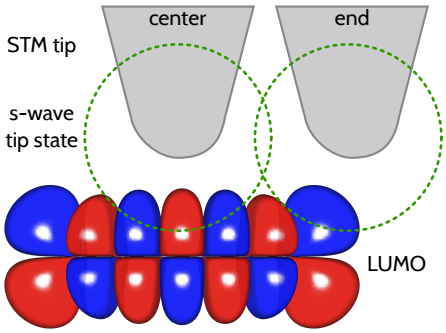

Figure 11.5.: Schematic illustration of elastic tunneling. When the tip is positioned above the outermost lobe of the LUMO, the tunneling matrix element is high. In contrast, when the tip is centered above the molecule, elastic tunneling contributions cancel. The matrix element for *s*-wave tunneling is low.

Recently, it has been realized that this suppresses elastic tunneling into graphene flakes, since in graphene only high-momentum states are available at the Fermi level (*160*). The excitation of a phonon facilitates tunneling by providing the required momentum. In analogy to optical excitations in indirect semiconductors this process was referred to as *phonon-assisted tunneling*. The physical arguments can be carried over to molecular systems, where the local symmetry instead of momentum has to be preserved.

As depicted in figure 11.5, with the tip being located at the end of the molecule, the LUMO exhibits locally *s* character and tunneling can occur via the *s*-wave tip states (*148*). At the center, however, the LUMO has a high nodal plane density and the overlap integral to an *s*-wave tip state is greatly reduced. The tunneling matrix element for tip states of matching *p* symmetry is much smaller, since these states fall off much more rapidly towards the molecule (*40*, *41*). Only, if the tunneling process is accompanied by an excitation of a vibrational mode coupling the two electronic wave functions, tunneling may still proceed via *s*-wave states of the tip. This picture of **vibration-assisted tunneling** provides a straightforward explanation of the spatial variation of elastic and inelastic contributions seen in our experiments.

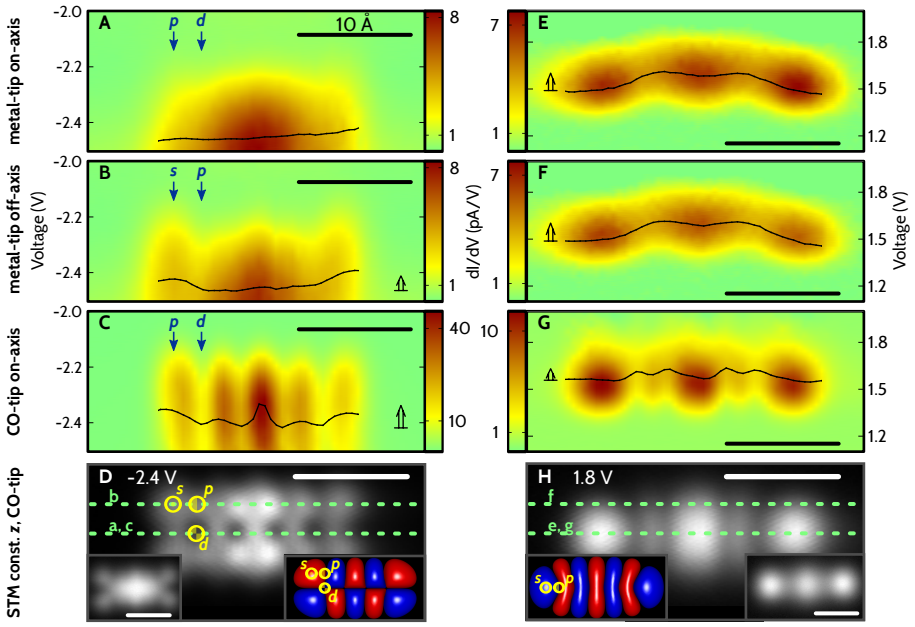

Figure 11.6.: Tip-dependent data acquired on NaCl. **A**-**C** and **E**-**G** Color plots of dI/dV curves of the HOMO and LUMO along the green dashed lines in panels **D** and **H**, respectively. The black curves show the spatially resolved centroid extracted from the spectra. The open arrows roughly indicate their spatial variations reflecting changes in λ. Note that for the HOMO absolute voltage rises from top to bottom. Panels **C** and **G** are acquired with a CO-functionalized tip. **D** and **H** Constant height STM images of HOMO and LUMO, respectively, acquired with a CO tip. Insets show STM images acquired with a metal tip at same voltages and corresponding DFT calculated orbital densities. Exemplary spots of local *s* , *p* and *d* character are indicated. on axis (off axis) refers to the line along (parallel to) the long molecular axis.

To prove that the local symmetry of the orbital is indeed decisive, we compared dI/dV data for tunneling out of the HOMO and into the LUMO along the long molecular axis (on axis) and parallel to it (off axis); see figure 11.6. The data coincide for the LUMO, since the symmetry is the same for on and off axis; see figure 11.6E-F. In contrast, the HOMO has a nodal plane on axis. Neither of the alternating p and d spots match the symmetry of an s-wave tip, resulting in negligible

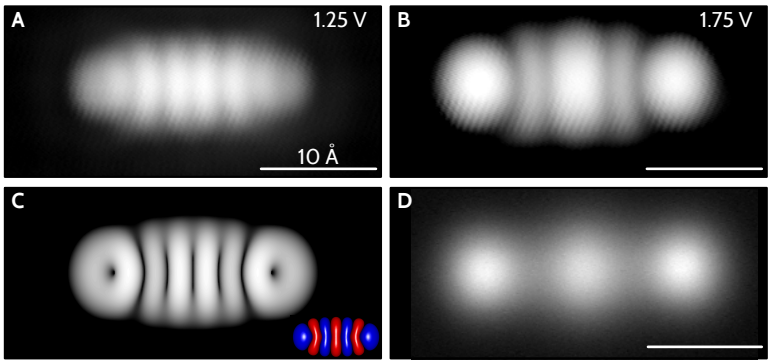

Figure 11.7.: ***p*-wave to *s*-wave tunneling.** **A**-**B** Bias-dependent constant current STM images at the indicated voltages ($I = 2\,\mathrm{pA}$) acquired with a CO tip on NaCl. At low absolute bias voltage *p*-wave tunneling dominates, while at high voltage *s*-wave contributions are enhanced. **C** Calculated *p*-wave STM image (*81*), which has been produced as follows. For the *p*-wave tip we used the $2p$ hydrogen atom wave function with the magnetic quantum number $m = 1$ and an effective nuclear charge of $Z_{\mathrm{eff}} = 2$. For symmetry reasons, the absolute square of the convolution of the tip and the DFT calculated LUMO wave function directly reflects the absolute square of the overlap integral of the two as a function of their relative displacement. The calculated image is a contour of constant value of this quantity. Inset shows DFT calculated orbital density. **D** For comparison with panel **B**, a constant current STM image acquired with a metal-terminated tip ($I = 2\,\mathrm{pA}$, $V = 1.8\,\mathrm{V}$) is shown.

variations of the centroid in figure 11.6A. For the off axis line cut (figure 11.6b) the centroid is shifted to lower absolute voltage at spots of local *s* character. Thus, the data for both orbitals confirm our symmetry considerations.

Another test case for the hypothesis is to suppress the strong preference for *s*-wave tunneling for the tip states. Functionalizing the tip with a CO molecule (*81*) strongly enhances *p*-wave character relative to *s*-wave, due to its π-molecular orbitals. As a CO tip does not have purely p character and the larger penetration of the *s*-wave character into vacuum still holds, the situation is not simply reversed. However, the enhanced *p*-wave character of the tip states should render a different spatial dependence of vibration-assisted tunneling. Indeed we observe

that characteristics and spatial dependence of the peak structure change qualitatively for CO tips, as presented in figure 11.6C,G. In agreement with the assumption that CO tips show s and p character, the deviations of the centroid along the LUMO are smaller for CO tips as compared to metal tips. Now, we consider the HOMO along the molecular axis. In this case, only the p spots match the tip symmetry and hence the variations of the centroid are much more pronounced for CO tips as compared to metal tips.

The concept of vibration-assisted tunneling can be rephrased in the following way: at energies directly corresponding to the electronic excitation (without any excess energy), the local symmetry of sample states has to match the one of the tip. At higher energies, the excess energy can be used to excite a vibrational mode coupling different symmetries in tip and sample. Following this reasoning and assuming that CO tips show predominantly p character (*81*), one would expect to see the p character most pronounced for voltages corresponding to the onset of an electronic resonance. At higher absolute bias voltages, the p character becomes blurred and the s character in the images increases. Our experiments support this picture. A CO tip orbital image at the onset of the LUMO is shown in figure 11.7A. This image nicely resembles the calculated p-wave STM image in figure 11.7C (*81*). As expected, an CO tip orbital image at higher voltage (figure 11.7B) bears more resemblance to an STM image acquired with a metal-tip (figure 11.7D) and hence more s character.

11.5. Conclusions

It has to be emphasized that the physics discussed here is not limited to STM experiments. For example, it will be relevant for electron hopping in organic crystals (*161*, *162*). One of many possible technical applications include organic solar cells, which seem to be very prospective (*31*, *33*).

The results presented in this chapter demonstrate how the reorganization energy λ can be measured spatially resolved and that its spatial

variations exceed a factor of two. These findings suggest that the dissipation in electron transport through organic semiconductors will strongly depend on the alignment of orbitals of adjacent molecules and therefore be highly dependent on the crystal structure. Similarly, it sheds new light on single molecule electronics (*143*, *144*, *163*), where it is relevant for the coupling to the lead.

12. Conclusions

In this thesis, I have presented the results of three topics, which will be quickly summarized in this chapter.

STM Head in High Magnetic Fields

The design, construction, and assembly of an STM head to be operated in high magnetic fields and at low temperature was subject of chapter 9. The body of the STM head, manufactured from phosphor bronze, has been divided into different functional parts. Thereby, a modular design could be established.

Despite the small dimensions of the STM head with a diameter of 21 mm and a total length of 49.5 mm, a piezo motor for lateral coarse movements could be incorporated. Besides, the microscope features a simple tip-exchange mechanism to allow spin-polarized STM.

The vertical coarse approach constituting the key component of an STM has proven to work reliably at ambient conditions. However, it remains to be seen wether adjustment of operating parameters at low temperatures will be similarly straightforward.

Finite element analysis shows that the fundamental eigenfrequency is at 3.6 kHz. This proves that the goal of a very rigid body has been achieved. It can be expected that this vibrational immunity to external disturbances will allow low-noise STS measurements.

Revealing Bistable Configurations of Dibenzo[a,h]thianthrene

Dibenzo[a,h]thianthrene (DBTH) molecules adsorbed on ultrathin layers of NaCl have been investigated using combined low temperature STM and AFM. Two stable configurations exist corresponding to different isomers of free nonplanar molecules. Excitations from inelastic

electron tunneling allow to reversibly switch between both configurations.

AFM with submolecular resolution unambiguously determined the molecular geometry of both configurations of these nonplanar molecules. Our observations demonstrate that DBTH and related molecules may act as ideal benchmarks for three-dimensional force mapping.

Besides, the pathway of the interconversion of the isomers was analyzed by taking the chirality of the molecules into account. Flapping of the molecular "wings" could be identified as the mechanism of the molecular switch.

Finally, these investigations also shed new light on contrast mechanisms in scanning tunneling microscopy. Commonly, STM images of molecules at low bias are said to somehow resemble the molecular geometry. In contrast, our experiments show a qualitative difference between STM images in both configurations. Surprisingly, this is the case even though the molecular structure projected onto the surface plane remains unchanged.

Symmetry-Dependence of Vibration-Assisted Tunneling

Spatially-resolved vibronic spectroscopy of individual pentacene molecules on different insulating films has been presented. It is observed that even for this effective single-level system the energy dissipation associated with electron attachment varies spatially by more than a factor of two. This is in contrast to the usual treatment of electron-vibron coupling in the Franck-Condon picture.

This picture could be substantiated by varying the insulating films (Xe, RbI, NaCl), the involved molecular orbitals (HOMO, LUMO) and finally by choosing well-defined tip-terminations (metal, CO).

In particular, our experiments unambiguously prove that the local symmetry of initial and final wave function determines the dissipation in electron transport. Since tip states with *s*-symmetry penetrate further into the vacuum as compared to other symmetries, these states dominate elastic tunneling. That is, at the onset of an electronic resonance (*zero*

phonon transition) electrons from an *s*-wave metal tip tunnel predominantly into the molecule at spots of local *s*-symmetry. Only electrons with sufficiently high excess energy may excite molecular vibrations and hence allow tunneling at spots of local *p*-symmetry (*vibrationally-assisted tunneling*).

A single CO-molecule at the tip apex favors *p*-wave tunneling as compared to *s*-wave tunneling due to its π molecular orbitals. In this case, spots of local *p*-symmetry in the molecule match the tip-symmetry and hence elastic tunneling is allowed. However, it is observed that tunneling at spots of local *d*-symmetry is highly suppressed. This demonstrates that no vibrations with a matching deformation potential can be found.

It has to be emphasized that this phenomena is not limited to STM experiments. On the contrary, electron transport through organic semiconductors underlies the same physics. The findings presented here suggest that dissipation will strongly depend on the crystal structure. When the overlap of adjacent electronic orbitals do not match in their symmetry, dissipation will be highly increased, since hopping can only occur by means of vibrationally-assisted tunneling.

Bibliography

1. G. Binnig, H. Rohrer, C. Gerber, E. Weibel, *Tunneling through a Controllable Vacuum Gap*. Applied Physics Letters **40**, 178 (1982).
2. G. Binnig, H. Rohrer, C. Gerber, E. Weibel, *Surface Studies by Scanning Tunneling Microscopy*. Physical Review Letters **49**, 57 (1982).
3. G. Binnig, H. Rohrer, C. Gerber, E. Weibel, *7x7 Reconstruction on Si(111) Resolved in Real Space*. Physical Review Letters **50**, 120 (1983).
4. G. Binnig, K. H. Frank, H. Fuchs, N. Garcia, B. Reihl, H. Rohrer, F. Salvan, A. R. Williams, *Tunneling Spectroscopy and Inverse Photoemission: Image and Field States*. Physical Review Letters **55**, 991 (1985).
5. D. M. Eigler, E. K. Schweizer, *Positioning Single Atoms with a Scanning Tunnelling Microscope*. Nature **344**, 524 (1990).
6. R. P. Feynman, *There's Plenty of Room at the Bottom: An Invitation to Enter a New Field of Physics*, presented at the Meeting of the American Physical Society (Dec. 1959), Caltech, Pasadena, USA, Dec. 1959.
7. G. Binnig, C. F. Quate, C. Gerber, *Atomic Force Microscope*. Physical Review Letters **56**, 930 (1986).
8. F. J. Giessibl, *Atomic Resolution of the Silicon (111)-(7x7) Surface by Atomic Force Microscopy*. Science **267**, 68 (1995).
9. T. R. Albrecht, P. Grütter, D. Horne, D. Rugar, *Frequency Modulation Detection Using High-Q Cantilevers for Enhanced Force Microscope Sensitivity*. Journal of Applied Physics **69**, 668 (1991).

10. J. Repp, G. Meyer, S. M. Stojković, A. Gourdon, C. Joachim, *Molecules on Insulating Films: Scanning Tunneling Microscopy Imaging of Individual Molecular Orbitals*. Physical Review Letters **94**, 026803 (2005).

11. A. J. Heinrich, J. A. Gupta, C. P. Lutz, D. M. Eigler, *Single-Atom Spin-Flip Spectroscopy*. Science **306**, 466 (2004).

12. C. F. Hirjibehedin, C. P. Lutz, A. J. Heinrich, *Spin Coupling in Engineered Atomic Structures*. Science **312**, 1021 (2006).

13. C. F. Hirjibehedin, C.-Y. Lin, A. F. Otte, M. Ternes, C. P. Lutz, B. A. Jones, A. J. Heinrich, *Large Magnetic Anisotropy of a Single Atomic Spin Embedded in a Surface Molecular Network*. Science **317**, 1199 (2007).

14. S. Loth, M. Etzkorn, C. P. Lutz, D. M. Eigler, A. J. Heinrich, *Measurement of Fast Electron Spin Relaxation Times with Atomic Resolution*. Science **329**, 1628 (2010).

15. Y.-S. Fu, S.-H. Ji, T. Zhang, X. Chen, X.-C. Ma, J.-F. Jia, Q.-K. Xue, *Ultrathin Lead Oxide Film on Pb(111) and Its Application in Single Spin Detection*. Applied Physics Letters **95**, 063107 (2009).

16. N. Tsukahara *et al.*, *Adsorption-Induced Switching of Magnetic Anisotropy in a Single Iron(II) Phthalocyanine Molecule on an Oxidized Cu(110) Surface*. Physical Review Letters **102**, 167203 (2009).

17. B. C. Stipe, M. A. Rezaei, W. Ho, *Single-Molecule Vibrational Spectroscopy and Microscopy*. Science **280**, 1732 (1998).

18. S. H. Pan, E. W. Hudson, J. C. Davis, *^{3}He Refrigerator Based Very Low Temperature Scanning Tunneling Microscope*. Review of Scientific Instruments **70**, 1459 (1999).

19. T. Mashoff, M. Pratzer, M. Morgenstern, *A Low-Temperature High Resolution Scanning Tunneling Microscope with a Three-Dimensional Magnetic Vector Field Operating in Ultrahigh Vacuum*. Review of Scientific Instruments **80**, 053702 (2009).

20. S. Meckler, M. Gyamfi, O. Pietzsch, R. Wiesendanger, *A Low-Temperature Spin-Polarized Scanning Tunneling Microscope Operating in a Fully Rotatable Magnetic Field.* Review of Scientific Instruments **80**, 023708 (2009).

21. Y. J. Song, A. F. Otte, V. Shvarts, Z. Zhao, Y. Kuk, S. R. Blankenship, A. Band, F. M. Hess, J. A. Stroscio, *Invited Review Article: A 10 mK Scanning Probe Microscopy Facility.* Review of Scientific Instruments **81**, 121101 (2010).

22. Y. J. Song *et al.*, *High-Resolution Tunnelling Spectroscopy of a Graphene Quartet.* Nature **467**, 185 (2010).

23. M. Assig, K. Kern, *Development of a Millikelvin Scanning Tunneling Microscope for Applications in Ultra High Vacuum and High Magnetic Fields.* Ph.D. thesis, École Polytechnique Fédérale de Lausanne (EPFL), 2011.

24. F. J. Giessibl, *Atomic Resolution on Si(111)-(7×7) by Noncontact Atomic Force Microscopy with a Force Sensor Based on a Quartz Tuning Fork.* Applied Physics Letters **76**, 1470 (2000).

25. M. Ternes, C. P. Lutz, C. F. Hirjibehedin, F. J. Giessibl, A. J. Heinrich, *The Force Needed to Move an Atom on a Surface.* Science **319**, 1066 (2008).

26. L. Gross, F. Mohn, N. Moll, P. Liljeroth, G. Meyer, *The Chemical Structure of a Molecule Resolved by Atomic Force Microscopy.* Science **325**, 1110 (2009).

27. L. Gross, F. Mohn, N. Moll, G. Meyer, R. Ebel, W. M. Abdel-Mageed, M. Jaspars, *Organic Structure Determination Using Atomic-Resolution Scanning Probe Microscopy.* Nature Chemistry **2**, 821 (2010).

28. F. Mohn, L. Gross, G. Meyer, *Measuring the Short-Range Force Field Above a Single Molecule with Atomic Resolution.* Applied Physics Letters **99**, 053106 (2011).

29. F. Mohn, L. Gross, N. Moll, G. Meyer, *Imaging the Charge Distribution within a Single Molecule.* Nature Nanotechnology **7**, 227 (2012).

30. J. Welker, F. J. Giessibl, *Revealing the Angular Symmetry of Chemical Bonds by Atomic Force Microscopy.* Science **336**, 444 (2012).

31. C.-C. Chen, L. Dou, R. Zhu, C.-H. Chung, T.-B. Song, Y. B. Zheng, S. Hawks, G. Li, P. S. Weiss, Y. Yang, *Visibly Transparent Polymer Solar Cells Produced by Solution Processing.* ACS Nano **6**, 7185 (2012).

32. G. Li, R. Zhu, Y. Yang, *Polymer Solar Cells.* Nature Photonics **6**, 153 (2012).

33. M. Kaltenbrunner, M. S. White, E. D. Głowacki, T. Sekitani, T. Someya, N. S. Sariciftci, S. Bauer, *Ultrathin and Lightweight Organic Solar Cells with High Flexibility.* Nature Communications **3**, 770 (2012).

34. J. R. Heath, *Molecular Electronics.* Annual Review of Materials Research **39**, 1 (2009).

35. J. S. Prauzner-Bechcicki, S. Godlewski, M. Szymonski, *Front Cover: Atomic- and Molecular-Scale Devices and Systems for Single-Molecule Electronics (phys. status solidi A 4/2012).* physica status solidi (a) **209**, n/a (2012).

36. C. Cohen-Tannoudji, B. Diu, F. Laloë, *Quantenmechanik 1* (de Gruyter, New York, 1999).

37. C. J. Chen, *Introduction to Scanning Tunneling Microscopy* (Oxford University Press, New York, ed. 2, 2008).

38. J. Bardeen, *Tunnelling from a Many-Particle Point of View.* Physical Review Letters **6**, 57 (1961).

39. J. Bardeen, L. N. Cooper, J. R. Schrieffer, *Theory of Superconductivity.* Physical Review **108**, 1175 (1957).

40. J. Tersoff, D. R. Hamann, *Theory and Application for the Scanning Tunneling Microscope.* Physical Review Letters **50**, 1998 (1983).

41. J. Tersoff, D. R. Hamann, *Theory of the Scanning Tunneling Microscope.* Physical Review B **31**, 805 (1985).

42. F. Ohnesorge, G. Binnig, *True Atomic Resolution by Atomic Force Microscopy Through Repulsive and Attractive Forces.* Science **260**, 1451 (1993).

43. F. Ohnesorge *et al.*, *Scanning Force Microscopy Studies of the S-Layers From Bacillus Coagulans E38–66, Bacillus Sphaericus CCM2177 and of an Antibody Binding Process.* Ultramicroscopy **42–44, Part 2**, 1236 (1992).

44. Y. Martin, C. C. Williams, H. K. Wickramasinghe, *Atomic Force Microscope–Force Mapping and Profiling on a Sub 100-Å Scale.* Journal of Applied Physics **61**, 4723 (1987).

45. F. J. Giessibl, *Advances in Atomic Force Microscopy.* Reviews of Modern Physics **75**, 949 (2003).

46. F. J. Giessibl, in *Noncontact Atomic Force Microscopy*, ed. by S. Morita, R. Wiesendanger, E. Meyer (Springer Berlin Heidelberg, Heidelberg Berlin, 2002), vol. 1, chapter 2.

47. F. J. Giessibl, in *Noncontact Atomic Force Microscopy*, ed. by S. Morita, F. J. Giessibl, R. Wiesendanger (Springer Berlin Heidelberg, Heidelberg Berlin, 2009), vol. 2, chapter 6.

48. J. N. Israelachvili, *Intermolecular and Surface Forces* (Elsevier Science, Revised Third Edition, 2011).

49. F. J. Giessibl, *Theory for an Electrostatic Imaging Mechanism Allowing Atomic Resolution of Ionic Crystals by Atomic Force Microscopy.* Physical Review B **45**, 13815 (1992).

50. M. Nonnenmacher, M. P. O'Boyle, H. K. Wickramasinghe, *Kelvin Probe Force Microscopy.* Applied Physics Letters **58**, 2921 (1991).

51. Y. Martin, H. K. Wickramasinghe, *Magnetic Imaging by "Force Microscopy" with 1000 Å Resolution.* Applied Physics Letters **50**, 1455 (1987).

52. J. J. Saenz, N. Garcia, P. Grutter, E. Meyer, H. Heinzelmann, R. Wiesendanger, L. Rosenthaler, H. R. Hidber, H.-J. Güntherodt, *Observation of Magnetic Forces by the Atomic Force Microscope.* Journal of Applied Physics **62**, 4293 (1987).

53. U. Kaiser, A. Schwarz, R. Wiesendanger, *Magnetic Exchange Force Microscopy with Atomic Resolution*. Nature **446**, 522 (2007).

54. J. E. Jones, *On the Determination of Molecular Fields. II. From the Equation of State of a Gas*. Proceedings of the Royal Society of London. Series A **106**, 463 (1924).

55. R. A. Buckingham, *The Classical Equation of State of Gaseous Helium, Neon and Argon*. Proceedings of the Royal Society of London. Series A. Mathematical and Physical Sciences **168**, 264 (1938).

56. P. M. Morse, *Diatomic Molecules According to the Wave Mechanics. II. Vibrational Levels*. Physical Review **34**, 57 (1929).

57. A. Zangwill, *Physics at Surfaces* (Cambridge University Press, Cambridge, 1996).

58. J. W. Ekin, *Experimental Techniques for Low-Temperature Measurements* (Oxford University Press, National Institute of Standards and Technology, Boulder, CO, 2006).

59. NASA, *Outgassing Data for Selecting Spacecraft Materials*, online, `http://outgassing.nasa.gov`.

60. C. Kittel, *Einführung in die Festkörperphysik*, hrsg. von S. Hunklinger (Oldenbourg Verlag, Aufl. 14, 2006).

61. J. Singleton, *Band Theory and Electronic Properties of Solids* (Oxford University Press, 2001).

62. CRC, *Handbook of Chemistry and Physics*, ed. by D. R. Lide (CRC Press, Boca Raton, ed. 90, 2009).

63. M. Buttiker, *Coherent and Sequential Tunneling in Series Barriers*. IBM Journal of Research and Development **32**, 63 (1988).

64. K. Uchida, in *Nanoelectronics and Information Technology: Advanced Electronic Materials and Novel Devices*, ed. by R. Waser (Wiley, New York, ed. 2, 2003), chapter 16.

65. R. Stomp, Y. Miyahara, S. Schaer, Q. Sun, H. Guo, P. Grutter, S. Studenikin, P. Poole, A. Sachrajda, *Detection of Single-Electron Charging in an Individual InAs Quantum Dot by Noncontact Atomic-Force Microscopy*. Physical Review Letters **94**, 056802 (2005).

66. P. W. Anderson, *Localized Magnetic States in Metals*. Physical Review **124**, 41 (1961).

67. D. M. Newns, *Self-Consistent Model of Hydrogen Chemisorption*. Physical Review **178**, 1123 (1969).

68. J. Repp, *Level Broadening on Insulating Films*, private communication, 2009.

69. J. Repp, G. Meyer, S. Paavilainen, F. E. Olsson, M. Persson, *Scanning Tunneling Spectroscopy of Cl Vacancies in NaCl Films: Strong Electron-Phonon Coupling in Double-Barrier Tunneling Junctions*. Physical Review Letters **95**, 225503 (2005).

70. D. M. Eigler, C. P. Lutz, W. E. Rudge, *An Atomic Switch Realized with the Scanning Tunnelling Microscope*. Nature **352**, 600 (1991).

71. T. Komeda, Y. Kim, M. Kawai, B. N. J. Persson, H. Ueba, *Lateral Hopping of Molecules Induced by Excitation of Internal Vibration Mode*. Science **295**, 2055 (2002).

72. T. Sonnleitner, I. Swart, N. Pavliček, A. Pöllmann, J. Repp, *Molecular Symmetry Governs Surface Diffusion*. Physical Review Letters **107**, 186103 (2011).

73. T. Sonnleitner, *Symmetrien und Manipulation des Ladungszustands von Molekülen auf NaCl-Filmen*. Diss., Universität Regensburg, Dez. 2011.

74. I. Swart, T. Sonnleitner, J. Niedenführ, J. Repp, *Controlled Lateral Manipulation of Molecules on Insulating Films by STM*. Nano Letters **12**, 1070 (2012).

75. N. Moll, L. Gross, F. Mohn, A. Curioni, G. Meyer, *The Mechanisms Underlying the Enhanced Resolution of Atomic Force Microscopy with Functionalized Tips*. New Journal of Physics **12**, 125020 (2010).

76. A. Schwarz, U. Kaiser, R. Schmidt, R. Wiesendanger, in *Noncontact Atomic Force Microscopy*, ed. by S. Morita, F. J. Giessibl, R. Wiesendanger (Springer Berlin Heidelberg, Heidelberg Berlin, 2009), vol. 2, chapter 13.

77. M. Neu, *to be submitted*. Diss., Universität Regensburg, 2013.

78. U. Dürig, H. R. Steinauer, N. Blanc, *Dynamic Force Microscopy by Means of the Phase-Controlled Oscillator Method*. Journal of Applied Physics **82**, 3641 (1997).

79. W. Pauli, *Über den Zusammenhang des Abschlusses der Elektronengruppen im Atom mit der Komplexstruktur der Spektren*. Zeitschrift für Physik A Hadrons and Nuclei **31**, 765 (1925).

80. C. Weiss, C. Wagner, R. Temirov, F. S. Tautz, *Direct Imaging of Intermolecular Bonds in Scanning Tunneling Microscopy*. Journal of the American Chemical Society **132**, 11864 (2010).

81. L. Gross, N. Moll, F. Mohn, A. Curioni, G. Meyer, F. Hanke, M. Persson, *High-Resolution Molecular Orbital Imaging Using a p-Wave STM Tip*. Physical Review Letters **107**, 086101 (2011).

82. G. Meyer, *A Simple Low-Temperature Ultrahigh-Vacuum Scanning Tunneling Microscope Capable of Atomic Manipulation*. Review of Scientific Instruments **67**, 2960 (1996).

83. S. Zöphel, *Der Aufbau eines Tieftemperatur-Rastertunnelmikroskops und Strukturuntersuchungen auf vicinalen Kupferoberflächen*. Diss., Freie Universität Berlin, 2000.

84. SPS-Createc GmbH, Magnusstr. 11, 12489 Berlin, Germany, `http://www.sps-createc.com`.

85. K. Besocke, *An Easily Operable Scanning Tunneling Microscope*. Surface Science **181**, 145 (1987).

86. W. Shockley, *On the Surface States Associated With a Periodic Potential*. Physical Review **56**, 317 (1939).

87. J. Repp, *Rastertunnelmikroskopie und -spektroskopie an Adsorbaten auf Metall- und Isolator-Oberflächen*. Diss., Freie Universität Berlin, 2002.

88. J. Repp, G. Meyer, *Gezielte Umladung einzelner Goldatome.* Physik in unserer Zeit **35**, 207 (2004).

89. J. Repp, G. Meyer, F. E. Olsson, M. Persson, *Controlling the Charge State of Individual Gold Adatoms.* Science **305**, 493 (2004).

90. I. Swart, T. Sonnleitner, J. Repp, *Charge State Control of Molecules Reveals Modification of the Tunneling Barrier with Intramolecular Contrast.* Nano Letters **11**, 1580 (2011).

91. J. Repp, S. Fölsch, G. Meyer, K.-H. Rieder, *Ionic Films on Vicinal Metal Surfaces: Enhanced Binding Due to Charge Modulation.* Physical Review Letters **86**, 252 (2001).

92. S. Fölsch, A. Riemann, J. Repp, G. Meyer, K.-H. Rieder, *From Atomic Kinks to Mesoscopic Surface Patterns: Ionic Layers on Vicinal Metal Surfaces.* Physical Review B **66**, 161409 (2002).

93. R. Smoluchowski, *Anisotropy of the Electronic Work Function of Metals.* Physical Review **60**, 661 (1941).

94. J.-Y. Park, S.-J. Kahng, U. D. Ham, Y. Kuk, K. Miyake, K. Hata, H. Shigekawa, *Adsorption and Growth of Xe Adlayers on the Cu(111) Surface.* Physical Review B **60**, 16934 (1999).

95. A. Šiber, B. Gumhalter, J. Braun, A. P. Graham, M. F. Bertino, J. P. Toennies, D. Fuhrmann, C. Wöll, *Combined He-Atom Scattering and Theoretical Study of the Low-Energy Vibrations of Physisorbed Monolayers of Xe on Cu(111) and Cu(001).* Physical Review Letters **59**, 5898 (1999).

96. L. Bartels, G. Meyer, K.-H. Rieder, *Controlled Vertical Manipulation of Single CO Molecules with the Scanning Tunneling Microscope: A Route to Chemical Contrast.* Applied Physics Letters **71**, 213 (1997).

97. W. Kohn, *Nobel Lecture: Electronic Structure of Matter – Wave Functions and Density Functionals.* Reviews of Modern Physics **71**, 1253 (1999).

98. K. Burke, *Perspective on Density Functional Theory.* The Journal of Chemical Physics **136**, 150901 (2012).

99. P. Hohenberg, W. Kohn, *Inhomogeneous Electron Gas.* Physical Review **136**, B864 (1964).

100. W. Kohn, L. J. Sham, *Self-Consistent Equations Including Exchange and Correlation Effects*. Physical Review **140**, A1133 (1965).

101. T. Koopmans, *Über die Zuordnung von Wellenfunktionen und Eigenwerten zu den einzelnen Elektronen eines Atoms*. Physica **1**, 104 (1934).

102. R. O. Jones, O. Gunnarsson, *The Density Functional Formalism, its Applications and Prospects*. Reviews of Modern Physics **61**, 689 (1989).

103. CPMD V3.15, Copyright IBM Corp. 1990-2011, Copyright MPI für Festkörperforschung Stuttgart 1997-2001, `http://www.cpmd.org`.

104. V. Coropceanu, M. Malagoli, D. A. da Silva Filho, N. E. Gruhn, T. G. Bill, J. L. Brédas, *Hole- and Electron-Vibrational Couplings in Oligoacene Crystals: Intramolecular Contributions*. Physical Review Letters **89**, 275503 (2002).

105. C. C. Mattheus, G. A. de Wijs, R. A. de Groot, T. T. M. Palstra, *Modeling the Polymorphism of Pentacene*. Journal of the American Chemical Society **125**, 6323 (2003).

106. R. Endres, C. Fong, L. Yang, G. Witte, C. Wöll, *Structural and Electronic Properties of Pentacene Molecule and Molecular Pentacene Solid*. Computational Materials Science **29**, 362 (2004).

107. H. Yamane, H. Fukagawa, S. Nagamatsu, M. Ono, S. Kera, K. K. Okudaira, N. Ueno, *Direct Observation of HOMO-Hole/Vibration Coupling in Pentacene Thin Films by Means of High-Resolution Ultraviolet Photoelectron Spectroscopy*, presented at the The International Symposium on Super-Functionality Organic Devices. IPAP Conference Series 6 (Oct. 2004).

108. J. P. Perdew, K. Burke, M. Ernzerhof, *Generalized Gradient Approximation Made Simple*. Physical Review Letters **77**, 3865 (1996).

109. D. R. Hamann, *Generalized Norm-Conserving Pseudopotentials*. Physical Review B **40**, 2980 (1989).

110. D. Rappoport, N. R. M. Crawford, F. Furche, K. Burke, in *Encyclopedia of Inorganic Chemistry*, ed. by E. I. Solomon, R. B. King, R. A. Scott (John Wiley and Sons, Ltd, Chichester, 2009), pp 159–172.

111. I. Rowe, B. Post, *The Crystal Structure of Thianthrene.* Acta Crystallographica **11**, 372 (1958).

112. H. Lynton, E. G. Cox, *954. The Crystal and Molecular Structure of Thianthren.* Journal of the Chemical Society, 4886 (1956).

113. J. Stenhouse, *Ueber die Producte der Trockenen Destillation der Sulfobenzolsauren Salze.* Justus Liebigs Annalen der Chemie **149**, 247 (1869).

114. M. J. Aroney, R. J. W. Le Fevre, J. D. Saxby, *92. Molecular Polarisability. The Apparent Conformations of Thianthren and of Three of its Oxides as Solutes in Benzene.* Journal of the Chemical Society, 571 (1965).

115. K. L. Gallaher, S. H. Bauer, *Structure and Inversion Potential of Thianthren.* Journal of the Chemical Society, Faraday Transactions 2 **71**, 1173 (1975).

116. S. Hosoya, *Molecular Shapes of Thianthrene and Related Heterocyclic Compounds.* Acta Crystallographica **16**, 310 (1963).

117. S. Loth, S. Baumann, C. P. Lutz, D. M. Eigler, A. J. Heinrich, *Bistability in Atomic-Scale Antiferromagnets.* Science **335**, 196 (2012).

118. A. Cano, I. Paul, *Aharonov-Bohm Oscillations in the Local Density of States.* Physical Review B **80**, 153401 (2009).

119. J. Lambe, R. C. Jaklevic, *Molecular Vibration Spectra by Inelastic Electron Tunneling.* Physical Review **165**, 821 (1968).

120. Edwards GmbH, Ammerthalstrasse 36, 85551 Kirchheim, `http://www.edwardsvacuum.de`.

121. P. Gorla, C. Bucci, S. Pirro, *Complete Elimination of 1K Pot Vibrations in Dilution Refrigerators.* Nuclear Instruments and Methods in Physics Research Section A: Accelerators, Spectrometers, Detectors and Associated Equipment **520**, 641 (2004).

122. S.-i. Park, C. F. Quate, *Theories of the Feedback and Vibration Isolation Systems for the Scanning Tunneling Microscope.* Review of Scientific Instruments **58**, 2004 (1987).

123. M. Okano, K. Kajimura, S. Wakiyama, F. Sakai, W. Mizutani, M. Ono, *Vibration Isolation for Scanning Tunneling Microscopy.* Journal of Vacuum Science & Technology A: Vacuum, Surfaces, and Films **5**, 3313 (1987).

124. C. R. Ast, M. Assig, A. Ast, K. Kern, *Design Criteria for Scanning Tunneling Microscopes to Reduce the Response to External Mechanical Disturbances.* Review of Scientific Instruments **79**, 093704 (2008).

125. O. Pietzsch, A. Kubetzka, D. Haude, M. Bode, R. Wiesendanger, *A Low-Temperature Ultrahigh Vacuum Scanning Tunneling Microscope with a Split-Coil Magnet and a Rotary Motion Stepper Motor for High Spatial Resolution Studies of Surface Magnetism.* Review of Scientific Instruments **71**, 424 (2000).

126. H. Kambara, T. Matsui, Y. Niimi, H. Fukuyama, *Construction of a Versatile Ultralow Temperature Scanning Tunneling Microscope.* Review of Scientific Instruments **78**, 073703 (2007).

127. S. C. White, U. R. Singh, P. Wahl, *A Stiff Scanning Tunneling Microscopy Head for Measurement at Low Temperatures and in High Magnetic Fields.* Review of Scientific Instruments **82**, 113708 (2011).

128. S. Schmaus, A. Bagrets, Y. Nahas, T. K. Yamada, A. Bork, M. Bowen, E. Beaurepaire, F. Evers, W. Wulfhekel, *Giant Magnetoresistance Through a Single Molecule.* Nature Nanotechnology **6**, 185 (2011).

129. N. Pavliček, B. Fleury, M. Neu, J. Niedenführ, C. Herranz-Lancho, M. Ruben, J. Repp, *Atomic Force Microscopy Reveals Bistable Configurations of Dibenzo[a,h]thianthrene and their Interconversion Pathway.* Physical Review Letters **108**, 086101 (2012).

130. T. A. Jung, R. R. Schlittler, J. K. Gimzewski, *Conformational Identification of Individual Adsorbed Molecules with the STM.* Nature **386**, 696 (1997).

131. W. Auwärter, F. Klappenberger, A. Weber-Bargioni, A. Schiffrin, T. Strunskus, C. Wöll, Y. Pennec, A. Riemann, J. V. Barth, *Conformational Adaptation and Selective Adatom Capturing of Tetrapyridyl-porphyrin Molecules on a Copper (111) Surface.* Journal of the American Chemical Society **129**, 11279 (2007).

132. A. Weber-Bargioni, W. Auwärter, F. Klappenberger, J. Reichert, S. Lefrançois, T. Strunskus, C. Wöll, A. Schiffrin, Y. Pennec, J. V. Barth, *Visualizing the Frontier Orbitals of a Conformationally Adapted Metalloporphyrin.* ChemPhysChem **9**, 89 (2008).

133. A. Spurg, G. Schnakenburg, S. R. Waldvogel, *Oxidative Coupling of Diaryldisulfides by MoCl5 to Thianthrenes.* Chemistry – A European Journal **15**, 13313 (2009).

134. C. Loppacher, M. Guggisberg, O. Pfeiffer, E. Meyer, M. Bammerlin, R. Lüthi, R. Schlittler, J. K. Gimzewski, H. Tang, C. Joachim, *Direct Determination of the Energy Required to Operate a Single Molecule Switch.* Physical Review Letters **90**, 066107 (2003).

135. R. Raval, *Chiral Expression From Molecular Assemblies at Metal Surfaces: Insights from Surface Science Techniques.* Chemical Society Reviews **38**, 707 (2009).

136. M. J. Comstock, D. A. Strubbe, L. Berbil-Bautista, N. Levy, J. Cho, D. Poulsen, J. M. J. Fréchet, S. G. Louie, M. F. Crommie, *Determination of Photoswitching Dynamics through Chiral Mapping of Single Molecules Using a Scanning Tunneling Microscope.* Physical Review Letters **104**, 178301 (2010).

137. Y. Sugimoto, P. Pou, M. Abe, P. Jelinek, R. Perez, S. Morita, O. Custance, *Chemical Identification of Individual Surface Atoms by Atomic Force Microscopy.* Nature **446**, 64 (2007).

138. J. E. Sader, S. P. Jarvis, *Accurate Formulas for Interaction Force and Energy in Frequency Modulation Force Spectroscopy.* Applied Physics Letters **84**, 1801 (2004).

139. J. Welker, E. Illek, F. J. Giessibl, *Analysis of Force-Deconvolution Methods in Frequency-Modulation Atomic Force Microscopy.* Beilstein Journal of Nanotechnology **3**, 238 (2012).

140. M. Herz, F. J. Giessibl, J. Mannhart, *Probing the Shape of Atoms in Real Space.* Physical Review B **68**, 045301 (2003).

141. N. Pavliček, I. Swart, J. Niedenführ, G. Meyer, J. Repp, *Symmetry-Dependence of Vibration-Assisted Tunneling.* Physical Review Letters **110**, 136101 (2013).

142. V. Coropceanu, J. Cornil, D. A. da Silva Filho, Y. Olivier, R. Silbey, J.-L. Brédas, *Charge Transport in Organic Semiconductors.* Chemical Reviews **107**, 926 (2007).

143. A. Nitzan, M. A. Ratner, *Electron Transport in Molecular Wire Junctions.* Science **300**, 1384 (2003).

144. M. Di Ventra, S. T. Pantelides, N. D. Lang, *Current-Induced Forces in Molecular Wires.* Physical Review Letters **88**, 046801 (2002).

145. X. H. Qiu, G. V. Nazin, W. Ho, *Vibronic States in Single Molecule Electron Transport.* Physical Review Letters **92**, 206102 (2004).

146. K. W. Hipps, U. Mazur, $^4A_2 \rightarrow {}^4T_2$ *and* $^4A_2 \rightarrow {}^4T_1$ *Electronic Transitions in Cobalt(II) Tetrachloride: An FT-IR and Inelastic Electron Tunneling Spectroscopy Study.* Journal of the American Chemical Society **109**, 3861 (1987).

147. M. Paulsson, T. Frederiksen, H. Ueba, N. Lorente, M. Brandbyge, *Unified Description of Inelastic Propensity Rules for Electron Transport through Nanoscale Junctions.* Physical Review Letters **100**, 226604 (2008).

148. A. Garcia-Lekue, D. Sanchez-Portal, A. Arnau, T. Frederiksen, *Simulation of Inelastic Electron Tunneling Spectroscopy of Single Molecules with Functionalized Tips.* Physical Review B **83**, 155417 (2011).

149. N. Lorente, M. Persson, L. J. Lauhon, W. Ho, *Symmetry Selection Rules for Vibrationally Inelastic Tunneling.* Physical Review Letters **86**, 2593 (2001).

150. J. R. Hahn, W. Ho, *Spatially Inhomogeneous Inelastic Electron Tunneling in Oxygen-Ethylene Complexes on Ag(110) Resolved with a Scanning Tunneling Microscope.* Physical Review B **80**, 165428 (2009).

151. I. M. Rutenberg, O. A. Scherman, R. H. Grubbs, W. Jiang, E. Garfunkel, Z. Bao, *Synthesis of Polymer Dielectric Layers for Organic Thin Film Transistors via Surface-Initiated Ring-Opening Metathesis Polymerization.* Journal of the American Chemical Society **126**, 4062 (2004).

152. J. Repp, P. Liljeroth, G. Meyer, *Coherent Electron–Nuclear Coupling in Oligothiophene Molecular Wires.* Nature Physics **6**, 975 (2010).

153. N. Ogawa, G. Mikaelian, W. Ho, *Spatial Variations in Submolecular Vibronic Spectroscopy on a Thin Insulating Film.* Physical Review Letters **98**, 166103 (2007).

154. K. W. Hipps, U. Mazur, *Unoccupied Orbital Mediated Tunneling: Resonance-Like Structures in the Tunneling Spectra of Polyacenes.* The Journal of Physical Chemistry **98**, 5824 (1994).

155. L. Limot, T. Maroutian, P. Johansson, R. Berndt, *Surface-State Stark Shift in a Scanning Tunneling Microscope.* Physical Review Letters **91**, 196801 (2003).

156. S. W. Wu, G. V. Nazin, X. Chen, X. H. Qiu, W. Ho, *Control of Relative Tunneling Rates in Single Molecule Bipolar Electron Transport.* Physical Review Letters **93**, 236802 (2004).

157. R. S. Sánchez-Carrera, V. Coropceanu, D. A. da Silva Filho, R. Friedlein, W. Osikowicz, R. Murdey, C. Suess, W. R. Salaneck, J.-L. Brédas, *Vibronic Coupling in the Ground and Excited States of Oligoacene Cations†.* The Journal of Physical Chemistry B **110**, 18904 (2006).

158. A. B. Trofimov, H. Koppel, J. Schirmer, *Vibronic Structure of the Valence π-Photoelectron Bands in Furan, Pyrrole, and Thiophene.* The Journal of Chemical Physics **109**, 1025 (1998).

159. K. Morgenstern, *On the Interpretation of IETS Spectra of a Small Organic Molecule.* Journal of Physics: Condensed Matter **23**, 484007 (2011).

160. Y. Zhang, V. W. Brar, F. Wang, C. Girit, Y. Yayon, M. Panlasigui, A. Zettl, M. F. Crommie, *Giant Phonon-Induced Conductance in Scanning Tunnelling Spectroscopy of Gate-Tunable Graphene.* Nature Physics **4**, 627 (2008).

161. R. A. Marcus, *Chemical and Electrochemical Electron-Transfer Theory.* Annual Review of Physical Chemistry **15**, 155 (1964).

162. J. Hirsch, *Hopping Transport in Disordered Aromatic Solids: A Re-Interpretation of Mobility Measurements on PKV and TNF.* Journal of Physics C: Solid State Physics **12**, 321 (1979).

163. H. Song, Y. Kim, Y. H. Jang, H. Jeong, M. A. Reed, T. Lee, *Observation of Molecular Orbital Gating.* Nature **462**, 1039 (2009).

List of Abbreviations

AFM	atomic force microscopy, atomice force microscope
DBTH	dibenzo[a,h]thianthrene
DBTJ	double-barrier tunneling junction
DFT	density functional theory
DNTH	dinaphtho[a,j]thianthrene
e-ph	electron-phonon coupling
e-ν	electron-vibron coupling
FEA	finite element analysis
FEM	finite element method
FM-AFM	frequency modulation atomic force microscopy
HOMO	highest occupied molecular orbital
KPFM	Kelvin probe force microscopy
LDOS	local density of states of the sample at the Fermi level at the center of curvature of the tip
LJ	Lennard-Jones potential
LT	low temperature (depending on context either about 4 K or 1.5 K)

LUMO	lowest unoccupied molecular orbital
NC-AFM	noncontact atomic force microscopy
PLL	phase-locked loop
SPM	scanning probe microscopy, scanning probe microscope
STM	scanning tunneling microscopy, scanning tunneling microscope
STS	scanning tunneling spectroscopy
TH	thianthrene
THA	Tersoff and Hamann approximation
UHV	ultrahigh vacuum

List of Symbols

A	oscillation amplitude
α	decay constant of tunneling current
B	magnetic field
β	decay constant of Morse potential
C	heat capacity
χ	magnetic susceptibility
Δf	frequency shift
$\frac{dI}{dV}$	differential conductance
E_{F}	Fermi energy, Fermi level
$f(E,T)$	Fermi-Dirac distribution
F_{ts}	tip-sample interaction force
f_0	eigenfrequency of cantilever
I	tunneling current
k_0	stiffness of cantilever
k_{B}	Boltzmann constant, $8.617 \times 10^{-5}\,\mathrm{eV}$
κ	thermal conductivity
λ	reorganization energy

M	tunneling matrix element
μ_0	magnetic constant, $4\pi \times 10^{-7}\,\mathrm{N/A^2}$
$\mu_\mathrm{B} = \frac{e\hbar}{2m_e}$	Bohr magneton, $57.9\,\mathrm{eV/T}$
Q	quality factor of cantilever
R	gas constant, $8.314\,\mathrm{J/(K\,mol)}$
$\rho(E_F, \mathbf{r}_0)$	LDOS
$\rho_S(E)$	density of states of sample
$\rho_T(E)$	density of states of tip
S	Huang-Rhys factor
T	temperature
Θ_D	Debye temperature
U_ts	tip-sample interaction potential
Q	quality factor of cantilever
V	applied bias voltage
V_CPD	contact potential difference
z	tip-sample separation, coordinate vertical to sample surface

Acknowledgment

At this point I want to address thanks to the many people from which I received support during the course of my thesis.

- First and foremost, I want to address many thanks to Jascha Repp for the excellent supervision I received from him. I am grateful for entrusting me with the design work of the 1-K STM system and the freedom to carry out whatever experiments I was interested in. Despite his willingness to discuss all emerging scientific questions, he never forgot to provide some fun.
- Many thanks are due to Andreas Pöllmann. As the technical expert he had to improve, correct or disapprove many of my ideas particularly with regard to the 1-K system. Not to forget the close collaboration in the assembly and testing phase of the UHV chamber and the cryostat.
- I acknowledge the contributions of all co-workers on the configurational switch as well as on vibration-assisted tunneling. Gerhard Meyer has to be mentioned explicitly. He and Jascha Repp initially realized the spatial dependence of vibronic side bands.
- Thanks are due to our collaboration partners Mario Ruben, Coral-Herranz Lancho and Benoit Fleury for synthesizing the molecules and their chemical expertise in writing the manuscript. Of course, I like to thank Mathias Neu, who has built-up the AFM. His and Florian Albrecht's introduction in AFM saved me a lot of time. I gratefully acknowledge valuable comments on the AFM manuscript by Leo Gross, Gerhard Meyer and Nikolaj Moll.
- Finally, I address special thanks to Jonas for the cover design, as well as Herbert and Florentina for carefully proofreading the manuscript. Besides, thank you for so much more, Florentina!

Niko Pavliček

Personal Data

Born 21.05.1984—Stuttgart, Germany

Status Married, one child

Chronology

2009–2013 **Ph. D. thesis**, Institute of Experimental and Applied Physics, University of Regensburg, Research Group Prof. Dr. Jascha Repp.
Scanning Probe Methods Applied to Molecular Electronics

2004–2009 **Study in physics**, Institute of Experimental and Applied Physics, University of Regensburg, Research Group Prof. Dr. Jascha Repp.
Diploma research project: "Electronic Coupling of Anthracenedicarbonitrile Dimers on Ultrathin Insulating Films"

2003–2004 **Alternative Civilian Service**, Anesthesiology Clinic, University Hospital Freiburg.

2000–2003 **Abitur**, Heinrich-Schickhardt-Schule, Freudenstadt.

Contributions

Articles

1. N. Pavliček, I. Swart, J. Niedenführ, G. Meyer, J. Repp, *Symmetry-Dependence of Vibration-Assisted Tunneling*. Physical Review Letters **110**, 136101 (2013).
2. N. Pavliček, B. Fleury, M. Neu, J. Niedenführ, C. Herranz-Lancho, M. Ruben, J. Repp, *Atomic Force Microscopy Reveals Bistable Configurations of Dibenzo[a,h]thianthrene and their Interconversion Pathway*. Physical Review Letters **108**, 086101 (2012).
3. T. Sonnleitner, I. Swart, N. Pavliček, A. Pöllmann, J. Repp, *Molecular Symmetry Governs Surface Diffusion*. Physical Review Letters **107**, 186103 (2011).

Talks

1. N. Pavliček, *Spatial Dependence of Vibronic Excitations*, presented at the DPG Frühjahrstagung, Regensburg (Mar. 2013).
2. N. Pavliček, *STM/AFM Studies of Molecular Motion*, presented at the Weekly Colloquium, UniBw München (Dec. 2012), Invited Talk.
3. N. Pavliček, *Visualizing the Configurations of a Molecular Switch by Means of Atomic Force Microscopy*, presented at the 24th Conference of the EPS Condensed Matter Division (CMD-24), Edinburgh (Sept. 2012), Invited Talk.

4. N. Pavliček, *On the Influence of Molecular Symmetry on Surface Diffusion*, presented at the DPG Frühjahrstagung, Dresden (Mar. 2011).

Posters

1. N. Pavliček, *Direct Observation of Bistable Conformational Change by Means of Atomic Force Microscopy with Submolecular Resolution*, presented at the 493. WE-Heraeus-Seminar on "Latest Developments in Scanning Probe Techniques focused on Nanotechnology", Bad Honnef (Nov. 2011).
2. N. Pavliček, *Bond Formation Between Single Molecules on Ultrathin Insulating Films*, presented at the DPG Frühjahrstagung, Regensburg (Mar. 2010).